

Università degli Studi di Udine

DIPARTIMENTO DI SCIENZE MATEMATICHE, INFORMATICHE E FISICHE

Corso di Dottorato di Ricerca in Matematica e Fisica

Curriculum in Astrofisica delle Alte Energie

PHD THESIS

Gamma-Ray Transients observed with the *Fermi* Large Area Telescope

Candidato:
Rachele Desiante

Relatore:
Dott. Stefano Ansoldi
Correlatore:
Dott. Francesco Longo

Contents

| | |
|--|-----------|
| Introduction | 3 |
| Time-domain astrophysics | 3 |
| Contents of the thesis | 3 |
| 1 Gamma-ray observatories | 5 |
| 1.1 The <i>Fermi</i> Gamma-Ray Space Telescope | 5 |
| 1.1.1 The Large Area Telescope | 6 |
| 1.1.2 The Gamma-Ray Burst Monitor | 22 |
| 1.2 The MAGIC observatory | 25 |
| 2 Gamma-Ray Bursts | 30 |
| 2.1 Historical overview and basic concepts | 31 |
| 2.1.1 Models for GRBs emission | 36 |
| 2.2 GRBs as observed by the LAT | 40 |
| 2.3 The sample of LLE detected GRBs: spectral analysis | 48 |
| 2.3.1 Analysis methods: background estimation and fitting techniques | 48 |
| 2.3.2 Results and Discussion | 51 |
| 3 Solar Flares | 62 |
| 3.1 The general picture | 62 |
| 3.2 Observations at high-energies | 66 |
| 3.2.1 Solar Flares as observed by the LAT | 66 |
| 3.3 New LAT event selections for solar flares studies | 75 |
| 3.4 LLE-detected solar flares: spectral analysis | 80 |
| 3.4.1 Background estimation and fitting technique | 80 |
| 3.4.2 Results | 81 |
| 4 Active Galactic Nuclei | 92 |
| 4.1 A model for AGN emission | 93 |

| | | |
|----------|---|------------|
| 4.1.1 | Blazars: main characteristics and variability | 95 |
| 4.1.2 | Gamma-ray observations | 96 |
| 4.2 | Fermi-LAT and MAGIC joint observational effort | 100 |
| 4.2.1 | Automated Fermi-LAT analysis pipelines | 100 |
| 5 | Novae | 115 |
| 5.1 | Fermi-LAT observations of novae | 116 |
| 5.2 | Searching for VHE emission with Fermi-LAT and MAGIC | 124 |
| 5.2.1 | Fermi-LAT data analysis | 124 |
| 6 | Conclusions | 130 |
| | Bibliografy | 133 |

Introduction

Time-domain astrophysics

Many observed phenomena in the universe are not static: this is why time-domain astrophysics is a key field of current astronomy and astrophysics. The temporal domain offers an important window on the understanding of extreme phases of stellar and galaxy evolution through studies of novae, supernovae, Gamma-Ray Bursts (GRBs), pulsars, Active Galactic Nuclei (AGN) to list only a few. Variable objects show some different characteristic variability and a lot of information on the physical processes at work comes from measuring luminosity and spectral variations over time.

Launched in June 2008, during its first eight years of operation the *Fermi* Gamma-Ray Space Telescope has confirmed that the gamma-ray sky is highly dynamic on all time scales, from μs to years, providing insight into extreme physical conditions.

The Large Area Telescope (LAT) and the Gamma-ray Burst Monitor (GBM), the two instruments on-board *Fermi* can detect photons with energies from 8 keV up to ~ 1 TeV. Both instruments also have very large Field of View (FoV) achieving together an unprecedented coverage of the hard-X and gamma-ray sky. These characteristics make *Fermi* a perfect observatory to monitor the gamma-ray sky allowing both the study of known transient astrophysical sources and the serendipitous discovery of unexpected variable phenomena.

Contents of the thesis

My research activity is focused on the analysis of transient gamma-ray sources observed by the *Fermi* Gamma-ray Space Telescope and in particular by the LAT, the main instrument on-board *Fermi*. The variable sources analyzed in this thesis spans different observing time scales:

- GRBs and solar flares show an impulsive and short phase that can last from \sim ms to some hundreds of seconds, and a time-extended phase observed at

- higher energies that can lasts several hours;
- AGN show variability from hours to days;
- novae, whose high-energy transient emission lasts for weeks.

In chapters number 2 and 3, I will present the spectral analysis of the impulsive phase of gamma-ray bursts and solar flares using data from the LAT and the GBM. The goal of of this work has been to develop a semi-automatic analysis-pipeline to optimize the source selection and the modeling of background emission in order to better constrain spectral features and infer important physical information on emission processes at work.

In chapter 4 and 5, I will show the analysis performed on LAT data for AGN and novae, in the context of coordinated very-high energy (\sim TeV) observations with the Major Atmospheric Gamma Imaging Cherenkov (MAGIC) telescopes.

The aim of Chapter 1 is to present the main features of the observatories whose data have been used for my analyses.

At the beginning of each subsequent chapter, I report a brief introduction to the physical phenomena at work for the different types of sources studied and a review of observations performed at high-energies (from \sim keV to \sim TeV).

In Chapter 2, I present a detailed spectral analysis of a sample of twenty-five GRBs detected by the LAT through the Low-Energy Technique (LLE) testing different spectral models in order to verify the evidence for additional spectral components such as photospheric components or spectral cut-offs and, in general, to better investigate the low-energy part of the GRBs spectrum.

A detailed spectral analysis of impulsive solar-flares detected using LLE data is presented in Chapter 3: for each flare, different spectral models have been tested to asses the energy spectrum and composition of ambient and accelerated particles during the explosive event.

Chapter 4 is devoted to illustrate the analysis pipeline developed to perform real-time analyses of LAT data in order to monitor the variability of a large number of AGN in the context of coordinated observations with the MAGIC collaboration.

In Chapter 5, I present the results of a joint study using MAGIC and *Fermi*-LAT data of Nova V339 Del during its outburst in August 2013. This work benefits from the same analysis framework developed for the monitoring of AGN showing that it can be easily adapted to monitor also galactic transients and, in general, point sources at different time scales.

Chapter 1

Gamma-ray observatories

1.1 The *Fermi* Gamma-Ray Space Telescope

The *Fermi Gamma-ray Space Telescope* was launched by NASA in June 2008 from Cape Canaveral on a low-intermediate orbit at a height of 565 km above sea level. It consists of two instruments: the LAT [38] and the GBM [114] (Fig.1.1).



Figure 1.1: The Fermi spacecraft shortly before launch: the solar panels are folded at the sides, the GBM detector modules and the telemetry antennas can be seen on the left side, the LAT on the top. Picture taken from [1].

| Parameter | Value or Range |
|---------------------------------------|---|
| Energy Range | ~20 MeV to >300 GeV |
| Energy Resolution | <15% at energies >100 MeV |
| Effective Area | >8,000 cm ² maximum effective area at normal incidence |
| Single Photon Angular Resolution | <0.15°, on-axis, 68% space angle containment radius for E > 10 GeV; < 3.5°, on-axis, 68% space angle containment radius for E = 100 MeV |
| Field of View | 2.4 sr |
| Source Location Determination | <0.5 arcmin for high-latitude source |
| Point Source Sensitivity | <6x10 ⁻⁹ ph cm ⁻² s ⁻¹ for E > 100 MeV, 5σ detection after 1 year sky survey |
| Time Accuracy | <10 microseconds, relative to spacecraft time |
| Background Rejection (after analysis) | <10% residual contamination of a high latitude diffuse sample for E = 100 MeV - 300 GeV. |
| Dead Time | <100 microseconds per event |

Figure 1.2: Main features of the LAT [3].

The GBM and the LAT can detect photons with energies from 8 keV up to ~1 TeV. Both instruments have very large Fields of View (FoV) achieving together an unprecedented coverage of the hard-X and gamma-ray sky: the GBM FoV consists of the whole not-occulted sky and the LAT scans about 20% of the sky at any instant. These characteristics make the *Fermi* Spacecraft a perfect observatory to study and monitor the gamma-ray transient astrophysical sources.

In this section I'll describe the main characteristics of the two instruments.

1.1.1 The Large Area Telescope

The LAT is the main experimental apparatus onboard of *Fermi* and it was developed by an international collaboration between various scientific institutions from USA, Italy, France, Sweden and Japan.

The LAT is a pair-conversion telescope that reconstructs the direction and the energy of an incident photon through the analysis of the tracks and the energy of electrons (e^-) and positrons (e^+) produced in the detector. The LAT is sensitive to γ rays with energy from ~20 MeV to ~1 TeV.

The experimental apparatus (Fig.1.3) consists of an array of 4×4 towers; each module is 84 cm high and comprises a precision tracker (TKR) and a calorimeter. The whole structure is covered by a segmented anticoincidence detector (ACD) to reject the charged cosmic-ray background. The detector is also provided with a programmable trigger and a data acquisition system (DAQ).

The analysis of the conversion of a γ photon in a $e^+ - e^-$ couple is done firstly

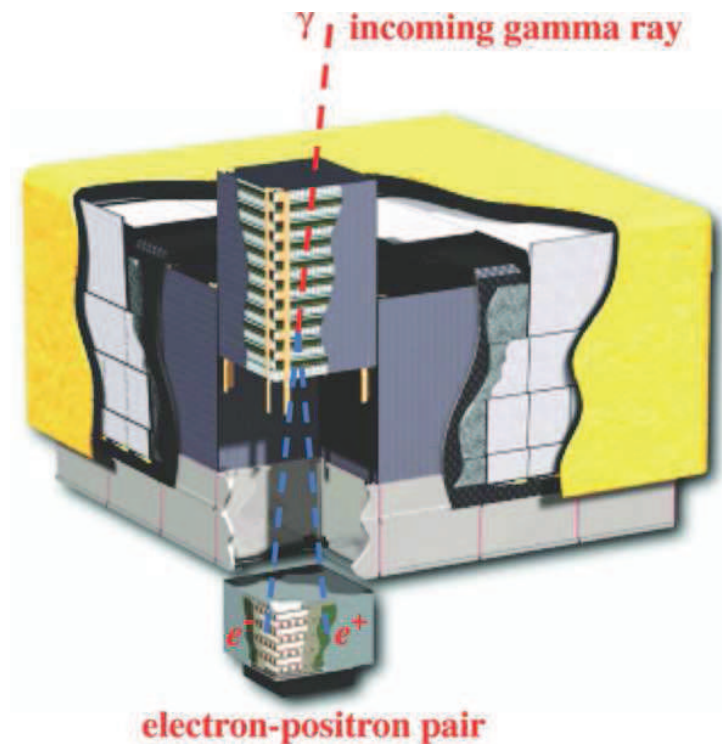


Figure 1.3: Schematic picture of the LAT: the telescope's real dimension is $1.8 \times 1.8 \times 0.72$ m, the required power is 650 W and the mass is 2789 kg [38].

in the TKR where the tracks are reconstructed using an algorithm based of the Kalman filter [76] in order to infer the direction of the primary photon. Then the electromagnetic shower develops in the calorimeter where the energy of the incident photon is measured.

Before launch, the Monte Carlo modeling of the LAT was validated through an on-ground calibration at CERN, GSI and SLAC laboratories. The most extensive beam-test campaign was performed at CERN on a calibration unit (CU), made from some subdetector modules identical to those on-board *Fermi*, including two complete tracker-calorimeter towers. The CU was exposed to photons (up to 2.5 GeV), electrons (1 – 300 GeV), hadrons (π and p, from a few GeV to 100 GeV) and ions (C, Xe, 1.5 GeV/n); see [42], for details.

Anti-Coincidence Detector

The ACD performs the first-level discrimination between the photons and the charged cosmic-ray particles that outnumber cosmic gamma rays by more than 5

orders of magnitude. The ACD covers the four sides of the LAT tracker for a total active area of $\sim 8.3 \text{ m}^2$. In order to suppress self-veto by shower particles at high gamma-ray energies, the LAT ACD is segmented into 89 tiles composed of plastic scintillator of different sizes. The segmentation of the ACD is one of the important innovations of the LAT with respect to the past. In the case of the EGRET telescope, for example, the ACD was monolithic causing self-veto of high-energy gamma rays i.e. the rejection of primary high-energy photons because of the *back-splash* (Fig.1.4) on the ACD of secondary particles produced in the calorimeter. For this reason EGRET detection efficiency at 10 GeV was a factor of two lower than at 1 GeV and the instrument was almost insensitive to photons with energies above $\sim 30 \text{ GeV}$.

The overall ACD efficiency for detection of singly charged relativistic particles entering the FoV of the telescope is very high, with a value exceeding 0.9997.

To protect the ACD from debris hitting its surface, it is covered by a low-mass micrometeoroid shield (0.39 g cm^2).

A more complete description of the ACD and its performance is given in [120].

Precision Converter-Tracker

The LAT converter-tracker modules [40] have 16 planes of high-Z material (tungsten), that allows the conversion into electron-positrons pairs. Each tracker module consists of 18 (x, y) tracking planes, each with two layers (x and y) of single-sided silicon strip detectors. The 16 planes on the top are interleaved with the tungsten foils: the first 12 have a thickness of 0.03 radiation lengths (thin or front section) to maximize the angular resolution at low energies limiting the Coulomb scattering while the last 4 have a thickness of 0.18 radiation lengths (thick or back section) to maximize the conversion probability at high energies. The last two planes have no tungsten converter foils. The aspect ratio of the TKR (height/width) is 0.4, allowing a FoV of 2.4 sr and ensuring that nearly all pair-conversion events will pass into the calorimeter. The self-triggering capability of the TKR is an important new feature of the LAT design; it is possible because of the choice of silicon-strip detectors (SSDs), which do not require an external trigger,

The support structure for the detectors and converter foil planes is a stack of 19 trays (composite panels), supported by carbon-composite sidewalls that also serve to conduct the heat to the base of the tracker array. Figure 1.5 shows a flight tracker tray (on the left) and a completed tracker module (on the right) with one sidewall removed.

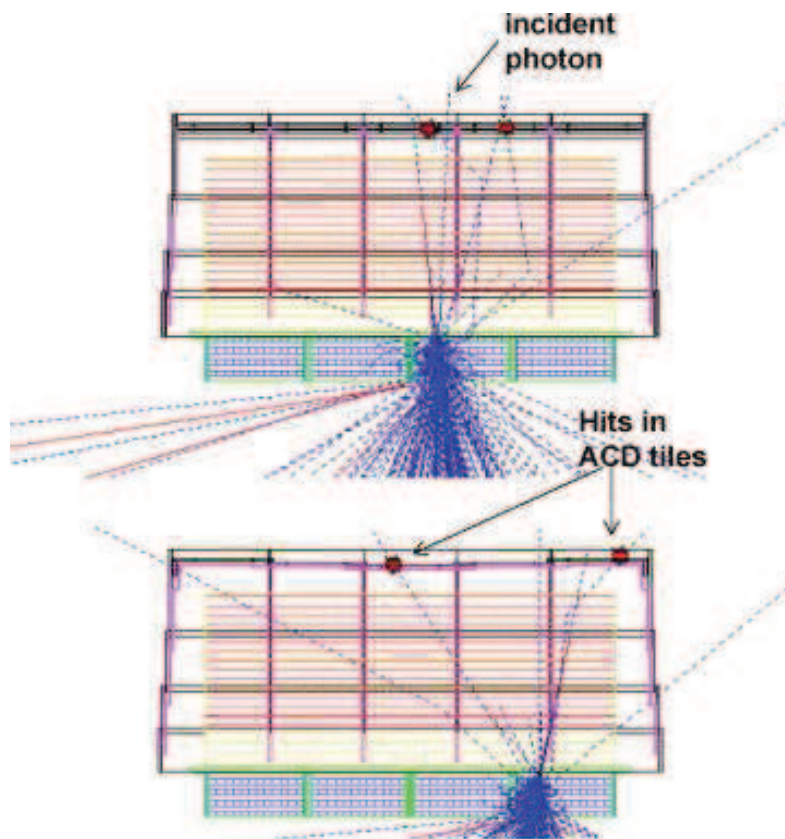


Figure 1.4: Simulation of the *backslash* effect in the LAT ACD: charged particles are shown by red lines, protons by blue dashed lines, signals in the ACD caused by *backslash* are shown by red dots [120].

Calorimeter

The LAT calorimeter was built to cover an energy range of more than five orders of magnitude: in fact, although it is only 8.6 radiation lengths deep, the longitudinal segmentation enables energy measurements up to a TeV. The calorimeter modules are placed at the bottom of each of the 16 towers, right below the TKR module. The primary purposes of the calorimeter are:

- measure the energy deposition due to the electromagnetic particle shower that results from the e^+e^- pair produced by the incident photon;
- image the shower development profile, thereby providing an important background discriminator and an estimator of the shower energy leakage fluctuations.

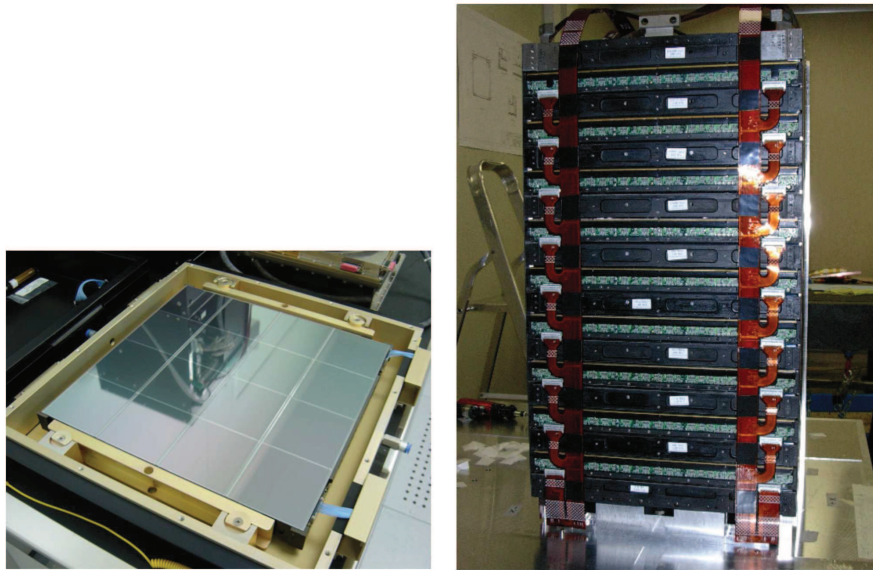


Figure 1.5: On the left: a flight tracker tray. On the right: a completed tracker module (one sidewall removed). [38]

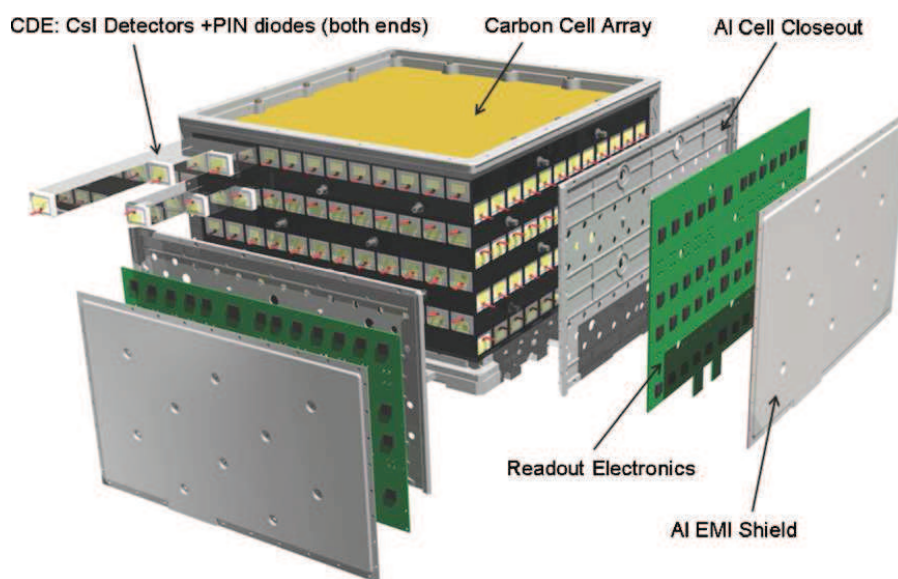


Figure 1.6: Module of the LAT calorimeter [38].

The segmented structure permits to sample the electromagnetic shower and to reconstruct very well its longitudinal and lateral development. In fact the lateral

segmentation provides the necessary imaging capability to correlate the events in the tracker with the energy depositions in the calorimeter and derive loose (at the level of few degrees) directional information for those photons not converting in the tracker. On the other side the longitudinal segmentation allows to derive an estimate of the initial energy of the pair from the longitudinal shower profile by fitting the measurements to an analytical description of the energy-dependent mean longitudinal profile.

Each calorimeter module has 96 CsI(Tl) crystals (size $2\text{ cm} \times 2.7\text{ cm} \times 32.6\text{ cm}$); the crystals are optically isolated from each other and are arranged horizontally in 8 layers of 12 crystals. Each layer is rotated by 90° with respect to the previous one in the so called "hodoscopic configuration", in order to achieve x-y imaging capabilities [51].

More information about the design process of the LAT calorimeter are reported in [99] and [83], while ground calibrations results are in [77].

Data Acquisition System

The Data Acquisition System (DAQ) collects the data from the other subsystems, implements the multilevel event trigger (at a rate of 2 - 3 kHz), provides on-board event processing to run filter algorithms to reduce the number of downlinked events to $\sim 500\text{ Hz}$, and provides an on-board science analysis pipeline to rapidly search for transients.

The tracker and calorimeter modules of each tower are interfaced by a tower electronics module (TEM), generating tower-based triggers. At the entire instrument level a global unit collects signals from all the electronics module and distributes the clock signal, provides an interface with the ACD, generates instrument-wide triggers based on the information received from the TEMs and the ACD interface and builds the events with the information received from the whole apparatus, sending them to the event processor units (EPUs). The minimum read-out time per event is $26.5\ \mu\text{s}$, due to the transmission of the trigger signal between the different units. During the event read-out the different subsystems send a busy signal to the global unit, which generates the overall dead time and send it to the ground along with data.

The two EPUs implement the onboard filtering aimed at reducing the contamination by charged particles. In fact the events triggering the LAT are mostly background due to cosmic-ray interactions. The onboard analysis is designed in order to maximize the efficiency for γ -ray detection and keep the data flow within the bandwidth allowed for downlink. Note that all events exceeding a threshold of raw energy deposited in the calorimeter ($\sim 20\text{ GeV}$) are downlinked at Earth for analysis since their rate is low.

The Fermi orbit crosses the Earth inner radiation belt in a region known as

the South Atlantic Anomaly (SAA). The SAA consists of geomagnetically trapped particles with fluxes exceeding by several orders of magnitude those in the rest of the orbit. This hard radiation environment would lead to the saturation of the tracker electronics, with a drastic reduction of the live-time, and high currents in ACD PMTs exceeding the safe operation limits and producing a rapid deterioration. Therefore, the LAT does not take data during the passages in the SAA. This turn-off leads to a loss in observation time of $\sim 13\%$ of the total on-orbit time [9].

Event classification and background rejection

Event classification aims at reducing the backgrounds in the final data sample as well as at selecting the best estimates of the event direction and energy and determining their accuracy. These purposes are achieved using a series of classification trees, automated algorithms which partition a data set into classes generating complex event selection criteria

The background rejection is a fundamental task since the background events triggering the LAT exceed by 10^5 the celestial γ -ray flux. The on-board filter is configured in order to fit the available band for data downlink at the Earth while keeping the largest possible efficiency for γ -ray detection, reducing the signal-to-noise ratio at $\sim 1 : 300$). The background rejection at Earth aims at further reducing the backgrounds by almost three orders of magnitude.

The various scientific objectives of the LAT Science require an appropriate tuning of the instrument performance and of background contamination. LAT data are classified in different event-classes ordered on the basis of the background rejection. This classification allows to choose the proper event-class to use for an analysis depending on the characteristics of the source that the user is going to study prior to launch, a few event classes, called "Pass 6"¹, were defined. The TRANSIENT class, suitable for studying bright, transient phenomena, was designed to maximize effective area, particularly at low energy, at the expense of higher residual background rate (< 2 Hz); it would result in no more than one background event every 5 s inside a 10° radius around a source. The SOURCE class was designed so that the residual background contamination was similar to that expected from the extra-galactic gamma-ray background flux over the entire FoV (< 0.4 Hz). It is suitable to study localized sources. The DIFFUSE class, so called because it was specifically tuned to study diffuse γ -ray emission, was the purest class, expected to achieve a background-rejection factor of the order of 10^6 , while keeping an efficiency for γ -ray detection $\sim 80\%$ [38].

The high-level final results of the event analysis are collected in FITS files that contain a table where each detected photon is associated with an energy, a set of

¹See next paragraph 1.1.1 for details on more recent event classes.

spacial coordinates and some additional pre-computed quantities, as well as a flag which allows the user to select among the different event classes.

LAT photon data are publicly available through the Fermi Science Support Center (FSSC)², together with the orbital history of the telescope and more information about last developed event-classes³.

The LAT Instrument Response Functions

The Instrument Response Functions (IRFs) are a set of analytical functions that describe the response of the detector to the incident photons. The IRFs depend from the detector itself, from the reconstruction algorithms, from the background-rejection algorithms and from the event quality selection in general. To evaluate the LAT response, dedicated Gent4-based Monte Carlo simulations have been performed. A large number of gamma-ray events are simulated in order to cover all possible photon inclination angles and energies with good statistics. This is based on the best available representation of the physics interactions, the instrument, and the on-board and ground processing to produce event classes (see [38] and [24]). The comparison between the properties of the simulated events within a given event class and the input photons gives the instrument response functions.

If F is the differential flux of incident particles, the flux of detected particles is given by this equation:

$$\frac{dN(E', \vec{v}')}{dE dt} = R(E', \vec{v}' | E, \vec{v}) F(E, \vec{v}) \quad (1.1)$$

E and \vec{v} (E' and \vec{v}') are the measured (reconstructed) energy and incident direction of the primary photon. $R(E', \vec{v}' | E, \vec{v})$ is the IRF. It is usually factorized in this way:

$$R(E', \vec{v}' | E, \vec{v}) = A_{eff}(E, \vec{v}) PSF(\vec{v}' | E, \vec{v}) \Delta E(E' | E, \vec{v}) \quad (1.2)$$

The three functions on the left are:

- $A_{eff}(E, \vec{v})$, the detector Effective Area;
- $PSF(\vec{v}' | E, \vec{v})$, the Point Spread Function: that links the true direction with the reconstructed one;
- $\Delta E(E' | E, \vec{v})$, the Energy Dispersion: that transforms the true energy of the primary photon into the measured one.

²<http://fermi.gsfc.nasa.gov/ssc/data/>

³http://fermi.gsfc.nasa.gov/ssc/data/analysis/documentation/Cicerone/Cicerone_Data/LAT_DP.html

The various analysis cuts, event selections and the IRFs optimized before the launch are known as P6_V1 [38]. The IRFs obtained after the first year are known as P6_V3 [150] optimized for the conditions found on-orbit during the all-sky survey phase⁴.

The next set of IRFs, is called "Pass 7" (P7). Additional science classes available for specific kind of analysis were developed, as looser cuts for the transients and selection for charged particles.

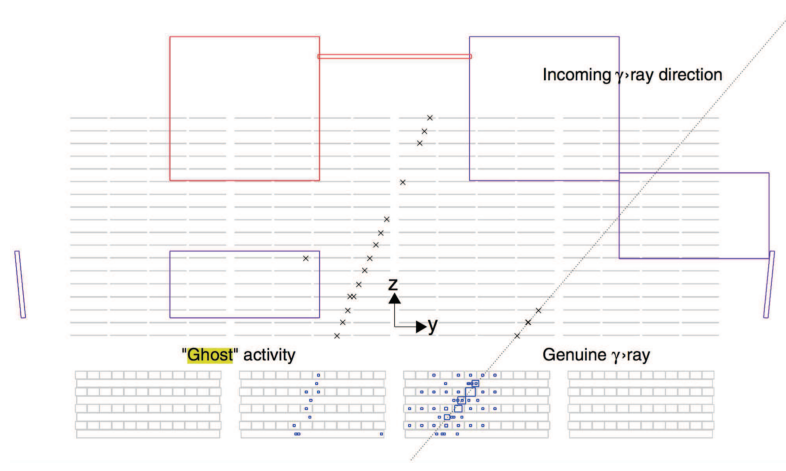


Figure 1.7: Example of a ghost event in the LAT (y - z orthogonal projection). A 8.5 GeV back-converting γ -ray candidate is also shown on the right. Note the additional activity in all three LAT subsystems, with the remnants of a charged particle track crossing the ACD, TKR, and CAL. The small crosses represent the clusters (i.e., groups of adjacent hit strips) in the TKR, while the variable-size squares indicate the reconstructed location of the energy deposition for every hit crystal in the CAL (the side of the square being proportional to the magnitude of the energy release). The dashed line indicates the γ -ray direction. For graphical clarity, only the ACD volumes with a signal above the zero suppression level are displayed. Figure and caption are taken from [24].

The switch between the P6_V3 and the P6_V1 IRFs was needed since the so called ghost events effect [150] was observed on-board and it was not previously introduced in the Monte Carlo simulations. In fact, soon after launch, it became apparent that

⁴After a \sim two months "on-orbit checkout phase", Fermi carried out a one-year validation and sky survey program, designed for relatively uniform sky coverage, in order to fully validate the performance of the science instruments and to refine the data processing pipelines based on operational experience.

the LAT was recording events that included an un-predicted background: remnants of electronic signals from particles that passed through the LAT a few μs before the particle that triggered the event.

The spectral analysis done with the IRFs obtained from a Monte Carlo sample without ghost events, as the P6_V1, are affected by a systematic overestimate of the LAT efficiency. In P6_V3 IRFs the ghost effect is introduced in the Monte Carlo achieving a correct modeling of the instrument; the P7 IRFs also correct the reconstruction taking care of the spurious signal.

Since the IRFs are strongly dependent on the hardware of the telescope, two kinds of them are separately generated: FRONT to choose only events that convert in the thin part of the tracker, BACK for the thick part of it, or can be used together by combining them.

The subsequent IRFs set is called "P7 REProcessed" (P7REP_V15, based the same event analysis and selection criteria as the previously released P7_V6 IRFs. The P7REP dataset was reprocessed from scratch with updated calibration constants. The primary differences with respect to the P7_V6 IRFs are the correction of a slight measured degradation (1% per year) in the calorimeter light yield and a significant improvement of the calorimeter position reconstruction, which in turn significantly improved the LAT PSF at high energies (> 5 GeV). More details about the reprocessing can be found in [49].

The LAT data currently being released by the FSSC have been processed using the "Pass 8" event-level analysis. The Pass 8 analysis uses an entirely new set of event-level reconstruction algorithms that improve the instrument performance and mitigate pile-up effects. The Pass 8 data are processed with the same calibration constants used for the P7REP data release [37]. The current Pass 8 data set is known as P8R2.

Each event class is defined by a set of event selections and has a corresponding set of IRFs that are unique to that class. The multiple IRFs relative to the different event classes delivered with the Fermi Science Tools allow the user the flexibility necessary for the different analysis types. The online LAT-performance page is kept updated in case of new IRFs release⁵.

Effective Area, Acceptance, Field of View, Point Spread Function and Energy Dispersion

The Effective Area depends on the energy of the primary photon and from its incident direction. It can be expressed in polar coordinates centered in the LAT with the z-axis that goes through the instrument from the calorimeter to the tracker

⁵http://www.slac.stanford.edu/exp/glast/groups/canda/lat_Performance.html

and the x-axis along the solar panel direction.

The effective area as a function of energy for the three event classes *TRANSIENT*, *SOURCE* and *ULTRACLEAN*⁶ is shown in Fig.1.8A. Fig.1.8B shows the effective area as a function of the incident photon direction from the *SOURCE* event-class and for different conversion types. At low energies ($\lesssim 100$ MeV), the effective area for the *TRANSIENT* event-class is almost a factor of three higher than the one for the class *ULTRACLEAN*. This feature, regardless the high background contamination, makes the *TRANSIENT* event class, the proper choice to analyze very short (duration $< \sim 200$ s) transient phenomena like the prompt phase of Gamma Ray Bursts and the impulsive phase of Solar Flares (see Chapters 2 and 3 respectively).

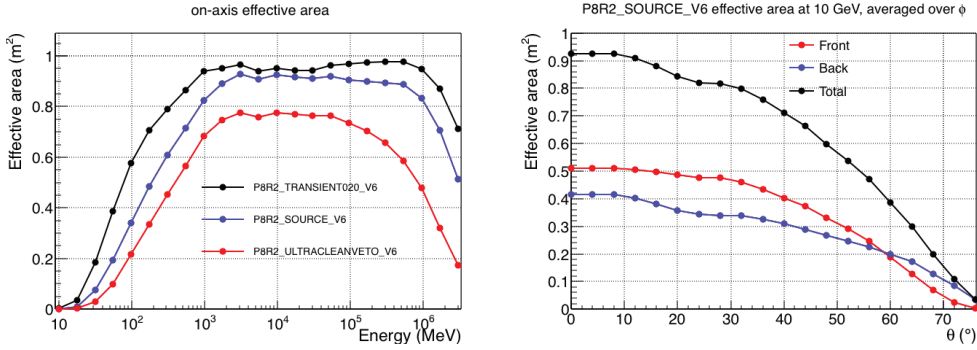


Figure 1.8: Left panel (A): effective area at normal incidence ($\theta = 0$) for different event classes. Right panel (B): effective area at 10 GeV as a function of the inclination angle of the incident photon for the *SOURCE* event class and for different conversion types. Both images are taken from [2].

The FoV is defined as the ratio between the acceptance (effective area integrated on the solid angle) and the peak effective area.

$$FoV = \frac{Accept}{A_{eff}(0,0)} = \frac{\int A_{eff}(\theta, \phi) d\Omega}{A_{eff,peak}} \quad (1.3)$$

For the LAT, after all the background selection cuts, the FoV is ~ 2.4 sr at 1 GeV.

The Point Spread Function (PSF) is the probability distribution for the reconstructed direction of incident photons from a point source. We can say also that the PSF is the effective angular resolution of the instrument, after all detector, reconstruction and background rejection effects. In particular, the 68% containment

⁶As previously cited, LAT data are classified in different event-classes ordered on the basis of the residual background rate.

angle indicates the angular resolution and the ratio between 95% and 68% containments actually gives an idea of how gaussian is the instrument response. The plots in Fig.1.9 shows: the 68% and 95% containment angles of the acceptance-weighted PSF and the ratio between PSF95% and PSF68%; both plots are referred to FRONT and BACK event types (the dependence on the off-axis angle is included).

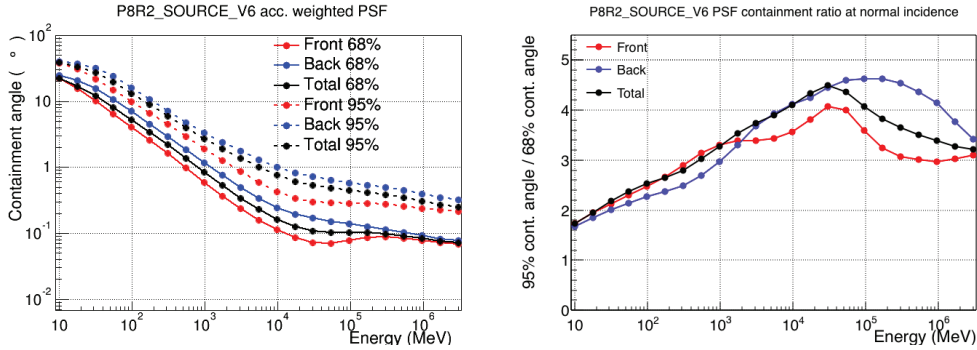


Figure 1.9: Left panel: 68% and 95% containment angles of the acceptance-weighted PSF. Right panel: the ratio PSF95% / PSF68%, which is a useful indicator of the magnitude of the tails of the distribution. Both images are taken from [2].

The Energy Redistribution Function describes the probability density to have a reconstructed energy E' , given the true energy E and the true incoming direction of the photons. In an ideal case, at fixed energy of the incoming photons, the energy redistribution function is a delta function but in real detectors, the energy response function can be fitted with a Gaussian with a mean value (E_{mean}) and a standard deviation σ . A good description of the Energy Redistribution function can be given, for each value of the true energy E , in terms of the energy resolution, that is defined as:

$$R = \frac{\sigma}{E_{mean}} \quad (1.4)$$

Fig.1.10 shows the energy resolution for the SOURCE event-class versus the reconstructed energy of the incident photon (left panel) and then versus its the inclination angle respect to LAT z-axis.

Pass 8 data

Pass 8 provides a full reprocessing of the entire mission dataset, including improved event reconstruction, a wider energy range, better energy measurements, and significantly increased effective area. In addition, the events have been evaluated for their measurement quality in both position and energy. This allows to

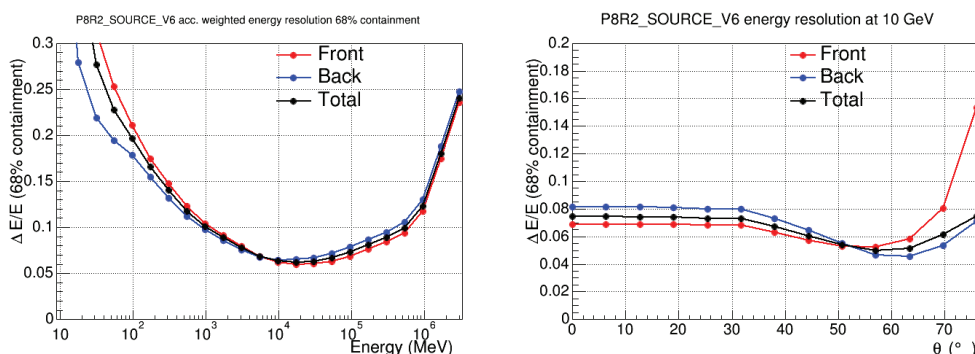


Figure 1.10: Left panel: acceptance-weighted energy resolution (i.e. 68% containment half width of the reconstructed incoming photon energy) as a function of energy. Right panel: energy resolution as a function of incidence angle for 10 GeV photons. Both images are taken from [2].

select a subset of the events if appropriate to improve analysis results.

The main features of the P8R2_V6 IRFs are:

- Subdivision of IRFs into three event type partitions (FRONT/BACK,PSF, and EDISP). Previous IRF releases were partitioned only by conversion type into FRONT and BACK events⁷.
- No flight-based corrections have been made to the effective area or PSF. Systematic uncertainties in the effective area and PSF are less than 5% between 100 MeV and 10 GeV.
- New tables that contain a correction for the bias in the LAT event direction reconstruction (the so called "fish-eye effect") as a function of energy and incidence angle. The "fish-eye effect" is a bias in the reconstructed event direction toward the LAT boresight. This effect is largest at low energies and high incidence angles. Although the Fermi Science Tools do not currently provide a mechanism for applying this correction, these tables can be used to quantify systematic uncertainties on source localization that may be induced by this effect⁸.

All systematic uncertainties associated with the IRFs P8R2_V6 are documented in the LAT Caveats page⁹.

⁷See https://www.slac.stanford.edu/exp/glast/groups/canda/lat_Performance.htm for details.

⁸http://fermi.gsfc.nasa.gov/ssc/data/analysis/documentation/Cicerone/Cicerone_LAT_IRFs/IRF_PSF.html

⁹<http://fermi.gsfc.nasa.gov/ssc/data/analysis/caveats.html>

Figures 1.11 and 1.12 show a direct comparison between P7REP and Pass 8 LAT-performance plots using the SOURCE event class¹⁰ Fig.1.13 shows the improvement in the PSF and photon acceptance from Pass 7 to Pass 8 using a surface map; the LAT Pass 8 PSF is nearly 20% narrower above 10 GeV.

These improvements directly impact the LAT science performance, especially for transient searches. As shown in Fig.1.14 (left panel), the gain in photon counting statistics is >50% below 150 MeV and above 300 GeV: this effectively expands the energy bandwidth of the LAT standard analysis. The change is particularly important at the highest energies, where the scientific return is always limited by counting statistics, providing important targets for current and future very-high-energy telescopes, for joint studies and to increase their observing efficiency. The enhanced photon counts also directly improves the source detection, the determination of spectral shapes and is particularly critical for measurement of time variability, as said in the introduction, a characteristic of many gamma-ray sources. The better PSF together with increased acceptance improves source localization (Fig.1.14, right panel) and identification, as well as the resolution of spatially extended sources.

Moreover, the *Fermi* collaboration team is planning to increase the opportunities for transient source science by greatly reducing the processing and transmission latencies in the ground network by two-three hours and to halve the time for implementing target of opportunity observations enabling more frequent near-simultaneous multi-wavelength and multi-messenger observations. The Pass 8 enhancements to the LAT performance, the accumulated LAT observations of the gamma-ray sky over years, and new strategies for reducing data latencies will significantly improve the LAT capabilities of detecting and studying transient sources

Lat Low-Energy data product

The LAT Low Energy analysis (LLE) is a type of analysis developed by the Fermi-LAT and GBM teams for increasing the effective area of the Large Area Telescope at low energy, and it is suitable for studying short transient phenomena, such as Gamma-Ray Bursts and Solar Flares. The LLE analysis filters event data with a very loose event selection, requiring only minimal information, such as the existence of a reconstructed direction.

The reconstructed direction is used to select events that are compatible with a certain location in the sky, using information on the Point Spread Function to increase the signal-to-noise ratio. The instrument response is calculated with a dedicated Monte Carlo simulation that uses satellite pointing information and the

¹⁰Recall that this event class is designed so that the residual background contamination was similar to that expected from the extra-galactic gamma-ray background flux over the entire FoV (< 0.4 Hz) and that it is the recommended choice to study point sources.

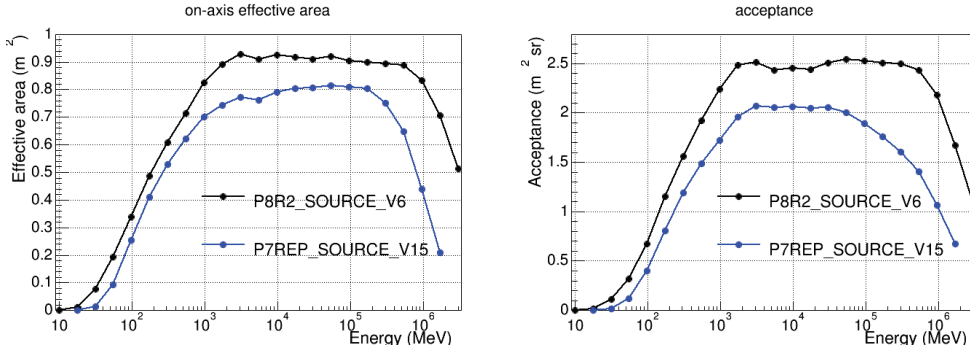


Figure 1.11: Comparison between Pass 8 and P7Rep effective area (on the left) and acceptance (on the right) [2].

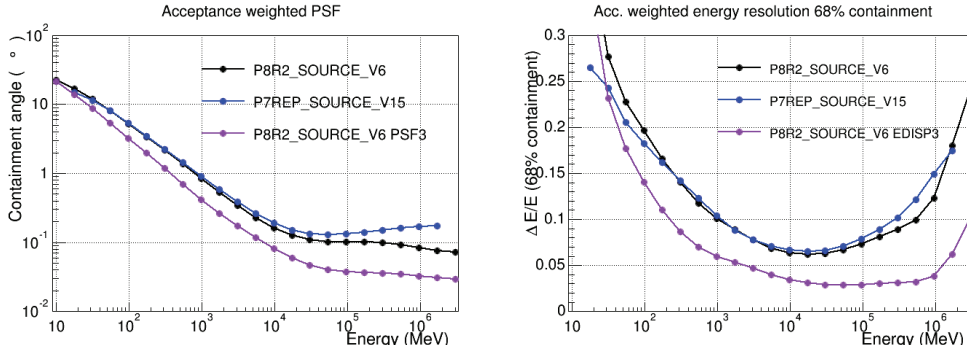


Figure 1.12: Comparison between Pass 8 and P7Rep PSF (on the left) and energy resolution (on the right); note that the LAT Pass 8 PSF is nearly 20% narrower above 10 GeV [2].

celestial location of the source. The LLE data selection and response depend on the input localization of the source; this is first taken by default from the Fermi GBM Trigger Catalog and then eventually refined using a more accurate estimation by the LAT.

The Monte Carlo used to generate the response covers an energy range up to 100 GeV. At low energy the effect of the energy dispersion can be significant so any spectral analysis below 30 MeV is currently discouraged.

Above a few hundred MeV (the exact value depends on the inclination angle of each event respect to the LAT z -axis) the signal-to-noise ratio for standard data (TRANSIENT, SOURCE and cleaner event classes) is higher than that for LLE data. In case of bright hard events, it is suggested to use standard LAT event data at high energy and LLE data at low energy.

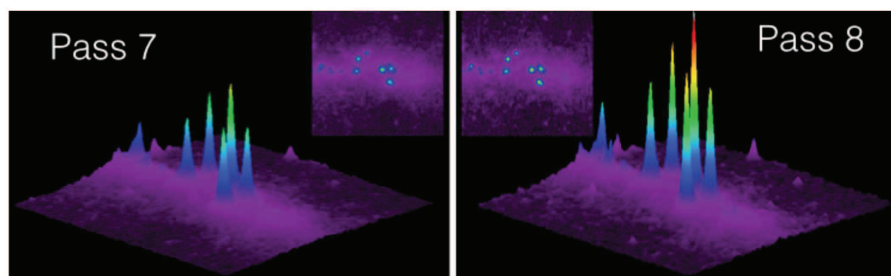


Figure 1.13: Improvement in the PSF and photon acceptance from Pass 7 to Pass 8 demonstrated by these planar and surface maps of the gamma-ray intensity at > 1 GeV in the Carina region of the Galactic plane; picture and caption are taken from [4].

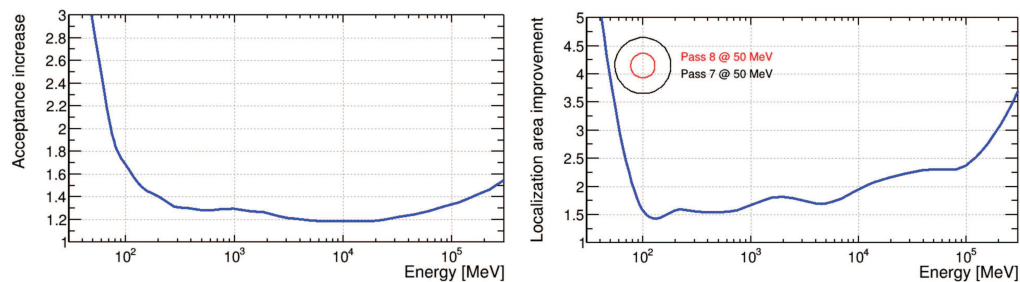


Figure 1.14: On the left: acceptance ratio showing the gain in photon statistics in Pass 8 relative to Pass 7. The acceptance increases at all energies, with the greatest improvements at the lowest and highest energies. On the right: localizations improve in Pass 8; the circles illustrate the relative areas at 50 MeV. The overall improvement for any particular source is at least 50% and can be much larger for very soft or very hard sources. Figures and captions taken from [4].

The background in LLE is mainly driven by residual particle events and soft gamma-ray events mostly coming from the bright limb of the Earth. During Autonomous Repoint Requests (ARR) observations¹¹, since a significant fraction of the Earth Limb enters the LAT field of view, an increase of the event rate is clearly visible in LLE data. Moreover, LLE data are background-dominated so, as already

¹¹An ARR occurs when the spacecraft autonomously slews to and performs a pointed observation at the location of a gamma-ray burst detected onboard the LAT or GBM which meets some pre-defined criteria. Currently, an ARR observation lasts for five hours: during the time that the GRB is occulted by the Earth, the observatory will perform an Earth avoidance maneuver to keep the Earth out of the LAT FoV.

said, they are suitable to study only short-impulsive events ($\lesssim 200$ s).

As happened for standard data selection, the LLE analysis has been updated to the new Pass 8 event reconstruction and additional selection cuts have been added to reduce the contamination from cosmic-ray events.

The released FITS files contain the data together with the instrument response and can be downloaded from the "Fermi LAT Low-Energy Events Catalog" ¹².

1.1.2 The Gamma-Ray Burst Monitor

The Gamma Ray Bursts Monitor (GBM) (see Fig.1.15) is the secondary instrument on-board the Fermi satellite and its goal is to improve the science return from Fermi with its prime objective being joint spectral and timing analyses of GRBs. In addition, GBM provides near real-time burst locations which permit: (i) the Fermi spacecraft to repoint the LAT towards the observed GRB and (ii) to communicate the position to ground-based observatories. Compared to other high-energy spacecrafts, the great advantage of GBM is its capability to observe the whole unocculted sky at any time with a FoV of $\gtrsim 8$ sr and its very broad energy coverage from 8 keV to 40 MeV. Therefore, GBM offers great capabilities to observe all kinds of high-energy astrophysical phenomena, such as e.g. GRBs Solar Flares, Soft Gamma Repeaters, Terrestrial Gamma-Ray Flashes and now possible electromagnetic counterparts to Gravitational Waves detections.

Hardware

GBM is composed of 12 thallium-doped sodium iodide (NaI(Tl)) scintillation detectors which are sensitive from 8 keV to 1 MeV and 2 bismuth germanate (BGO) detectors (see Fig.1.16), sensitive from 200 keV to 40 MeV. The NaI crystals have a thickness of 1.27 cm and a diameter of 12.7 cm. Their positions are oriented such that by measuring the relative counting rates in the detectors the position of the GRB can be determined with a systematic error from few degrees of up to 15° [59]. Each BGO crystal, on the other hand, has a diameter and thickness of 12.7 cm and the detectors are located on opposite sides of the spacecraft so that at least one is illuminated from any direction. The energy band of the BGOs overlaps both the NaI and LAT energy range at low and high energies, respectively.

Triggering and Data products

While GBM continuously observes the sky, its flight software constantly monitors the count rates recorded in the various detectors. To trigger on a GRB or any other high-energy transient, two or more detectors must have a statistically

¹²<https://heasarc.gsfc.nasa.gov/W3Browse/fermi/fermille.html>

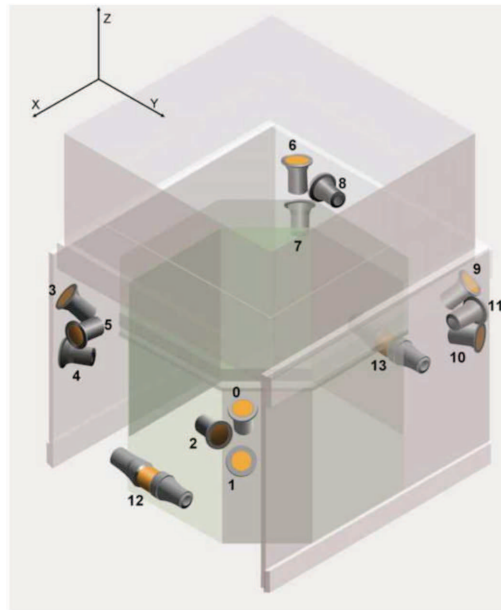


Figure 1.15: A scheme of the GBM detectors orientation on the spacecraft [114].

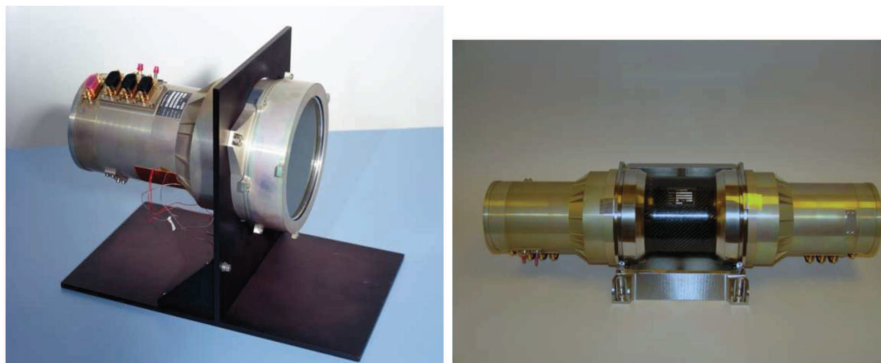


Figure 1.16: Left panel: NaI(Tl)-detector flight unit; right panel: BGO detector [114].

significant increase in count rate above the background rate. GBM currently operates on 75 (of 119 supported) different trigger algorithms, each defined by its timescale (from 16 ms to 4 s), offset (value in ms by which the time binning is shifted) and energy range (25 - 50 keV, 50 - 300 keV, > 100 keV, and > 300 keV). Additionally, each trigger algorithm can be operated on different threshold settings. GBM persistently records two different types of science data, called CTIME (fine

time resolution, coarse spectral resolution of 8 energy channels) and CSPEC (coarse time resolution, full spectral resolution of 128 energy channels). CTIME (CSPEC) data have a nominal time resolution of 0.256 s (4.096 s) which is speeded up to 64 ms (1.024 s) whenever GBM triggers on an event. After 600 s in triggered mode, both data types are returned to their non-triggered time resolution. The third data type are the "Time Tagged Events" (TTE) which consist of individual events, each tagged with arrival time ($2 \mu\text{s}$ resolution), energy (128 channels) and detector number.

A new analysis pipeline for the GBM, using "Continuous Time-Tagged Events" (CTTE) enhanced its capability to recognize short GRBs increasing the number of short-duration GRBs to 80/year: most of them are not detectable with other instruments.

Science data products (Trigger and Burst Data) created by the GBM's Instrument Operation Center together with useful information about the analysis are provided by the Fermi Science Support Center web page ¹³.

¹³<http://fermi.gsfc.nasa.gov/ssc/data/access/gbm/>

1.2 The MAGIC observatory



Figure 1.17: The two 17 m diameter MAGIC telescope system operating at the Roque de los Muchachos observatory in La Palma [33].

The MAGIC (Major Atmospheric Gamma Imaging Cherenkov) observatory consists in a stereoscopic system of two Imaging Atmospheric Cherenkov Telescopes (IACTs) located at 2200 m a.s.l. in the observatory of Roque de los Muchachos in La Palma, Canary Islands (Spain) (Fig.1.17) [33]. Together with the H.E.S.S. IACTs in Namibia (four telescopes with 108 m^2 mirror area each and one telescope of 614 m^2) [26] and the VERITAS IACTs in Arizona (mirror area: $2 \times 110 \text{ m}^2$) [95], MAGIC (mirror area: $2 \times 236 \text{ m}^2$) is the most sensitive instrument for high-energy gamma-ray astrophysics in the range between few tens of GeVs and tens of TeVs ($\sim 50 \text{ GeV} - 50 \text{ TeV}$).

IACTs can observe dim ($\sim 100 \text{ photons} / \text{m}^2 / \text{TeV}$) short ($\sim \text{ns}$) flashes produced by extended air showers developing in the atmosphere ([94], [111]). The light, mostly emitted in the UV and optical wave bands, is produced via Cherenkov radiation when charged particles of the atmospheric shower travel faster than the light in the air. The amount of Cherenkov light and its angular and spatial distribution carry information about the energy and incoming direction of the primary cosmic rays and γ -ray photons. The incoming direction is then reconstructed analyzing

the image (roughly an ellipse) formed on the focal plane of the telescope; the ellipse brightness, geometrical size, and orientation are the parameters used in the subsequent data analysis (see [92]). Moreover, multiple images of the same air shower (stereoscopic reconstruction) allow a more precise reconstruction of the energy and the incoming direction of the primary γ -ray.

The telescopes are self-triggered by multiple, neighbor pixels above a certain signal threshold. Because the Cherenkov light flashes from air showers are very short, the use of extremely fast and sensitive light sensors, like photomultiplier tubes (PMTs), and fast electronics for the trigger and signal sampling is the key to discriminate the shower light from fluctuations of the night sky background.

The major goal of the telescopes is a lowest possible energy threshold, which is achieved through fine pixelated cameras, fast sampling electronics and a large mirror area. The second goal is a fast re-positioning speed in order to catch rapid transient events such as gamma-ray bursts: for this purpose the telescope structure was made out of reinforced carbon fibre tubes in order to be as light as possible (<70 tons). The structure also requires an automatic mirror control to maintain the best possible optical PSF at different zenith angles of observations ([110]).

The MAGIC-I and MAGIC-II telescopes started operation in 2004 and 2009 respectively; the second telescope was an "improved clone" of the first one. In 2011-2012 MAGIC underwent a major upgrade program to improve and to unify the stereoscopic system of the two telescopes. In particular, the main motivations for the upgrade were:

- improve the low-energy performance through a lowering of the readout noise;
- improve the flux sensitivity to extended sources by enhancing the trigger area of the first telescope: in this way, extended sources up to $\sim 0.5^\circ$ extension can be analyzed and a better control of the background region has been achieved;
- reduce the dead-time of the system in order to gain a $\sim 12\%$ of observation time;
- achieve a better angular resolution of the instrument by replacing the camera of MAGIC-I telescope with one containing small pixels only instead of the previous "mixed" configuration.

The upgrade was also motivated by the need of reducing both:

- the downtime due to technical problems through the implementation of an online monitoring set of tools that immediately alert the shifters and experts in case of any problem;
- the manpower and expertise necessary to run MAGIC in the future.

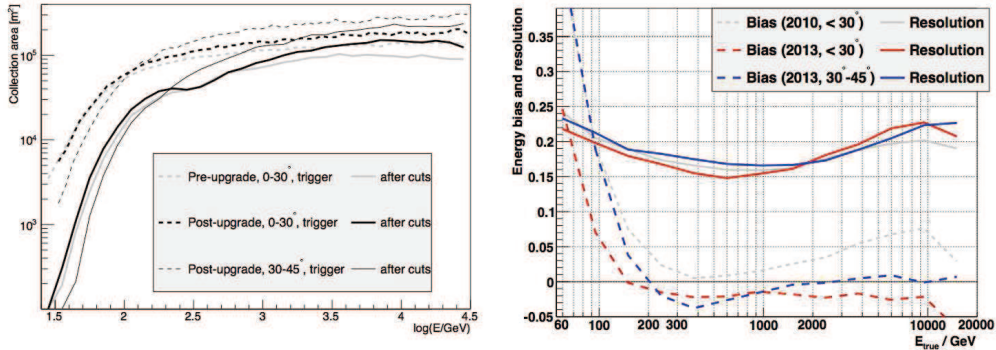


Figure 1.18: On the left: collection area of the MAGIC telescopes after the upgrade at the trigger level (dashed lines) and after all cuts (solid lines). Thick lines show the collection area for low zenith angle observations, while thin lines correspond to medium zenith angle. On the right: energy resolution (solid lines) and bias (dashed lines) obtained from the Monte Carlo simulations of γ -rays. Red: low zenith angle, blue: medium zenith angle. For comparison, pre-upgrade values are shown in gray lines. Both images and captions are taken from [34].

The performance parameters of the MAGIC telescopes after the upgrade and the influence of the upgrade on the systematic uncertainties of the measurements has been detailed discussed in [34] using data from the Crab Nebula.

The Crab Nebula is a nearby (~ 1.9 kpc away [175]) pulsar wind nebula, and the first source detected in very-high-energy (VHE) γ -rays [180]. A few years ago, the satellite γ -ray telescopes, AGILE and Fermi-LAT observed flares from the Crab at GeV energies ([173], [7]). However so far no confirmed variability in the VHE range was found so it is still considered the brightest steady VHE γ -ray source and it is frequently used to evaluate the performance of VHE instruments.

The best performance of the MAGIC telescopes is achieved at medium energies, at a few hundred GeV: at those energies the images are sufficiently large to provide enough information for efficient reconstruction, while the rapidly falling power-law spectrum of the Crab Nebula still provides enough statistics. The energy resolution at these medium energies is as good as 16% with a negligible bias and the angular resolution is 0.07° . The sensitivity above 220 GeV is $(0.66 \pm 0.03)\%$ of C.U¹⁴ for 50h of observations. Below 100 GeV, the performance has improved drastically, reducing the needed observation time by a factor of 2.5. The larger trigger region and pixelization of the MAGIC-I camera have improved also the off-axis performance:

¹⁴Crab Nebula Units: units of the VHE flux of the Crab Nebula, considered a "standard candle" in the VHE regime.

a source with a Crab-Nebula-like spectrum, but 80 times weaker, can be detected at the offset of $1^{\circ 15}$ within 50 h of observations. This makes the MAGIC telescopes capable of efficient sky scans.

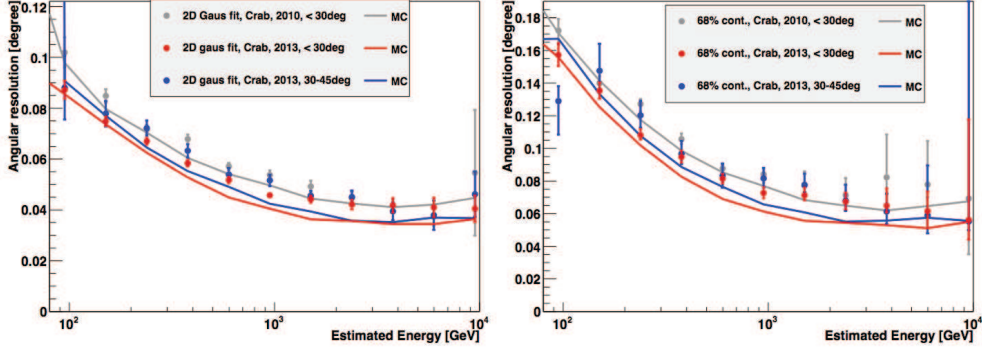


Figure 1.19: Angular resolution of the MAGIC telescopes after the upgrade as a function of the estimated energy obtained with the Crab Nebula data sample (points) and Monte Carlo simulations (solid lines). Left panel: 2D Gaussian fit, right panel: 68% containment radius. Red points: low zenith angle sample, blue points: medium zenith angle sample. For comparison the low zenith angle pre-upgrade angular resolution is shown as gray points [34].

The larger trigger region has allowed also to lower the systematics connected with the background estimation by a factor of 2. From comparisons of reconstructed SEDs of the Crab Nebula for different energy thresholds, the systematic uncertainty in the energy scale has been evaluated to be $<15\%$. The systematic uncertainty on the flux normalization was estimated to be 11-18%, and on the spectral slope ± 0.15 .

Thanks to the improvement in the performance achieved after the upgrade, the MAGIC telescopes have reached an unprecedented sensitivity: since then, more than five new VHE γ -ray sources have already been discovered by MAGIC so far.

¹⁵Less than 30% of the camera FoV.

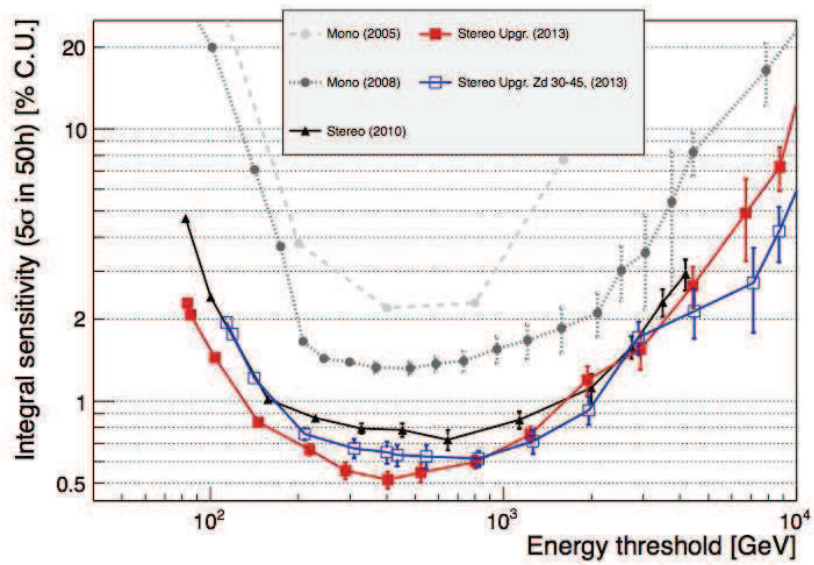


Figure 1.20: Evolution of integral sensitivity of MAGIC telescopes, i.e. the integrated flux of a source above a given energy for which $N_{\text{excess}}/N_{\text{bkg}} = 5$ after 50 h of effective observation time (requiring $N_{\text{excess}} > 10$ and $N_{\text{excess}} > 0.05N_{\text{bkg}}$) Gray circles: sensitivity of the MAGIC-I single telescope with different readouts systems. Black triangles: stereo before the upgrade [32]. Squares: stereo after the upgrade: zenith angle below 30° (red, filled), $30\text{-}45^\circ$ (blue, empty) [34].

Chapter 2

Gamma-Ray Bursts

Gamma-Ray Bursts (GRBs) are the most powerful and bright explosive phenomena observed in the Universe. Given the typical sensitivity of current observing instruments, GRBs take place at the rate of about one per day, and are uniformly distributed over the sky. As explained later, observations show that GRBs are localized at cosmological distances, implying a total time-integrated energy output of about $10^{50} - 10^{53}$ erg. This is roughly 10^{-3} of a solar rest mass, emitted over tens of seconds, it exceeds what than our Sun emits over its ten billion year lifetime, and it exceeds about as much as the entire Milky Way emits over a hundred years; this emission is mainly concentrated into gamma rays.

We also know that typical values of the isotropic-equivalent luminosity L_{iso} for GRBs exceeds the Eddington Luminosity (L_{Edd} ¹) of various orders of magnitude, necessarily implying that GRBs are explosive events.

The first part of a GRB emission, called *prompt* phase, is mainly observed in the keV-GeV energy range: it is short (from milliseconds to minutes), highly variable (with time-scales from milliseconds to tens of seconds) and non-thermal. It is associated to electron acceleration during non-collisional shocks inside highly collimated relativistic jets [128]. In most cases, the *prompt* phase is followed by a so-called *afterglow* phase: the emission decreases with time and is observed at longer wavelengths, from X-rays to radio and optical. It is associated to the deceleration of the relativistic jet in the interstellar medium surrounding the GRB progenitor.

¹ L_{Edd} is the maximum luminosity that a star can achieve before starting to loose its mass because the radiation pressure acting outward exceeds the gravitational force acting inward; $\sim 1.5 \times 10^{35} \frac{M}{M_{\odot}}$ erg/s.

2.1 Historical overview and basic concepts

Well before their detection, GRBs were predicted by Colgate as phenomena associated to relativistic shocks produced during supernovae explosion [58].

GRBs were serendipitously discovered only in 1967 by the military Vela satellites, which were monitoring the Nuclear Test Ban Treaty between the US and the Soviet Union. The announcement was postponed for several years, after having ruled out a man-made origin and ascertained that they were outside the immediate solar system [101]. The first GRB ever observed is GRB670702 (Fig.2.1).

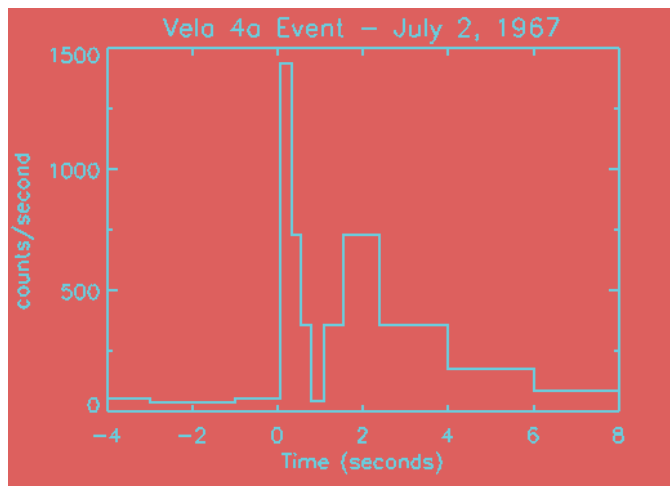


Figure 2.1: Light-curves of GRB670702 as observed by satellites Vela 3 and 4 [101].

After Vela, various gamma-ray instruments performed GRBs observations and several models had been proposed to explain their origin: however instruments of the time had poor positional accuracy and transmitted to Earth only hours after the trigger, so that only wide-field, less sensitive telescopes could follow-up the bursts to look for counterparts at other wavelengths.

A great improvement in GRBs science happened thanks to the *Burst and Transient Source Experiment* (BATSE) onboard the *Compton Gamma-Ray observatory* (CGRO) launched in 1991. Thanks to a very large FoV and wide energy range (15keV-2MeV), between 1991 and 2000 BATSE observed 2704 GRBs [134], while only few hundreds GRBs had been observed before. Moreover, thanks to joint observations performed by the *Energetic Gamma-Ray Experiment Telescope* (EGRET, onboard CGRO too) it was possible to explore GRBs emission up to 30 GeV. Before BATSE, GRBs distances were unknown, but BATSE clearly showed that they were uniformly distributed over the sky (Fig.2.2), thus ruling out a galactic origin.

2704 BATSE Gamma-Ray Bursts

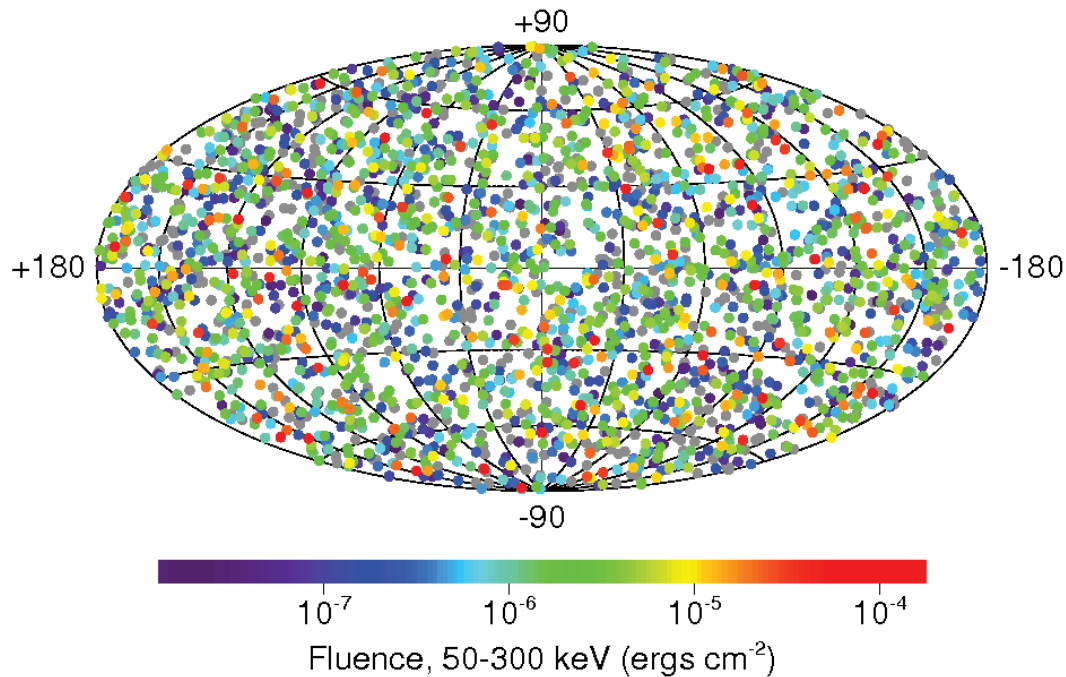


Figure 2.2: Distribution of BATSE observed GRBs over the entire sky in galactic coordinates [115].

The large sample of events observed by BATSE allowed to determine GRBs main features:

- light-curves show high diversity (see e.g. Fig.2.3);
- GRBs can be classified into two main groups, short and long GRBs, according to their duration, with a dividing line at ~ 2 s [102]² (Fig.2.4).

Short bursts are about the 30% of the whole BATSE sample, show different spectral characteristics compared to long bursts, and have a higher hardness ratio³.

The evidence of two different populations of GRBs suggested the existence of two classes of different progenitors.

²Note that the parameter usually used to measure GRBs duration is T90, defined as the time interval over which 90% of the total background-subtracted counts are observed.

³This is the ratio between the fluence measured in the energy range 100-300 keV and the fluence measured in the range 50-100 keV.

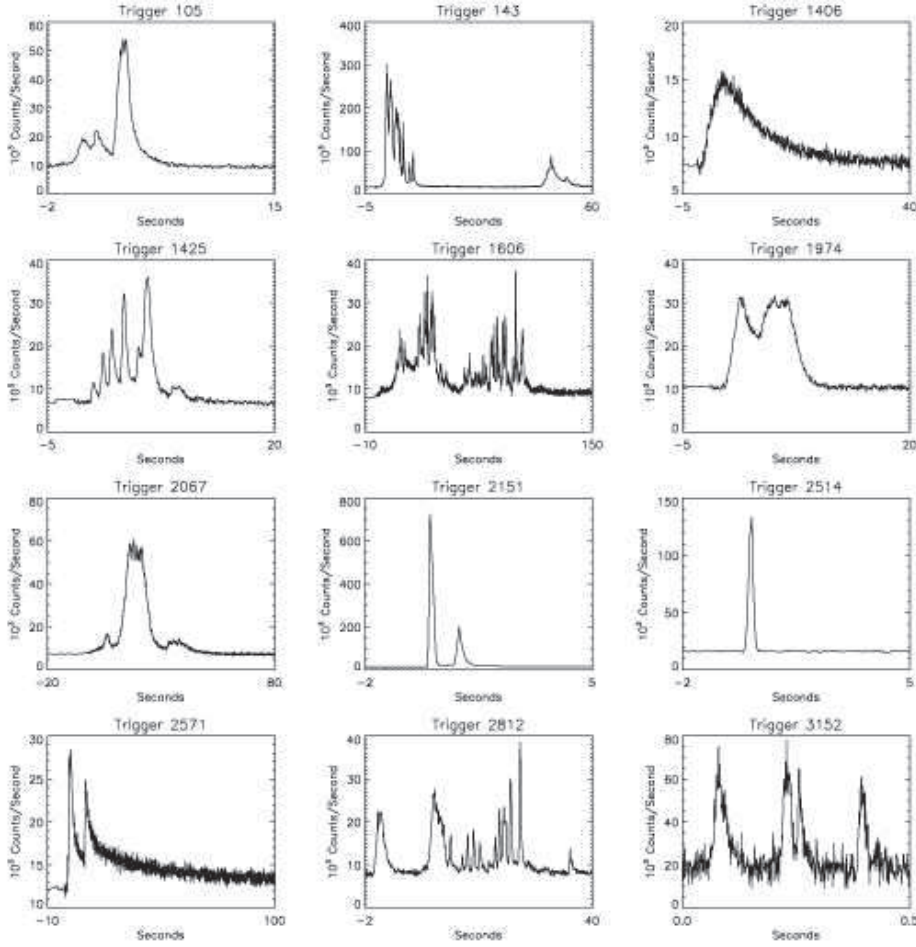


Figure 2.3: A sample of gamma-ray light curves observed by BATSE; figure adapted from [70].

The typical observed GRB's spectrum is non-thermal and shows a hard-to-soft temporal evolution. The function that usually better fits the observed time-integrated spectra of most gamma-ray bursts is the so-called "Band Function" [43], $S(E)$:

$$S(E) \equiv \begin{cases} A \left(\frac{E}{100 \text{keV}} \right)^\alpha \exp\left(-\frac{E}{E_0}\right), & E \leq (\alpha - \beta)E_0 \\ A \left(\frac{\alpha - \beta}{100 \text{keV}} \right)^{\alpha - \beta} \left(\frac{E}{100 \text{keV}} \right)^\beta \exp(\beta - \alpha), & E \geq (\alpha - \beta)E_0 \end{cases} \quad (2.1)$$

where α and β are the low and high energy spectral indexes respectively. The mean values of spectral parameters for brightest GRBs observed by BATSE are: $\alpha \sim -1$, $\beta \sim -2.25$ e $E_0 \sim 250$ keV [147]. The spectral energy distribution νF_ν

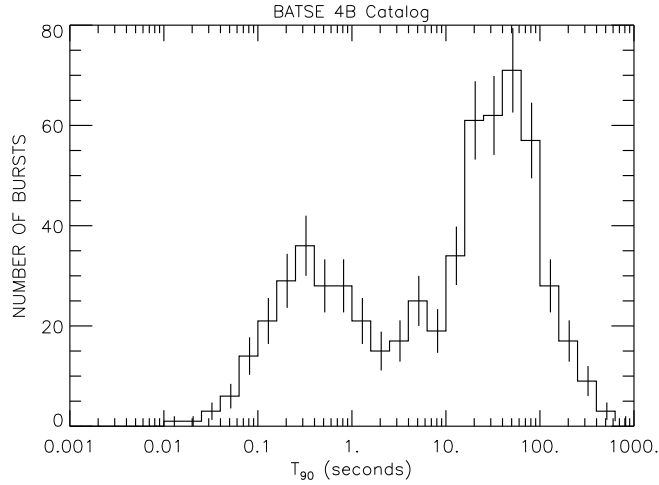


Figure 2.4: Duration (T_{90}) of BATSE GRBs. The bimodal distribution suggests that GRBs belong to two different classes, separated by $T_{90} \sim 2$ s [134]

peaks at $E_p \equiv (2 - \alpha)E_0$. This observed prompt emission is usually associated to synchrotron radiation produced by electrons accelerated in internal shocks with a power-law energy distribution.

Despite the optical and X-ray counterparts of GRBs had been already theoretically predicted [156, 119], the first instrument that could localize bursts with accuracy (≤ 10 arcmin) necessary make possible follow-ups by radio and optical telescopes was the Italian-Dutch satellite BeppoSAX that was launched in 1996. One of the first long bursts detected was GRB970228 (Fig.2.5): thanks to the localization and observation of the optical counterpart it was possible to identify the host galaxy at redshift $z = 0.498$: this was the first empirical evidence that long GRBs have a cosmological origin [66].

The measurement of the distance allowed also to study the GRBs intrinsic properties, and in particular the huge energetic release in gamma rays. For example, the typical fluence observed by BATSE ($10^{-5} \text{ erg cm}^{-2}$) corresponds to an isotropic emitted energy $E_{\text{iso}} \simeq 10^{53}$ erg.

The first observation of the afterglow associated to a short GRB was performed by the Swift satellite launched in 2004. Swift can locate a burst with an accuracy of about 2 arcminutes; this position is used to automatically slew the spacecraft, typically within less than a minute, to re-point towards the event. The positions are also rapidly sent to Earth so that ground telescopes can follow the afterglows. Swift observations allow to study in detail the transition between the prompt and the afterglow phase.

X-ray afterglow (see, e.g., Fig.2.6) usually shows an initial very steep time decay,

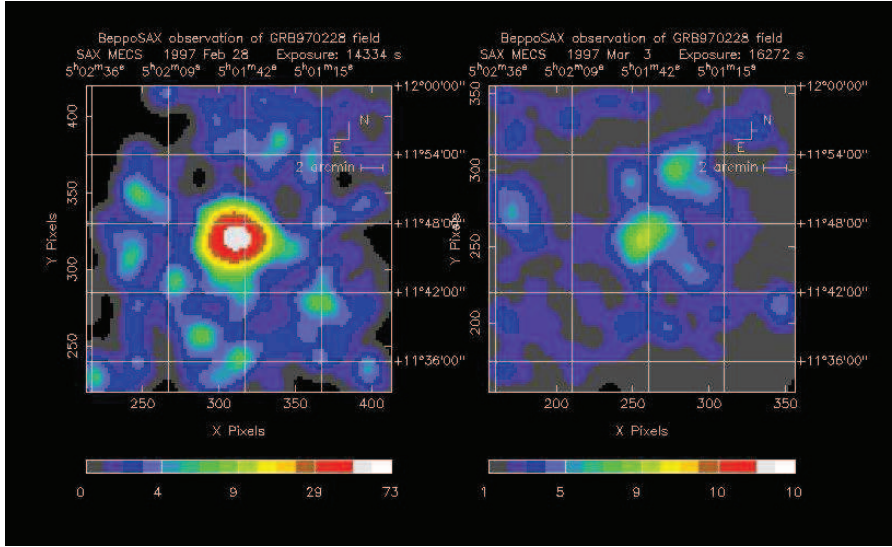


Figure 2.5: Localization of GRB970228 observed by Beppo-SAX. The image on the left (right) shows the X-ray emission coincident to the gamma one, observed ~ 8 h (3 days) after the trigger [5].

starting after the end of the prompt γ -ray emission. This is generally followed by a much shallower time decay, often punctuated by abrupt, large amplitude X-ray flares, lasting for up to ~ 1000 s, which then steepens into a power law time decay with the more usual (pre-Swift) slope of index of roughly -1.2 to -1.7 [182]; a final further steepening is sometimes detected. These structures in the X-ray afterglow light curves are present, both, in long and short bursts.

Swift found that long GRBs are in galaxies where massive stars ($M \gtrsim 30 M_{\odot}$) are forming, over a large redshift range from $z = 0.0085$ to $z > 8$ (see e.g. [172, 60]); when they occur close enough for supernova detection, they are found to have an accompanying Type Ib or Ic supernova, supporting the evidence that long bursts are caused by the collapse of the central core of a massive star in a compact object.

With the increasing statistics, long GRBs are contributing to a better understanding of the high-redshift universe. They provide spectroscopic information about the chemical composition of the intervening intergalactic medium at epochs when the Universe was as young as 1/20th of its present age. Also, since long GRBs are the endpoints of the life of massive stars, their rate is approximately proportional to the star formation rate. This gives more accurate information at high redshift, where the rate is highly uncertain.

As already said, Swift succeeded in finally localizing the host galaxies of a number of short GRBs (e.g. [46, 73]). Unlike long GRBs, the short GRBs typically

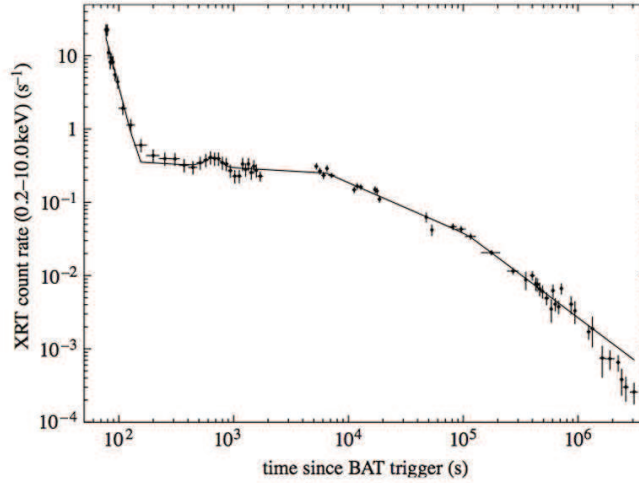


Figure 2.6: Light curve of GRB060428A observed by Swift XRT [50].

originate in host galaxies with a wide range of star formation properties, including low formation rates. The host properties are substantially different from those of long bursts ([71, 72, 106]), indicating a different origin. Furthermore, nearby short GRBs show no evidence for simultaneous supernovae [127]. These results reinforce the interpretation that short GRBs arise from an old population of stars, probably due to mergers of compact binaries such as double neutron stars or neutron star-black hole [127, 69, 135]. Short GRBs are found to have generally a lower isotropic-equivalent luminosity and total energy output, typically $E_{iso} \sim 10^{50}$ erg, and a weak afterglow.

2.1.1 Models for GRBs emission

Despite the fact that GRBs have been object of study since almost 50 years, their detailed physics is still partially unknown and even well accepted theoretical models still leave open questions. The above cited fast variability ($\Delta t \gtrsim 1$ ms) observed during the prompt phase puts limits on the typical dimension of the central engine: $R \lesssim c\Delta t \sim 100$ km. Moreover, if we consider that the central engine has a dimension that equals at least one Schwarzschild radius ($R_{Sch} = 2MG/c^2$), we can estimate the limit on mass of the progenitor as

$$R > R_{Sch} \Rightarrow M \leq \frac{c^3 \Delta t}{2G} \sim 100 M_{\odot} \quad (2.2)$$

This means again that the natural candidates for GRBs' progenitors are compact objects originated from stellar collapse: a black hole and a short-lived accretion

disc are thought to be formed after the core collapse (long GRBs) or binary merger (short GRBs).

The gravitational binding energy of the system is released within a short time scale, which eventually produces the GRB phenomenon when some fraction of the gravitational energy converts to gamma rays. This is done *via* accretion of material/gas onto the black hole. Infalling gas onto the newly-formed black hole is accreted with high efficiency. Most of the gravitational energy, $\sim 10^{54}$ erg, is radiated in ~ 10 MeV thermal neutrinos (as in core-collapse supernovae) and a lesser amount in gravitational waves. Only a small fraction, $\sim 10^{51}$ erg, is converted to a GRB fireball, which eventually produces a highly-relativistic bi-polar jet, and is responsible for the observed high-energy emission [78].

The observed spectrum extends to high energies, generally in a broken power law shape, i.e. it is highly non-thermal.

Two problems with the first expanding **fireball models** were (see [135] and [166] for details):

- they are initially optically thick and the photon spectrum escaping from the Thompson scattering photosphere would be expected to be an approximate blackbody;
- most of the initial fireball energy would be converted into kinetic energy of expansion, with a reduced energy in the observed photons, i.e. a very low radiative efficiency.

A simple way to achieve a high efficiency and a non-thermal spectrum, which is currently the most widely invoked explanation, is by reconvertng the kinetic energy of the flow into random energy *via* shocks, after the flow has become optically thin.

In the **internal-shocks model** electrons in the internal shock emit synchrotron and inverse Compton radiation, leading to the above cited non-thermal broken power law photon spectrum, roughly similar to the observed "Band" spectra: this model is the most widely used to interpret the prompt keV-MeV emission [117, 155].

In the **external-shocks model** the expanding fireball runs into the interstellar medium or a pre-ejected stellar wind, driving a forward shock into the external gas and a reverse shock that propagates back into the ejecta. This model is the favored interpretation for the observed afterglows starting early in gamma-rays (the so called early-afterglow, see e.g. [81, 61, 105]) and phasing into gradually longer wavelengths over periods of days to months. The reverse shock would lead to optical photons, while inverse Compton emission in the forward blast wave would produce photons in the multi-GeV range [116]. Prompt optical afterglows were first detected in 1999 [30], while multi-GeV emission was reported for the first time by CGRO-EGRET [98], but observed more recently and with more details by Fermi-LAT (see Section 2.2).

Any of these models provide a generic scenario for explaining the radiation spectrum, and they are largely independent of the specific nature of the progenitor.

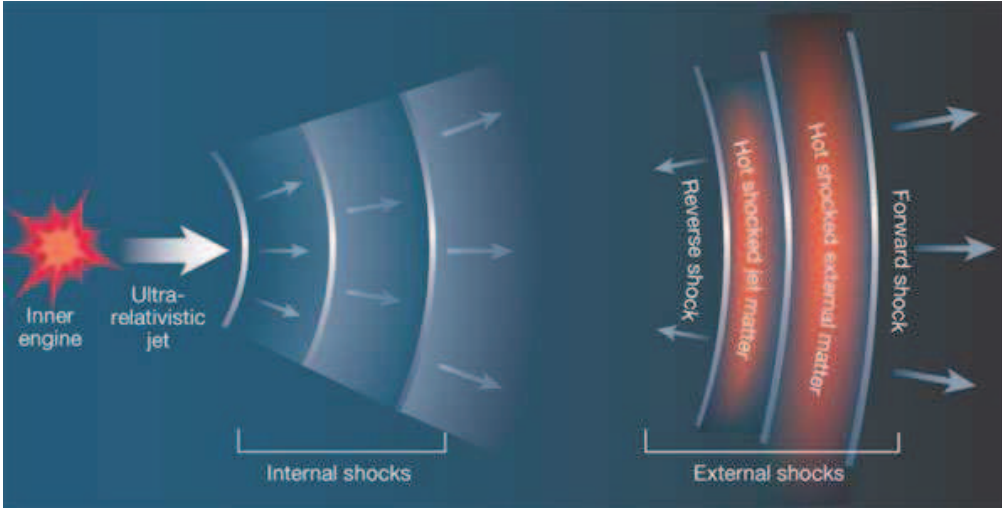


Figure 2.7: Schematic view of the **fireball model**: internal shocks reproduce the observed prompt keV-MeV emission while external shocks explain the later time afterglows from gamma to X, optical and radio wavelengths [144].

A problem with simple internal-shock synchrotron models of the prompt MeV emission is that the low energy photon number spectral slope, which is expected to be $-2/3$, is found to be flatter in a fraction of BATSE bursts [146]. In addition, the synchrotron cooling time can be typically shorter than the dynamical time, which would lead to slopes $-3/2$ [80]. A solution involves the presence of a **photospheric component**. An important question is whether the observed clustering of spectral peak energies in the 0.1-0.5 MeV range is intrinsic or rather due to observational selection effects. A preferred peak energy may be attributed to a blackbody spectrum at the comoving pair recombination temperature in the fireball photosphere [68]; a photospheric component can address also the above low-energy spectral slope issue with its steep Rayleigh-Jeans part of the spectrum, at the expense of the high energy power law. This was generalized by [118] to a photospheric blackbody spectrum at low energies with a comptonized photospheric component and possibly an internal shock or other dissipation region outside it, producing Fermi accelerated electrons and synchrotron photons at high energies.

The presence of a photospheric component in Fermi-LAT detected GRBs has been reported by several authors (e.g. [158, 138, 85, 41, 121]). In particular, Guiriec et al. 2015 [86] shows that GRBs spectra can be fitted using an empirical model composed of three components: (i) a black-body (BB) component that may be

interpreted as the photosphere emission of a magnetized relativistic outflow, (ii) the Band component as synchrotron radiation in an optically thin region above the photosphere, either from internal shocks or magnetic field dissipation, and finally (iii) an extra PL component extending to high energies likely having an inverse Compton origin even though its extension to a much lower energy remains a mystery.

As shown in section 2.3.2, the presence of such BB component has been tested in the analyses performed in this thesis.

Internal Absorption Processes

It is expected somehow that high-energy gamma rays inside a high-density fireball can be attenuated by various processes (e.g. Compton scattering, pair production) contributing to the fireball opacity.

The dominant process is pair production: two photons having energy ϵ_γ and $E \gtrsim (m_e c^2)^2 / 2\epsilon_\gamma$ (where m_e is the electron rest mass) annihilate producing an electron-positron couple ($\gamma\gamma \rightarrow e^- e^+$)

Unfortunately it is likely that the fireball opacity is quite different from one burst to another, depending on the local conditions. The opacity of the emitting region depends on the radiation density. When this parameter is high, there is also a high abundance of relatively low-energy photons that represent a target for high-energy photons. The radiation density is directly proportional to the luminosity of the emitting region and inversely proportional to its dimension that, as already said, can be inferred by the variability time-scale of the light-curve during the prompt phase. In fact, every peak of the prompt light-curve is related to the thickness of the region where the internal shock is taking place.

After Fermi observations of cut-off signatures in the spectra of some GRBs, it has been shown (see e.g. [21, 171]) that a direct measurement of the bulk Lorentz factor (Γ) can be done through a clear detection of a spectral break (E_c) in GRBs spectra if assuming that it's due to internal absorption process. The presence of such cut-off spectral feature has been also tested in the analyses performed in this thesis (section 2.3.2).

Unfortunately, even in the case of a clear detection of such a cut-off, determining its origin remains a big challenge. In fact internal absorption, or a roll-over in the energy of the emitting particles, or an external absorption (due for example to the extragalactic background light if the redshift of the source is high-enough) are all suitable candidates for the explanation of such a spectral feature. Still, the detection or non-detection of high-energy photons in GRBs' spectra can be used to put useful limits on the bulk Lorentz factor.

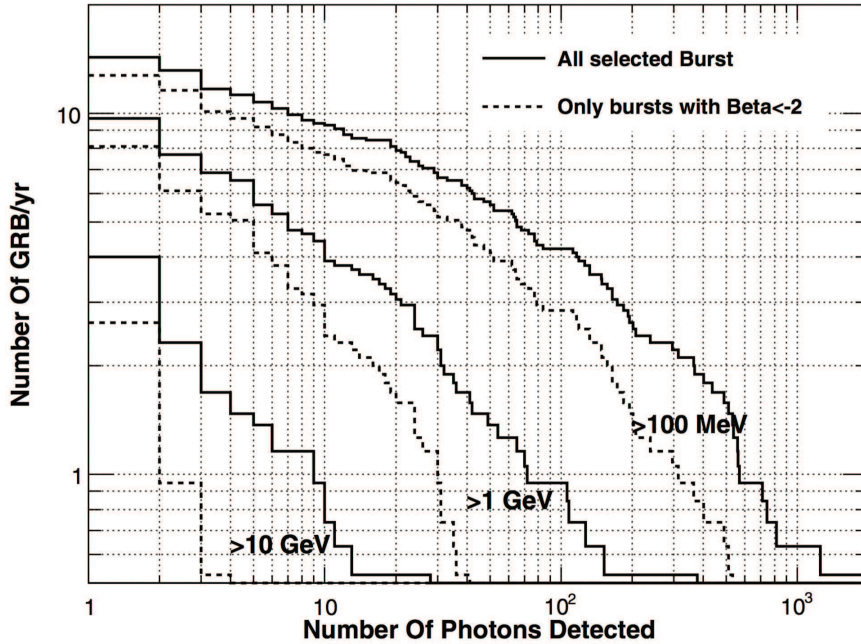


Figure 2.9: Predicted number of GRBs observed per year as a function of the number of detected photons for different energy threshold [44].

Taking into account only bursts with at least 10 photons detected with energy > 100 MeV we obtain a rate of almost ~ 7 bursts observed per year. This is slightly below the pre-lunch estimate of ~ 9 bursts per year (Fig.2.9 [44]). The discrepancy can be due to systematic uncertainties, different background estimations or to the fact that those predictions were made extrapolating the GRBs spectral shape obtained from the GRBs observed by BATSE to the one covered by the LAT. Moreover, it suggests that the high-energy component is not an ubiquitous characteristics of GRBs, and that it can be suppressed by the presence of a spectral cut-off, as observed in the case of GRB 090926A [21]. In any case the rate of high-energy GRBs detections achieved by the LAT is impressive, especially when compared to its predecessors EGRET (5 GRBs in 10 years) and AGILE (7 GRBs in 8 years).

The detailed study of LAT detected bursts allowed to uncover new and unexpected properties of the high-energy emission from GRBs shedding light on physics mechanisms, such as particle acceleration and emission processes in ultra-relativistic regime.

Here I will briefly show the features of GRBs observed at high energies as reported in [17], then I will report about the unique characteristics of GRB 130427A,

and will introduce the recent improvements in GRBs search implemented by the LAT team.

Delayed onset and extended duration

The emission above 100 MeV is systematically delayed with respect to the low-energy emission seen in the keV-MeV energy range. This was observed for the first time for GRB 080916C where the first peak visible in the GBM light curve is completely missing in the LAT one (Fig.2.10). Moreover, the emission above 100

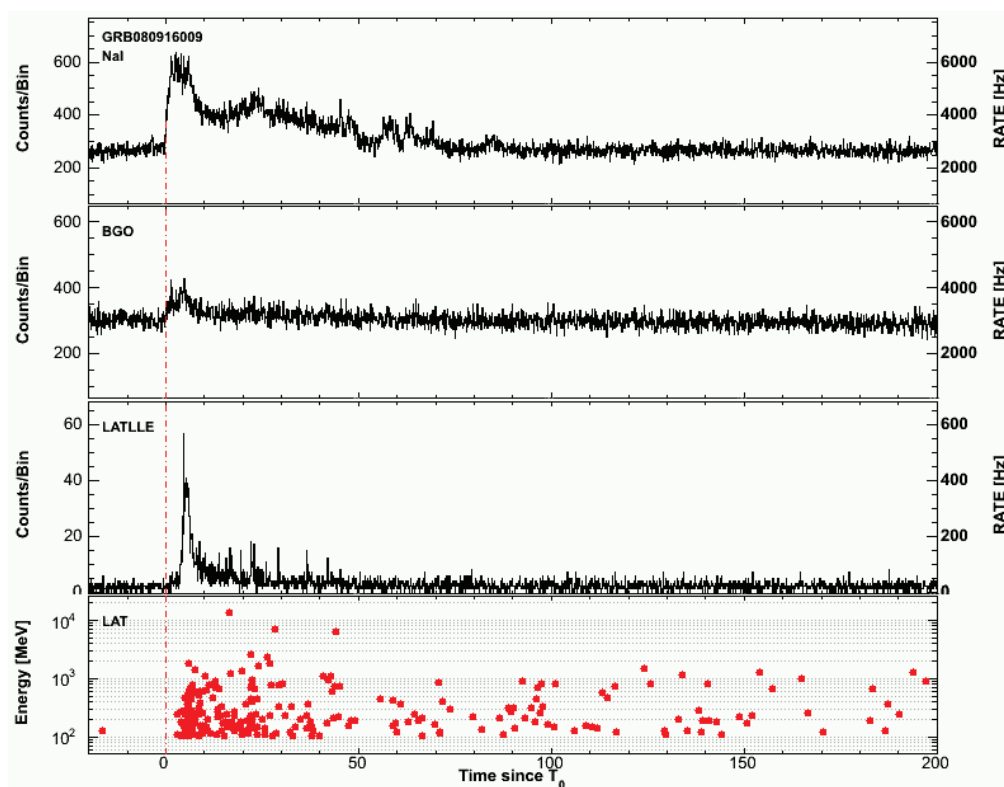


Figure 2.10: Composite light-curve of GRB 080916C as seen by Fermi in different energy bands [17].

MeV is also systematically longer than the prompt emission, and decays smoothly as a power law with a typical decay index of -1, pointing to a different physical origin with respect to the spiky prompt emission observed at lower energies.

Several models have been proposed to explain the delayed emission. Early afterglow models [104, 81] could explain the observed time decay, the delayed onset and the out-flow deceleration time scale, and the lack of variability. In particular

the value of the decaying index is foreseen by the standard afterglow model for an adiabatic expansion of the fireball while a radiative expansion would foresee a decay with an index of $10/7$, which is not observed in the LAT data. Hadronic models could explain these features as well: the onset delay could be the time to produce electromagnetic cascades [65, 87, 36], or the time required to accelerate, accumulate, and cool down relativistic protons via proton-synchrotron emission in a very strong magnetic field [152]. Energy-dependent delays would also be expected in proton-synchrotron models when the cooling break shifts to lower energies at later times.

Additional spectral component

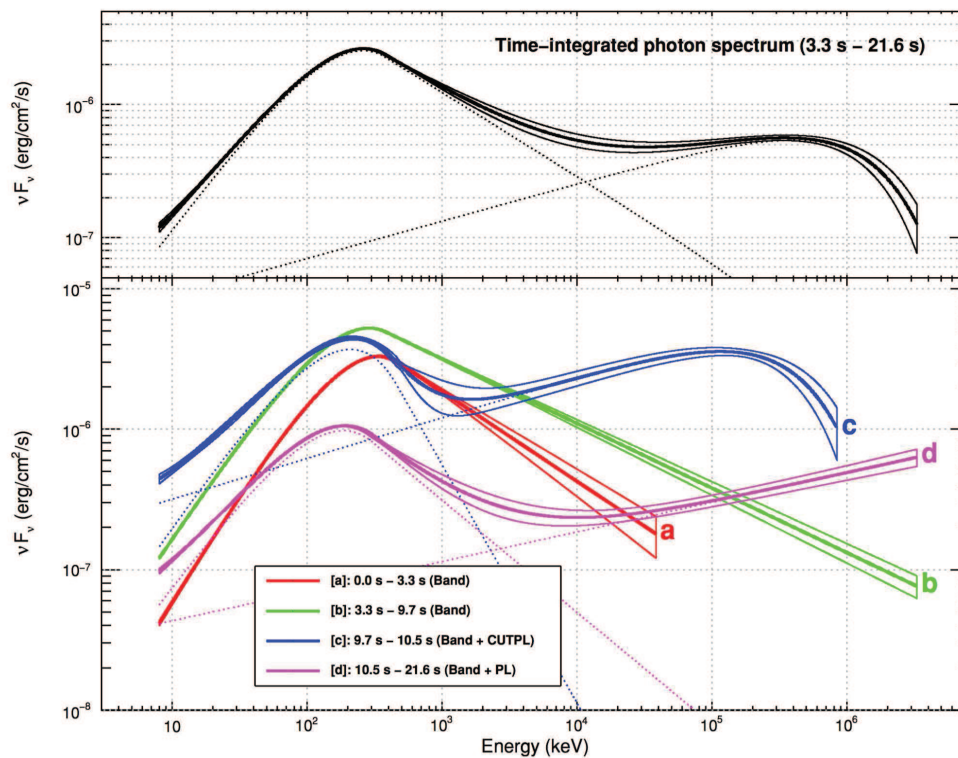


Figure 2.11: Top: the best-fit (Band+CUTPL) model for the time-integrated data of GRB 090926A plotted as a νF_ν spectrum. The two components are plotted separately as the dashed lines, and the sum is plotted as the heavy line; 1σ error contours are also shown. Bottom: the νF_ν model spectra (and 1σ error contours) plotted for each of the time bins considered in the time-resolved spectral analysis. Plot and capture taken from [21].

While the prompt emission of most GRBs have been successfully described in the past with the Band function [43], the spectra of brightest GRBs observed by the LAT require additional components, such as power laws, high-energy cut-offs, or both, to account for high-energy data. The first GRB observed by LAT showing an additional power-law spectral component was GRB 090510. For GRB 090926A instead the fit improves adding to the power-law a spectral break component (CUTPL) around 1.4 GeV (Fig.2.11). Other GRBs, observed at low off-axis angles, and with a corresponding high effective area, show deviations as well. Finally, as already mentioned, the presence of a BB photospheric component has been found in some GRBs' spectra.

This means that the empirical Band model seems to be inadequate to describe all the spectral features of LAT GRBs. Different components can be required depending on the particular event: this calls for a better broad-band modeling of the prompt spectra of GRBs, opening new questions and calling for new theoretical developments.

Fluence and Energetics

Generally speaking, LAT detected GRBs are among the most energetic revealed by GBM and populate the right tail (Fig.2.12, left panel) of the distribution of fluence values calculated in the GBM catalog [82].

The distribution of the fluence values for LAT detected GRBs suggests the existence of an hyper-energetic class of events characterized by a ratio between high- and low-energy fluence much larger than the others. For these GRBs, GBM measured high fluence values too (Fig.2.12, right panel).

LAT short GRBs ($\sim 7\%$ of the total sample, significantly smaller than the $\sim 20\%$ observed by GBM) also show values for the ratio between high-energy and low-energy fluence quite higher compared to long bursts (Fig.2.12, right panel). This is in agreement to previous observations assessing that short bursts are harder than long ones.

GRB 130427A

The observations of the exceptionally bright GRB 130427A by Fermi provide further constraints on the GRB phenomenon and their emission processes. The initial pulse (up to 2.5 seconds) is the brightest well-isolated pulse observed to date. A fine time resolution spectral analysis led by the Fermi-GBM team [145] highlighted how difficult it is for any of the existing models to account for all of the observed spectral and temporal behaviors simultaneously. Furthermore, GRB 130427A had the largest fluence, highest observed energy photon (95 GeV), longest gamma-ray duration (20 hours), and one of the largest isotropic energy releases

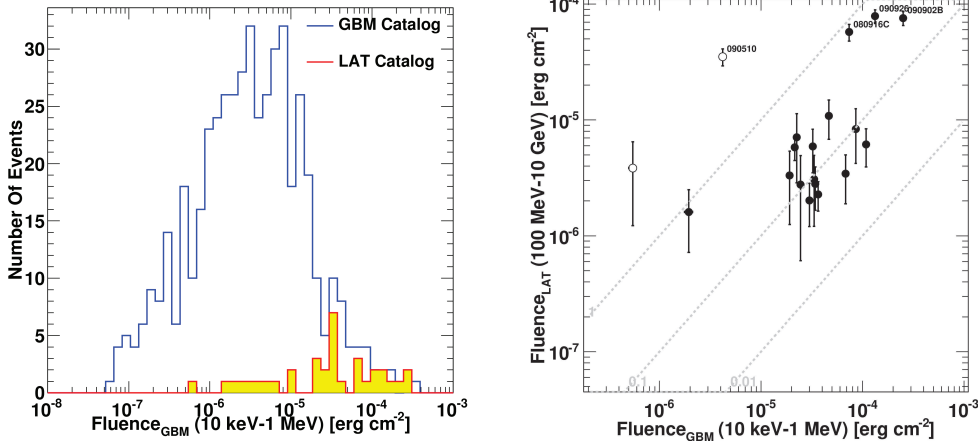


Figure 2.12: On the left: distribution of fluence values measures in the energy band 10 keV - 1 MeV for LAT detected GRBs (yellow) compared with the sample of LAT detected GRBs reported in [82]. On the right: fluence measured by the LAT (100 MeV - 10 GeV) Vs fluence measured by GBM (10 keV - 1 MeV); discontinued lines show the 100%, 10% e 1% threshold for their ratio; empty circles indicate short GRBs [17].

ever observed from a GRB. The temporal and spectral analyses of GRB 130427A presented by the Fermi/LAT Team in [18] challenge the widely accepted model that the non-thermal high-energy emission in the afterglow phase of GRBs is synchrotron emission radiated by electrons accelerated at an external shock.

Towards the second LAT GRBs catalog

The Fermi-LAT collaboration is currently actively working to produce the second GRB catalog, covering the eight years of the mission. This catalog will contain more GRBs, not only because of a longer period of data acquisition, but also thanks to renewed algorithms to search on a wider angular region centered on GBM-GRB trigger positions, and to the last LAT data selection (the already cited Pass8), with larger effective area both at low and at high energies.

Starting from the results obtained in the first LAT GRB catalog and thanks to the developments in the understanding of the systematic errors on GBM localizations [59], a new detection algorithm (presented in detail in [177]) has been developed and tested by the LAT collaboration which increases the number of detections by more than 45%. It consists of 10 searches running in parallel over time intervals logarithmically spaced from the trigger time to 10 ks after that. In case of

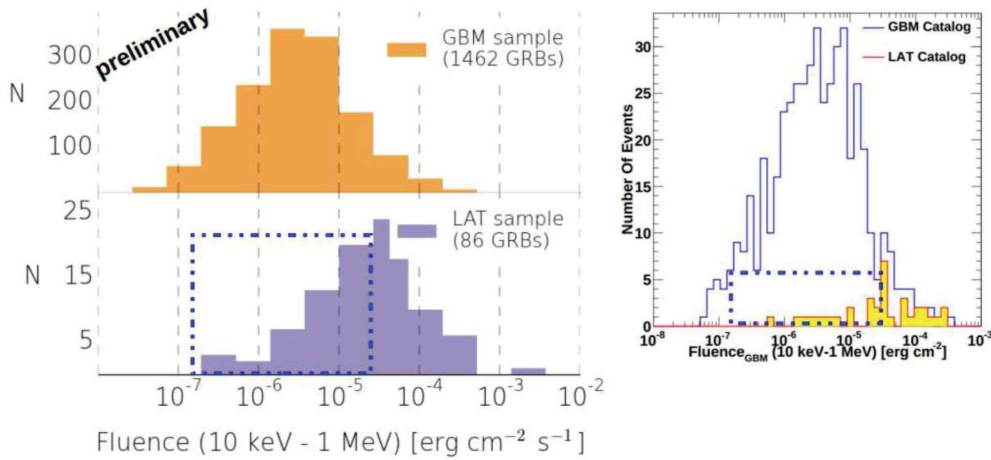


Figure 2.13: Left panel: low-energy fluence distribution for the whole GBM sample (upper panel) and for the sample detected with the new algorithm in LAT data (lower panel). Right panel: similar plot from the first LAT GRB catalog [17]; the blue dashed line marks the region where most of the new detections lie, showing the increased sensitivity of the new algorithm with respect to the old one [177].

a GBM trigger, for each of these time intervals the algorithm creates a grid covering a "searching" map of 30×30 deg, thus covering the GBM position uncertainty. For each point of the grid, a likelihood analysis is performed and a test statistics (TS) value is computed: the maximum of the TS in the map is considered as the best guess for the position of the new transient. A new likelihood analysis is finally performed on this position, and if the TS from this final analysis is above a certain threshold, it is considered a new detection. When the automatic search is completed, each new detection is then carefully checked manually by two LAT members in order to exclude false GRBs detections due, e.g., to earth limb in the FoV, or flaring nearby galactic or extragalactic known sources; I am currently actively involved in this effort.

Combining the specialized search algorithm with the Pass8 event selection, a large enhancement in the detection of faint high-energy GRB counterparts is achieved (see Fig.2.13), increasing the efficiency of detection by more than 60% and yielding more than 100 bursts over the time span of the Fermi mission (see Fig.2.14). The analysis and characterization of this new sample is currently in progress. When completed, it will help to settle some open questions, which could not be deeply answered in the first catalog due to the limited statistics, such as the existence of a separate population of hyper-energetic events, the nature of the fire-

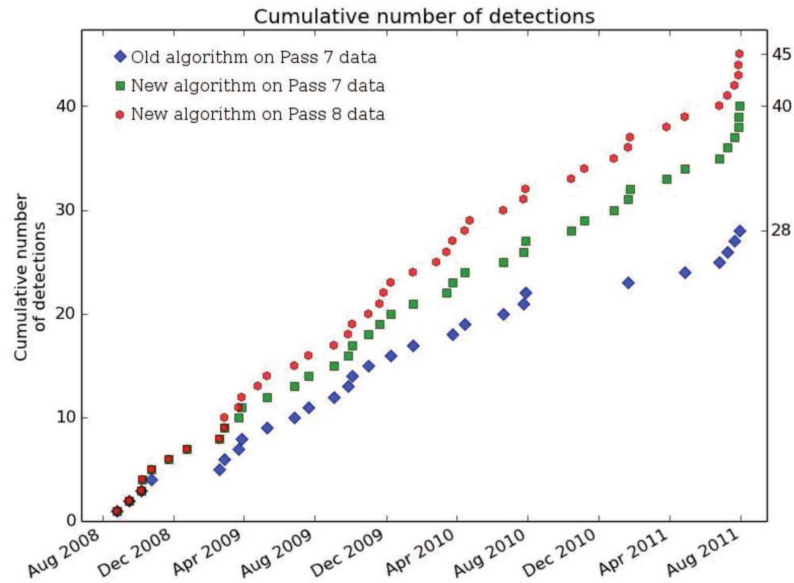


Figure 2.14: Cumulative detections for the time span covered by the LAT GRB catalog. The new analysis yields 45% more detections than the one used in the catalog when run on the same data (blue and green), and 60% more with Pass8 data (red) [177].

ball expansion, and how common are spectral cut-offs and additional components. Related results are detailed in Par.2.3.2.

Finally, using a preliminary version of Pass8 data, the LAT collaboration re-analyzed the prompt phase of ten bright GRBs previously detected by the LAT [39], finding four new gamma rays with energies greater than 10 GeV in addition to the seven previously known. Among these four there is a 27.4 GeV gamma-ray from GRB 080916C, which, at a redshift of 4.35, makes it the gamma-ray with the highest intrinsic energy (147 GeV) detected so far from a GRB.

2.3 The sample of LLE detected GRBs: GBM and LAT spectral analysis

This section is devoted to the spectral analysis of GRBs that have been significantly detected through the LLE events selection using both LLE and GBM data. The whole sample is composed of ~ 55 GRBs but I will focus on the twenty-five events that have been already included in the first GBM spectral catalog [84]; from now on I will refer to this sample of GRBs as the "GBMcat-sample". For each of these bursts, the GBM team provided a list of best detectors and of time-intervals suitable for spectral analysis. This is very useful: since the goal of this analysis is to fully characterize the spectra of these bursts constraining the possible additional spectral components, I want to avoid to introduce fake spectral features because of a not-accurate background subtraction or because a wrong choice of occulted detectors.

2.3.1 Analysis methods: background estimation and fitting techniques

Tab.2.1 shows the list of GRBs in the GBM-cat sample together with some additional information: GBM trigger time (expressed in MET⁶), the start and end of LLE-detected emission (t_i and t_f), the reprocessing of LLE data used for the spectral analysis (IRF).

I developed an analysis pipeline that automatically performs these steps:

- download GBM and LLE data from public repositories: the "Fermi-GBM Trigger catalogs"⁷ and the "Fermi Fermi LAT Low-Energy Events Catalog"⁸, respectively;
- perform the fit of the background for GBM data using informations about the right detectors and time interval provided by the GBM team;
- produce the source spectrum for GBM and LLE data on LLE detection time-interval.

A completely automated procedure to perform the fit of the background for LLE data is not possible. I then looked at the light-curves and choose two time-intervals in the off-pulse region, one just before the pulse and one just after: these time

⁶Mission Elapsed Time: the number of seconds since midnight at the beginning of January 1, 2001, in the UTC system.

⁷<https://heasarc.gsfc.nasa.gov/W3Browse/fermi/fermigtrig.html>

⁸<https://heasarc.gsfc.nasa.gov/W3Browse/fermi/fermille.html>

| name | GBM trigger time | t_i | t_f | IRF |
|-------------|------------------|--------|--------|-------|
| bn080825593 | 241366429.105 | -0.601 | 19.399 | P8V2 |
| bn080916009 | 243216766.613 | -4.395 | 45.805 | P8V2 |
| bn081024891 | 246576161.864 | -1.652 | 1.348 | P8V2 |
| bn081224887 | 251846276.414 | -0.514 | 0.486 | P7V6 |
| bn090217206 | 256539404.558 | 4.959 | 14.959 | P7V6 |
| bn090227772 | 257452263.407 | -0.962 | 2.038 | P7V6 |
| bn090323002 | 259459364.627 | 4.653 | 85.053 | P7V6 |
| bn090328401 | 259925808.511 | 6.01 | 26.11 | P7V6 |
| bn090510016 | 263607781.971 | -5.029 | 15.071 | P7V6 |
| bn090902462 | 273582310.313 | 4.905 | 45.105 | P7V6 |
| bn090926181 | 275631628.987 | -0.066 | 20.134 | P7V6 |
| bn091031500 | 278683230.846 | -5.041 | 15.059 | P7V6 |
| bn100116897 | 285370262.242 | 83.257 | 103.36 | P7V6 |
| bn100225115 | 288758733.147 | 5.515 | 15.515 | P7V6 |
| bn100724029 | 301624927.992 | 4.977 | 95.377 | P7V6 |
| bn100826957 | 304556304.898 | 2.956 | 43.056 | P7V6 |
| bn101123952 | 312245496.974 | 43.304 | 53.304 | P7V6 |
| bn110328520 | 323008161.194 | -0.6 | 19.4 | P7V6 |
| bn110529034 | 328322924.872 | -0.552 | 0.448 | P7V6 |
| bn110721200 | 332916465.761 | -5.76 | 4.34 | P7V6 |
| bn110731465 | 333803371.954 | -5.049 | 15.051 | P7V6 |
| bn120226871 | 351982459.027 | 5.926 | 26.026 | P7V6 |
| bn120328268 | 354608782.953 | -0.777 | 9.223 | P7V6 |
| bn120624933 | 362269436.934 | -300.0 | 50.0 | P7V6 |
| bn120709883 | 363561103.367 | 0.0 | 5.0 | P7REP |

Table 2.1: List of GRBs in the GBM-cat sample together with some additional information: the GBM trigger time (MET), the start and end of LLE-detected emission (t_i and t_f , expressed in seconds), the reprocessing of LLE data used for the spectral analysis (IRF).

intervals have to be close to the burst interval, should have a long enough duration, and should not contain structures in the light curve. The background fit itself is then done using a polynomial function.

After this step, all GRBs are automatically analyzed using the tool XSPEC⁹ [35] following the procedure described in [17].

After loading the data and response matrices in XSPEC, I excluded from the fit all the NaI channels between 33 keV and 36 keV (corresponding to the Iodine K-edge, see [114]), and I ignored the channels at the boundaries of the GBM spectra (channels below 8 keV and channels 127 and 128 for NaI; channels 1, 2, 127, and 128 for BGO). For LLE data, I kept all data between 30 MeV and 100 GeV, following the prescriptions at the web-page "Caveats About Analyzing LAT Pass8 Data"¹⁰. I jointly fitted the GBM and LAT data with several models (described below), minimizing the negative log-likelihood. This likelihood function, called "PG-stat", is derived from a joint probability distribution, obtained by modeling the spectral counts as a Poisson process and the background counts as a Gaussian process. The fitting algorithms find local minima for the statistic, but can then fail to converge to the global minimum. To mitigate this problem, I performed multiple fits for each model, each time starting from a different set of values for the parameters, and keeping as the best fit the set giving the lowest overall value for the statistic.

The base model used to fit the overall spectrum is the already mentioned Band Model [43]: two power laws joined by an exponential cutoff

$$N(E) \equiv \begin{cases} AE^\alpha e^{-\frac{E}{E_0}}, & E \leq (\alpha - \beta)E_0 \\ A[(\alpha - \beta)E_0]^{\alpha - \beta} E^\beta e^{\beta - \alpha}, & E \geq (\alpha - \beta)E_0 \end{cases} \quad (2.3)$$

$N(E)$ is the differential photon flux (in units of $\text{cm}^{-2} \text{s}^{-1} \text{keV}^{-1}$) expected from a model at a given energy E (in keV), and A is a normalization constant whose units depend on the model. E_0 (keV) is called the e-folding energy while the peak energy $E_p = (2 + \alpha)E_0$; α and β are respectively the (asymptotic) photon index at low energy and the photon index at high energy.

The additional components tested are:

- an exponential cut-off: e^{-E/E_c} , where E_c is the cutoff energy;
- a power-law, $N(E) \equiv AE^{-\lambda}$ where λ is the photon index;
- a Comptonized model (a power law with an exponential cutoff), $N(E) \equiv AE^{-\lambda} e^{-E/E_c}$.

⁹<http://heasarc.gsfc.nasa.gov/xanadu/xspec/>

¹⁰http://fermi.gsfc.nasa.gov/ssc/data/analysis/LAT_caveats.html

Finally a black-body (BB) component whose temperature is expressed in keV (kT) has been additionally tested.

To take into account the unknown uncertainties in the inter-calibration between the different detectors, I apply an effective area correction [47] for the four brightest bursts: bn080916009, bn090510016, bn090902462, bn090926181¹¹. It consists in scaling the model by a multiplicative constant, with the constant being fixed to 1 for the LLE data (taken as reference), and leaving the parameter free for all the other detectors. As it is reported in [17], adding such a correction does not change the results in the fitting of fainter bursts because in this case statistical errors dominate over the inter-calibration uncertainties.

2.3.2 Results and Discussion

The results of the composite spectral analysis are shown in Tables from 2.2 to 2.9.

For each burst I show here the model that gives the lower value of ratio between the PG-stat ("Statistic" in the tables) and the number of degrees of freedom (DoF). A more complex model is preferred only if the added complexity is justified by the increase in statistical significance following the prescription in [17].

For eight GRBs in the sample, I show the results for two models and not only one: this is due to the fact that it is not possible to choose the best model comparing the PG-stat value when the models to compare are not nested¹². In this case it would be necessary to perform dedicated simulations for each burst in order to finally distinguish between the two preferred models.

In fifteen cases, a BB seems also required to describe the observed spectrum at low energies; the observed kT values span the range from ~ 500 to ~ 750 keV and are usually well constrained. Evidence for a photospheric component has been already reported in the spectrum of, e.g., GRB 080916C and 090926A [86], 110721 [41], 080825 [121], 090902 [183].

Fig. 2.15 shows a summary of results obtained from the fit¹³: the values obtained when a BB component is required are in grey while parameters for other models are shown in yellow.

The mean values found for α , β and E_p are: -1.2, -2.9 and 1.02 MeV respectively. Note that the β index results steeper when a Black-body component is not included in the fit. Anyhow the analysis of the whole sample of LLE detected GRBs and the simulations needed to distinguish between different models are fundamental to

¹¹These GBM triggers refers to the famous bursts GRB 080916C, 090510, 090902, 090926A. For simplicity, from now on I will refers to GRBs always using the GBM trigger identifier.

¹²Two statistical models are nested if the first model can be transformed into the second model by imposing constraints on the parameters of the first model.

¹³Note that here I'm showing only the results fro the model that gives the lower PG-stat/DoF.

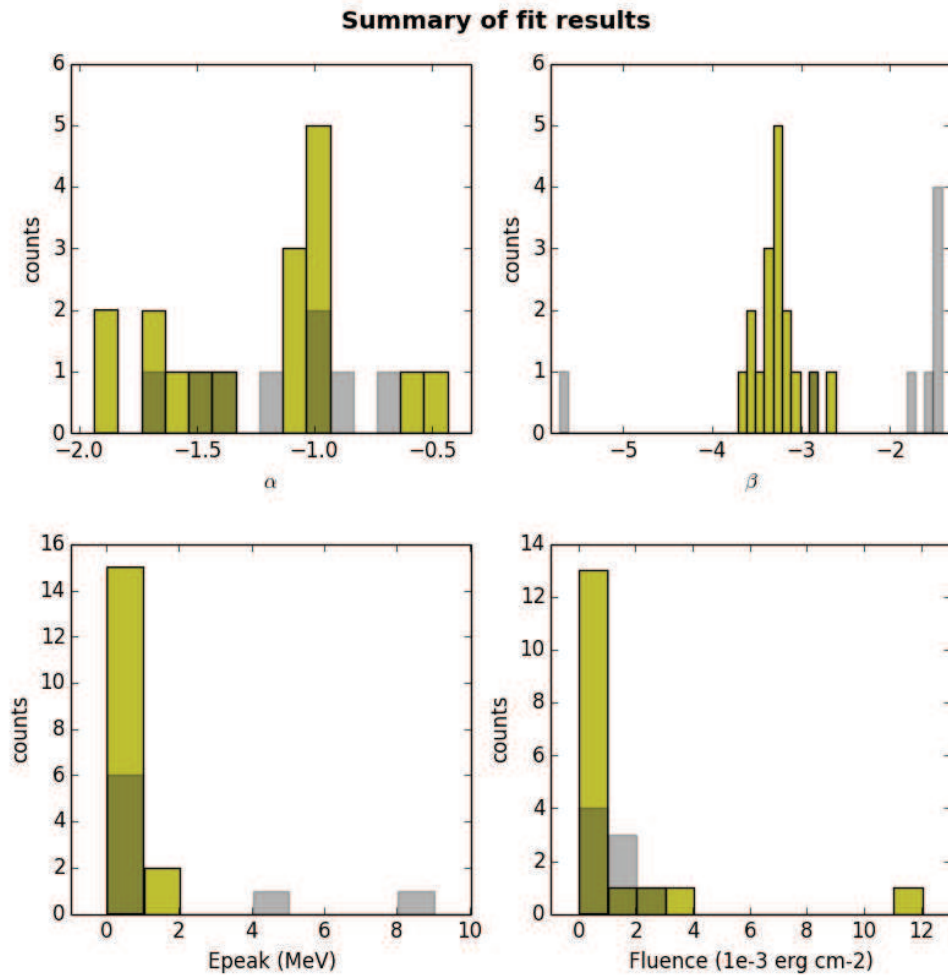


Figure 2.15: Summary of results obtained from the fit: the values obtained when a BB component is required are in grey while when it's not the parameters are shown in yellow.

better understand if this separation between the values of the high-energy spectral index is real or not. The mean value for the fluence is 1.3×10^{-3} erg cm².

Ten bursts show evidence of a cut-off at energies above 10 MeV; only in one case the cut-off energy is above 100 MeV but it is not constrained, i.e. the errors are too big. This is the case of the famous GRB 0900926A for which a cut-off at high energies has been reported by [21] and [17] while a photospheric component has been reported by [86]; these previous analyses have been done in different time intervals so a direct comparison with my results is difficult. Moreover, in the case

of this bright burst, the use of LAT standard data would help to assess the cut-off feature at high-energy while usually faint bursts benefit more by the use of LLE data. A spectral cut-off has been already reported in the spectrum of GRB 100724 by [17].

As already mentioned, the value of the Lorentz factor can be obtained assuming that the spectral cut-off is due to internal pair opacity.

By using a simplified expression of $\tau_{\gamma\gamma}$, as done in [13], and setting $\tau_{\gamma\gamma}(E_c)=1$, Abdo et al. 2009 [21] obtain the Lorentz factor as a function of the parameters obtained by the fit (E_0, E_c, β) , of the redshift and the variability time of the burst.

Tang et al. 2015 [171] pointed out that equation used in [21] is valid when the cutoff energy, E_c , is larger than a few hundreds MeV. However, for bursts with lower E_c , such all bursts in my sample, this condition is not satisfied; in this case the Lorentz factor is estimated to be [107]:

$$\Gamma \approx \frac{E_c}{m_e c^2} (1 + z) \quad (2.4)$$

Using this expression and high-energy cut-offs values ($E_c \geq \text{MeV}$) for GRBs in my sample I performed a first estimate of the Lorentz factor values. If available, I used known redshifts¹⁴, determined either spectroscopically or photometrically; for other bursts I tested two typical redshift values $z = 1$ and $z = 2$. The values found for the Lorentz factor are comprised from ~ 60 to ~ 860 .

These estimates are preliminary. When Pass8 data will be available for all GRBs, the whole analysis pipeline will be re-run and the simulations needed to distinguish between not nested models will be performed. In this way it will be possible to compute spectral parameters with more accuracy allowing to better measure also the values for the Lorentz factor.

Spectral analysis using GBM and LAT data have been already performed in [17], but in that case only with LAT standard event selection that can be used only for $E \gtrsim 100\text{MeV}$. LLE data have been used in some papers dedicated to specific bursts (e.g. [121, 86, 41]) providing evidence that these type of data are very useful to better study the low-energy part of GRBs spectrum and to test the existence of additional spectral features; this is true especially in the case of faint bursts.

A direct comparison with previous published results on the same bursts is beyond the scope of the work presented in this thesis but the method proposed here will be used for a forthcoming dedicated publication (in preparation) that will be the first systematic analysis of LLE-detected GRBs and will benefit from improvements of Pass8 event selection for the whole sample of bursts.

¹⁴<http://www.mpe.mpg.de/jcg/grbgen.html>

| Model | Parameter | Value |
|-----------------------------|----------------------|----------------------------------|
| bn080825593 | | |
| Band + Compt. | alpha | $-1.71^{+0.03}_{-0.04}$ |
| | beta | $-3.57^{+0.01}_{-0.02}$ |
| | E0 | $707.8^{+13.0}_{-7.6}$ |
| | Ph. index (pow.) | $1.39^{+0.01}_{-0.01}$ |
| | Cutoff energy | $122.5^{+3.8}_{-5.6}$ |
| | Fluence (10-1E7 keV) | $0.001281^{+6e-06}_{-6e-06}$ |
| | Statistic | 1.383e+04 (with 508 dof) |
| Band with cutoff+Black Body | alpha | $-1.63^{+0.03}_{-0.01}$ |
| | beta | $-1.827^{+0.006}_{-0.007}$ |
| | Cut-off energy | $7.678e+04^{+4783}_{-3870}$ |
| | kT | $751.2^{+2.4}_{-2.6}$ |
| | Fluence (10-1E7 keV) | $0.001168^{+5e-06}_{-6e-06}$ |
| | Statistic | 1.563e+04 (with 508 dof) |
| bn080916009 | | |
| Band + Compt. | alpha | $-1.03^{+0.01}_{-0.02}$ |
| | beta | $-3.41^{+0.01}_{-0.01}$ |
| | E0 | $830.9^{+10.1}_{-4.9}$ |
| | Ph. index (pow.) | $1.19^{+0.01}_{-0.01}$ |
| | Cutoff energy | $142.9^{+4.3}_{-5.8}$ |
| | Fluence (10-1E7 keV) | $0.002270^{+7e-06}_{-8e-06}$ |
| | Statistic | 1.603e+04 (with 394 dof) |
| Band + black body | alpha | $-1.572^{+0.003}_{-0.004}$ |
| | beta | $-3.18^{+0.03}_{-0.05}$ |
| | E0 | $2.522e+04^{+671.3}_{-518}$ |
| | kT | $692.3^{+1.5}_{-2.0}$ |
| | Fluence (10-1E7 keV) | $0.002290^{+6e-06}_{-6e-06}$ |
| | Statistic | 2.1e+04 (with 395 dof) |
| bn081024891 | | |
| Band + Compt. | alpha | $-0.97^{+0.12}_{-0.11}$ |
| | beta | $-3.17^{+0.04}_{-0.04}$ |
| | E0 | $851.5^{+56.3}_{-53.5}$ |
| | Ph. index (pow.) | $1.091^{+0.08}_{-0.08}$ |
| | Cutoff energy | $48.9^{+5.5}_{-4.6}$ |
| | Fluence (10-1E7 keV) | $6.46e-05^{+1.4e-06}_{-1.3e-06}$ |
| | Statistic | 1601 (with 513 dof) |

Table 2.2: Best fit parameters for the best models for LLE-detected time interval. Note that energy (E0, Cutoff energy) and temperature (kT) are given in keV; fluences are given in erg cm^{-2} .

| Model | Parameter | Value |
|-------------------|----------------------|-----------------------------------|
| bn081224887 | | |
| Band + Compt. | alpha | $-0.47^{+0.13}_{-0.11}$ |
| | beta | $-3.44^{+0.08}_{-0.08}$ |
| | E0 | $1054.0^{+85.7}_{-81.2}$ |
| | Ph. index (pow.) | $1.206^{+0.13}_{-0.14}$ |
| | Cutoff energy | $73.0^{+27.2}_{-16.0}$ |
| | Fluence (10-1E7 keV) | $3.70e-05^{+1.1e-06}_{-1.0e-06}$ |
| | Statistic | 973.2 (with 514 dof) |
| bn090217206 | | |
| Band + Compt. | alpha | $-1.90^{+0.13}_{-0.16}$ |
| | beta | $-3.55^{+0.11}_{-0.16}$ |
| | E0 | $550.3^{+31.3}_{-22.5}$ |
| | Ph. index (pow.) | $1.531^{+0.008}_{-0.007}$ |
| | Cutoff energy | $1.756e+04^{+790}_{-709}$ |
| | Fluence (10-1E7 keV) | $0.0002248^{+2.6e-06}_{-2.6e-06}$ |
| | Statistic | 2870 (with 514 dof) |
| Band + black body | alpha | $-1.530^{+0.005}_{-0.005}$ |
| | beta | $-4.50^{+0.16}_{-0.14}$ |
| | E0 | $1.941e+04^{+80}_{-421}$ |
| | kT | $589.9^{+6.6}_{-6.9}$ |
| | Fluence (10-1E7 keV) | $0.0002115^{+1.9e-06}_{-2.0e-06}$ |
| | Statistic | 2926 (with 515 dof) |
| bn090227772 | | |
| Band + Compt. | alpha | $-1.13^{+0.12}_{-0.11}$ |
| | beta | $-3.62^{+0.21}_{-0.32}$ |
| | E0 | $692.7^{+37.6}_{-36.3}$ |
| | Ph. index (pow.) | $1.50^{+0.02}_{-0.02}$ |
| | Cutoff energy | $4.103e+04^{+4823}_{-4413}$ |
| | Fluence (10-1E7 keV) | $0.0001249^{+2.4e-06}_{-2.4e-06}$ |
| | Statistic | 1262 (with 510 dof) |
| Band + black body | alpha | $-1.44^{+0.01}_{-0.01}$ |
| | beta | $-3.91^{+0.43}_{-0.96}$ |
| | E0 | $3.26e+04^{+2789}_{-2549}$ |
| | kT | $557.7^{+8.1}_{-8.1}$ |
| | Fluence (10-1E7 keV) | $0.0001227^{+2.2e-06}_{-2.3e-06}$ |
| | Statistic | 1288 (with 511 dof) |

Table 2.3: Best fit parameters for the best models for LLE-detected time interval. Note that energy (E0, Cutoff energy) and temperature (kT) are given in keV; fluences are given in erg cm^{-2} .

| Model | Parameter | Value |
|-----------------------------|----------------------|-----------------------------------|
| bn090323002 | | |
| Band + Compt. | alpha | $-1.05^{+0.01}_{-0.02}$ |
| | beta | $-3.309^{+0.009}_{-0.008}$ |
| | E0 | $816.3^{+8.7}_{-5.8}$ |
| | Ph. index (pow.) | $1.42^{+0.01}_{-0.01}$ |
| | Cutoff energy | $115.7^{+2.7}_{-3.9}$ |
| | Fluence (10-1E7 keV) | $0.003195^{+1.0e-05}_{-1.0e-05}$ |
| | Statistic | 4.415e+04 (with 511 dof) |
| bn090328401 | | |
| Band with cutoff+Black Body | -alpha | $-0.69^{+0.5}_{-0.08}$ |
| | beta | $-1.509^{+0.003}_{-0.006}$ |
| | Cut-off energy | $2.859e+04^{+979}_{-647}$ |
| | kT | $643.9^{+5.3}_{-5.8}$ |
| | Fluence (10-1E7 keV) | $0.0005201^{+3.8e-06}_{-4.1e-06}$ |
| | Statistic | 5345 (with 513 dof) |
| bn090510016 | | |
| Band + Compt. | alpha | $-1.57^{+0.03}_{-0.04}$ |
| | beta | $-3.161^{+0.01}_{-0.02}$ |
| | E0 | $678.1^{+13.6}_{-9.7}$ |
| | Ph. index (pow.) | $1.378^{+0.02}_{-0.02}$ |
| | Cutoff energy | $63.6^{+2.6}_{-2.4}$ |
| | Fluence (10-1E7 keV) | $0.0006782^{+3.9e-06}_{-4.1e-06}$ |
| | Statistic | 1.115e+04 (with 514 dof) |

Table 2.4: Best fit parameters for the best models for LLE-detected time interval. Note that energy (E0, Cutoff energy) and temperature (kT) are given in keV; fluences are given in erg cm^{-2} .

| Model | Parameter | Value |
|-----------------------------|----------------------|---------------------------------------|
| bn090902462 | | |
| Band + black body | alpha | $-1.459^{+0.002}_{-0.002}$ |
| | beta | $-2.88^{+0.03}_{-0.03}$ |
| | E0 | 8116^{+252}_{-225} |
| | kT | $563.5^{+2.7}_{-2.7}$ |
| | Fluence (10-1E7 keV) | $0.001502^{+5e-06}_{-6e-06}$ |
| | Statistic | 6925 (with 512 dof) |
| Band + Compt. | alpha | $-0.02^{+0.02}_{-0.04}$ |
| | beta | $-3.04^{+0.01}_{-0.01}$ |
| | E0 | 1151^{+29}_{-13} |
| | Ph. index (pow.) | $1.466^{+0.006}_{-0.006}$ |
| | Cutoff energy | 468^{+33}_{-43} |
| | Fluence (10-1E7 keV) | $0.001426^{+5e-06}_{-6e-06}$ |
| | Statistic | 7887 (with 511 dof) |
| bn090926181 | | |
| Band + Compt. | alpha | $-1.35^{+0.16}_{-0.09}$ |
| | beta | $-2.879^{+0.01}_{-0.01}$ |
| | E0 | $731.1^{+27.4}_{-38.0}$ |
| | Ph. index (pow.) | $1.017^{+0.007}_{-0.006}$ |
| | Cutoff energy | $346.7^{+14.0}_{-9.5}$ |
| | Fluence (10-1E7 keV) | $0.0008734^{+4.3e-06}_{-5.0e-06}$ |
| | Statistic | 4325 (with 513 dof) |
| Band with cutoff+Black Body | alpha | $-1.006^{+0.007}_{-0.006}$ |
| | beta | $-2.01^{+0.01}_{-0.01}$ |
| | Cut-off energy | $1.413e+05^{+1.315e+04}_{-1.228e+04}$ |
| | kT | $702.9^{+4.0}_{-4.7}$ |
| | Fluence (10-1E7 keV) | $0.0008366^{+3.9e-06}_{-3.9e-06}$ |
| | Statistic | 4541 (with 513 dof) |
| bn091031500 | | |
| Band + power law | alpha | $-1.00^{+0.01}_{-0.02}$ |
| | beta | $-3.37^{+0.02}_{-0.01}$ |
| | E0 | $839.5^{+9.6}_{-9.1}$ |
| | Ph. index (pow.) | $1.904^{+0.007}_{-0.003}$ |
| | Fluence (10-1E7 keV) | $0.0006798^{+3.3e-06}_{-3.0e-06}$ |
| | Statistic | 8852 (with 397 dof) |

Table 2.5: Best fit parameters for the best models for LLE-detected time interval. Note that energy (E0, Cutoff energy) and temperature (kT) are given in keV; fluences are given in erg cm^{-2} .

| Model | Parameter | Value |
|-----------------------------|----------------------|-------------------------------|
| bn100116897 | | |
| Band + black body | alpha | $-1.642^{+0.004}_{-0.004}$ |
| | beta | $-5.71^{+0.80}_{-0.25}$ |
| | E0 | $2.441e+04^{+595}_{-588}$ |
| | kT | 605^{+3}_{-3} |
| | Fluence (10-1E7 keV) | $0.000522^{+3e-06}_{-3e-06}$ |
| | Statistic | 6436 (with 511 dof) |
| bn100225115 | | |
| Band + Compt. | alpha | $-1.52^{+0.09}_{-0.10}$ |
| | beta | $-3.04^{+0.02}_{-0.02}$ |
| | E0 | $634.4^{+27.1}_{-21.6}$ |
| | Ph. index (pow.) | $1.55^{+0.04}_{-0.04}$ |
| | Cutoff energy | $161.8^{+26.4}_{-23.2}$ |
| | Fluence (10-1E7 keV) | $0.000273^{+3e-06}_{-3e-06}$ |
| | Statistic | 4634 (with 511 dof) |
| bn100724029 | | |
| Band with cutoff+Black Body | alpha | $-1.034^{+0.01}_{-0.01}$ |
| | beta | $-1.428^{+0.003}_{-0.004}$ |
| | Cut-off energy | $1.473e+04^{+188}_{-144}$ |
| | kT | $577.6^{+2.1}_{-2.5}$ |
| | Fluence (10-1E7 keV) | $0.002544^{+8e-06}_{-9.e-06}$ |
| | Statistic | 1.713e+04 (with 510 dof) |
| bn100826957 | | |
| Band with cutoff+Black Body | alpha | $-1.34^{+0.02}_{-0.02}$ |
| | beta | $-1.530^{+0.004}_{-0.007}$ |
| | Cut-off energy | $2.168e+04^{+627}_{-454}$ |
| | kT | $635.7^{+2.3}_{-2.5}$ |
| | Fluence (10-1E7 keV) | $0.001714^{+7e-06}_{-8e-06}$ |
| | Statistic | 7504 (with 394 dof) |

Table 2.6: Best fit parameters for the best models for LLE-detected time interval. Note that energy (E0, Cutoff energy) and temperature (kT) values are given in keV; fluences are given in erg cm^{-2} .

| Model | Parameter | Value |
|-----------------------------|----------------------|-----------------------------------|
| bn101123952 | | |
| Band + black body | alpha | $-1.02^{+0.01}_{-0.01}$ |
| | beta | $-1.79^{+0.01}_{-0.01}$ |
| | E0 | $592.3^{+52.0}_{-42.1}$ |
| | kT | $610.3^{+6.4}_{-5.7}$ |
| | Fluence (10-1E7 keV) | $0.00147^{+7e-05}_{-7e-05}$ |
| | Statistic | 1595 (with 394 dof) |
| bn110328520 | | |
| Band + Compt. | alpha | $-1.04^{+0.03}_{-0.04}$ |
| | beta | $-3.25^{+0.02}_{-0.01}$ |
| | E0 | $796.5^{+18.2}_{-14.3}$ |
| | Ph. index (pow.) | $0.19^{+0.03}_{-0.04}$ |
| | Cutoff energy | $29.8^{+0.7}_{-0.8}$ |
| | Fluence (10-1E7 keV) | $0.0005894^{+4.3e-06}_{-4.2e-06}$ |
| | Statistic | $3.245e+04$ (with 512 dof) |
| Band + black body | alpha | $-0.50^{+0.03}_{-0.03}$ |
| | beta | $-3.28^{+0.02}_{-0.01}$ |
| | E0 | 1038^{+18}_{-19} |
| | kT | $11.56^{+0.06}_{-0.05}$ |
| | Fluence (10-1E7 keV) | $0.0005803^{+4.2e-06}_{-4.0e-06}$ |
| | Statistic | $3.395e+04$ (with 513 dof) |
| bn110529034 | | |
| Band + Compt. | alpha | $-0.57^{+0.51}_{-0.32}$ |
| | beta | $-3.26^{+0.07}_{-0.07}$ |
| | E0 | 1020^{+200}_{-190} |
| | Ph. index (pow.) | $1.34^{+0.11}_{-0.15}$ |
| | Cutoff energy | $241.2^{+635.1}_{-122.3}$ |
| | Fluence (10-1E7 keV) | $3.5e-05^{+1e-06}_{-1e-06}$ |
| | Statistic | 1038 (with 514 dof) |
| bn110721200 | | |
| Band with cutoff+Black Body | alpha | $-0.87^{+0.08}_{-0.08}$ |
| | beta | $-1.456^{+0.008}_{-0.009}$ |
| | Cut-off energy | $1.649e+04^{+530}_{-478}$ |
| | kT | $601.2^{+7.1}_{-7.3}$ |
| | Fluence (10-1E7 keV) | $0.0002855^{+2.7e-06}_{-2.8e-06}$ |
| | Statistic | 2186 (with 514 dof) |

Table 2.7: Best fit parameters for the best models for LLE-detected time interval. Note that energy (E0, Cutoff energy) and temperature (kT) values are given in keV; fluences are given in erg cm^{-2} .

| Model | Parameter | Value |
|-----------------------------|----------------------|-----------------------------------|
| bn110731465 | | |
| Band + Compt. | alpha | $-1.66^{+0.05}_{-0.06}$ |
| | beta | $-3.392^{+0.02}_{-0.02}$ |
| | E0 | $658.4^{+16.9}_{-13.6}$ |
| | Ph. index (pow.) | $1.90^{+0.006}_{-0.007}$ |
| | Cutoff energy | $2.092e+04^{+2221}_{-2089}$ |
| | Fluence (10-1E7 keV) | $0.0006501^{+4.3e-06}_{-4.3e-06}$ |
| | Statistic | 6039 (with 394 dof) |
| Band + black body | alpha | $-1.821^{+0.005}_{-0.006}$ |
| | beta | $-3.40^{+0.09}_{-0.12}$ |
| | E0 | $4.788e+04^{+1928}_{-2045}$ |
| | kT | $674.8^{+3.42}_{-3.8}$ |
| | Fluence (10-1E7 keV) | $0.0005943^{+2.8e-06}_{-3.3e-06}$ |
| | Statistic | 7248 (with 395 dof) |
| bn120226871 | | |
| Band + Compt. | alpha | $-0.95^{+0.04}_{-0.04}$ |
| | beta | $-3.30^{+0.02}_{-0.01}$ |
| | E0 | 850^{+19}_{-17} |
| | Ph. index (pow.) | $1.24^{+0.012}_{-0.02}$ |
| | Cutoff energy | 115^{+5}_{-5} |
| | Fluence (10-1E7 keV) | $0.0006924^{+4.5e-06}_{-4.5e-06}$ |
| | Statistic | $1.529e+04$ (with 510 dof) |
| bn120328268 | | |
| Band with cutoff+Black Body | alpha | $-1.15^{+0.02}_{-0.02}$ |
| | beta | $-1.50^{+0.01}_{-0.01}$ |
| | Cut-off energy | $1.696e+04^{+817}_{-704}$ |
| | kT | $634.2^{+4.177}_{-4.039}$ |
| | Fluence (10-1E7 keV) | $0.0005569^{+4.2e-06}_{-4.1e-06}$ |
| | Statistic | 7294 (with 511 dof) |
| bn120624933 | | |
| Band + Compt. | alpha | $-0.978^{+0.001}_{-0.001}$ |
| | beta | $-2.7^{+0.004}_{-0.003}$ |
| | E0 | $817.6^{+0.8}_{-0.7}$ |
| | Ph. index (pow.) | $1.469^{+0.003}_{-0.001}$ |
| | Cutoff energy | $94.04^{+0.66}_{-0.32}$ |
| | Fluence (10-1E7 keV) | $0.01138^{+1e-05}_{-1e-05}$ |
| | Statistic | $1.388e+05$ (with 509 dof) |

Table 2.8: Best fit parameters for the best models for LLE-detected time interval. Note that energy (E0, Cutoff energy) and temperature (kT) are given in keV; fluences are given in erg cm^{-2} .

| Model | Parameter | Value |
|---------------|----------------------|----------------------------------|
| bn120709883 | | |
| Band + Compt. | alpha | $-1.94^{+0.14}_{-0.21}$ |
| | beta | $-3.22^{+0.05}_{-0.05}$ |
| | E0 | $578.3^{+44.6}_{-30.5}$ |
| | Ph. index (pow.) | $1.79^{+0.01}_{-0.01}$ |
| | Cutoff energy | $2.328e+04^{+3465}_{-3495}$ |
| | Fluence (10-1E7 keV) | $9.72e-05^{+1.7e-06}_{-1.7e-06}$ |
| | Statistic | 2017 (with 514 dof) |

Table 2.9: Best fit parameters for the best models for LLE-detected time interval. Note that energy (E0, Cutoff energy) and temperature (kT) are given in keV; fluences are given in erg cm^{-2} .

Chapter 3

Solar Flares

A solar flare is an intense and rapid energy release in the solar corona driven by stored magnetic energy liberated by coronal magnetic reconnection processes. The energy release results in acceleration of particles, including electrons, protons and heavy nuclei, to a wide range of energies and in heating of coronal and chromospheric plasma. This definition is strictly related to what is called the "standard flare model" (see Fig.3.1) and has been postulated starting from the empirical observation of a causal relation between the thermal soft X-ray flux and non-thermal hard X-ray signatures of energetic electrons (Neupert effect).

First observation was reported by Carrington in 1859 ([52]) in optical band and in association with sunspots. After that, thanks to the improvements of observational techniques, solar flares were observed at various wavelengths across the electromagnetic spectrum: radio, EUV and X-ray observations were performed during the first half of the 20th century ([62, 91, 75]) while first detection of gamma-ray line emission from heavy nuclei came later ([143, 57]).

3.1 The general picture

Nowadays, solar flares are usually classified in five main classes according to the 1-8 Å peak energy flux observed by the Geostationary Operational Environmental Satellites (GOES) (see Fig.3.2; note also that within a class there is a linear scale from 1 to 9.n).

Solar flares release energy in four different temporal phases ([96, 148]): Fig.3.3 shows the evolution of emission in different wavelengths. Concentrating our attention on the X and gamma-ray light curves we can distinguish:

- precursor phase, observed as a gradual raise of emission mainly visible in soft X-rays and EUV indicating the slowly heating of the coronal plasma in the flare region;

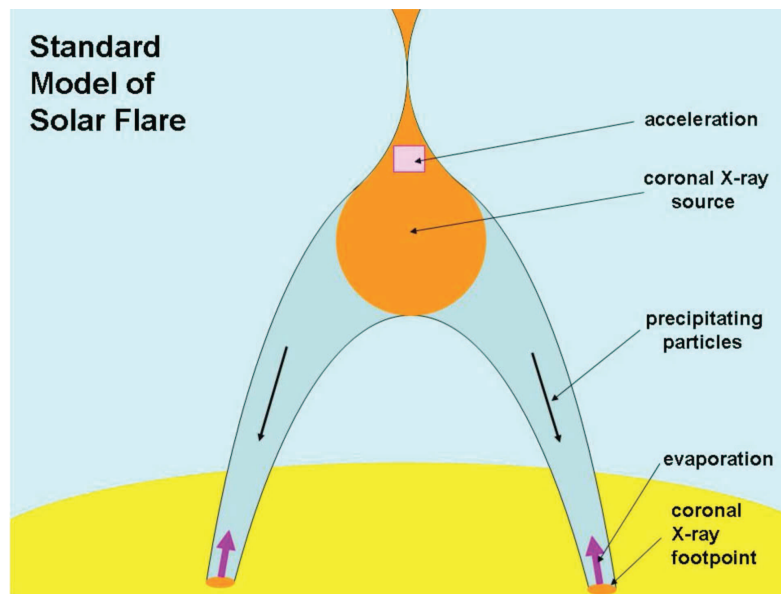


Figure 3.1: A schematic cartoon of the the "standard flare model". It postulates that the flare energy release consists of accelerating particles: energetic particles then precipitate to the chromosphere, where they heat the plasma to the high temperatures observed in soft X-rays. The hot plasma expands along the loop into the corona: this process is called "evaporation" [45].

| GOES class | $1 - 8 \text{ \AA}$ peak [W/m ²] | events/year max/min |
|------------|---|------------------------|
| A | $> 10^{-8}$ | -- |
| B | $> 10^{-7}$ | -- |
| C | $> 10^{-6}$ | $> 2000/300$ |
| M | $> 10^{-5}$ | 300/20 |
| X | $> 10^{-4}$ | 10/1 |
| -- | $> 10^{-3}$ | few?/none? |

Figure 3.2: Solar flare GOES classification [178].

- impulsive, characterized by a rapid raise of hard X and gamma-ray flux; this is the phase when most of the flare energy is released. A large number of energetic electrons and ions is accelerated while some trapped high-energy

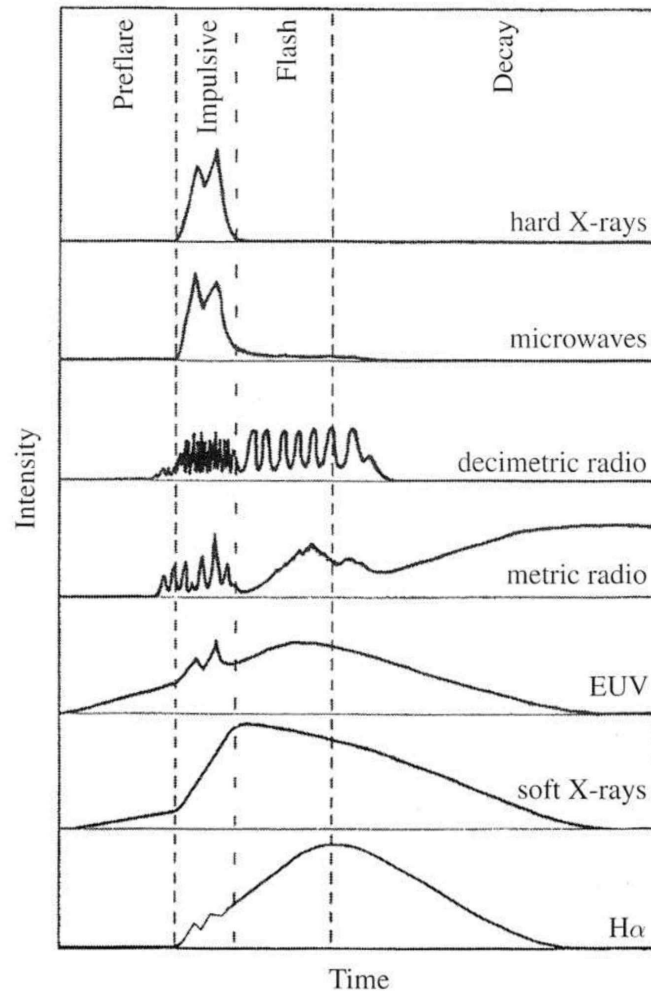


Figure 3.3: Solar flare emission in different energy ranges [45].

particles produce emissions in the radio band.

- gradual, observed as a slow decaying of X and gamma-ray flux; in this phase the thermal soft X-ray and $H\alpha$ emissions¹ reach their maxima and energy is more gently released. The coronal plasma returns nearly to its pre-flare state, except in the high corona where magnetic reconfiguration, plasma ejections and shock waves continue to accelerate particles, causing metric-radio² bursts

¹Solar flares are often observed using filters to isolate the light emitted by hydrogen atoms in the red region of the solar spectrum i.e. the $H\alpha$ spectral line.

² $\lesssim 300$ MHz

and release of Solar Energetic Particles (SEP).

- extended, mainly observed as a sustained gamma-ray emission that can last for several hours.

Coronal Mass Ejections (CMEs) and Solar Energetic Particles (SEP) are often observed in association with most energetic solar flares [96].

| Emissions | Processes | Observed photons or neutrons | Primary ion or electron energy range |
|---------------------------------|---|--|--|
| Continuum | Primary electron bremsstrahlung | 20 keV–1 MeV >10 MeV | 20 keV–1 GeV |
| Nuclear de-excitation lines | Accelerated ion interactions, e.g., ${}^4\text{He}(\alpha, n){}^7\text{Be}^*$ ${}^4\text{He}(\alpha, p){}^7\text{Li}^*$ ${}^{20}\text{Ne}(p, p'){}^{20}\text{Ne}^*$ ${}^{12}\text{C}(p, p'){}^{12}\text{C}^*$ ${}^{16}\text{O}(p, p'){}^{16}\text{O}^*$ | Lines at e.g., 0.429 MeV 0.478 MeV 1.634 MeV 4.439 MeV 6.129 MeV | 1–100 MeV/nucl |
| Neutron capture line | Neutron production by accelerated ions followed by ${}^1\text{H}(n, \gamma){}^2\text{H}$ | Line at 2.223 MeV | 10–100 MeV/nucl |
| Positron annihilation radiation | β^+ Emitter or π^+ production by accelerated ions, e.g., ${}^{12}\text{C}(p, pn){}^{11}\text{C} \mapsto {}^{11}\text{B} + e^+ + \nu$ $p + p \mapsto \pi^+ \dots \pi^+ + \mapsto \mu^+ \mapsto e^+$ followed by $e^+ + e^- \mapsto 2\gamma$ $e^+ + e^- \mapsto \text{Ps} + h\nu$ or $e^+ + {}^1\text{H} \mapsto \text{Ps} + p$ $\text{Ps} \mapsto 2\gamma, 3\gamma$ | Line at 0.511 MeV Orthopositronium Continuum < 511 keV | 10–100 MeV/nucl |
| Pion decay radiation | π^0 and π^\pm production by accelerated particles, e.g., $p + p \mapsto \pi^0, \pi^\pm \dots$ followed by $\pi^0 \mapsto 2\gamma, \pi^\pm \mapsto \mu^\pm \mapsto e^\pm$ $e^\pm \mapsto \gamma_{\text{brems}}, \gamma_{\text{ann}}$ in flight $e^- \mapsto \gamma_{\text{brems}}$ | 10 MeV–3 GeV | 0.2–5 GeV |
| Neutrons | Accelerated particle interactions, e.g., ${}^4\text{He}(p, pn){}^3\text{He}$ $p + p \mapsto \pi + n + \dots$ ${}^{22}\text{Ne}(\alpha, n){}^{25}\text{Mg}$ | neutrons in space (10–500 MeV) neutron induced atmospheric cascades (0.1–10 GeV) Neutron decay protons in space (20–200 MeV) | 10 MeV–1 GeV 0.1–10 GeV 20–400 MeV |

Figure 3.4: High-energy photon and nuclear production mechanisms [149].

During the impulsive phase, various physical components can be observed in the energy range covered by the GBM and LAT (see also Fig. 3.4 for details [149]):

- bremsstrahlung radiation produced from electrons with energies up to a few MeV in high-density regions of the solar corona and chromosphere;
- gamma-ray line emission from nuclear interactions of accelerated protons or heavier ions with the solar medium: nuclear de-excitation lines, neutron-capture line at 2.23 MeV due to accelerated neutrons captured by the protons to form the heavier deuterium and electron-positron annihilation line at 511 keV;
- continuum radiation produced by interactions of > 300 MeV protons and > 800 MeV α particles with solar ambient ions producing neutral and charged pions [122]: the first decay in gamma rays producing the characteristic pion bump spectral shape, while the latter decay ultimately into energetic electrons, positrons, and neutrinos.

One of the main goal of this chapter is to characterize the spectral components emerging in the impulsive phase of solar flares using both GBM and LAT data (see Sec. 3.4 for details).

3.2 Observations at high-energies

The first systematic observational campaign of solar flares up to tens of MeV has been performed using instruments onboard the Solar Maximum Mission (SMM) [176] that sampled mainly the impulsive phase of the eruptive events (see Fig.3.5). EGRET detected gamma-rays above 100 MeV for more than an hour after the impulsive phases for three flares. In particular, the 1991 June 11 flare (GOES class X12.0) is remarkable because the high-energy emission lasted for 8 hr after the impulsive phase [100] (see Fig.3.6). It was suggested that the particles accelerated during the impulsive phase of the flare could remain trapped for the entire duration of the flare and precipitate gradually into the denser solar atmosphere to produce the gamma-rays [157]; alternatively, the possible origin could be continuous acceleration either by CME shock or by turbulence in a closed magnetic loop [151]. The origin of the temporally extended emission is not well understood yet and an important open question is whether the radiative process is hadronic or leptonic.

3.2.1 Solar Flares as observed by the LAT

As already mentioned, the GBM and the LAT, the two instruments on-board to the *Fermi* spacecraft, can detect photons with energies from 8 keV up to 1 TeV. Both instruments also have very large fields of view (FOV) achieving together an unprecedented coverage of the X and gamma-ray sky: the GBM FOV consists

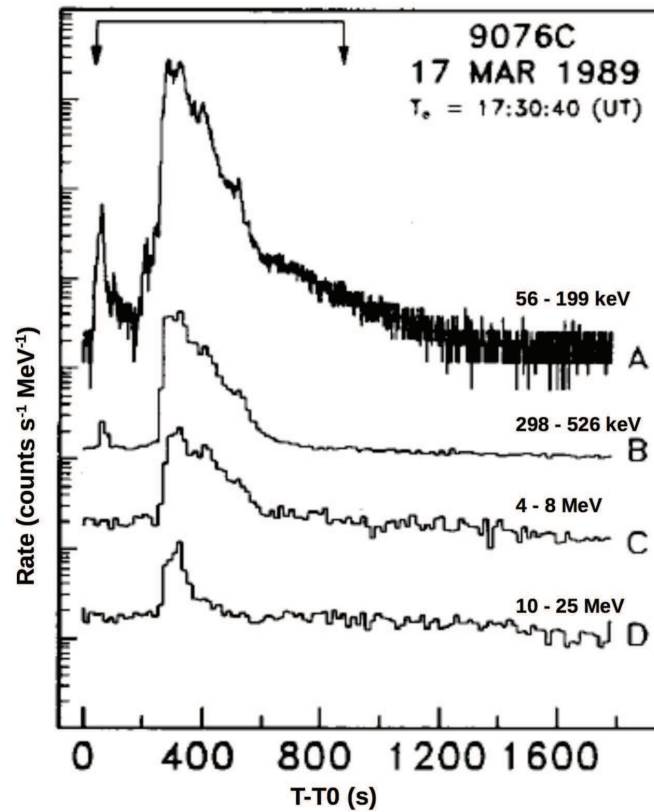


Figure 3.5: Light curve of a solar flare observed by SMM in different energy ranges (figure adapted from [176]).

of the whole not-occulted sky and the LAT scans about the 20% of the sky at any instant. These characteristics make *Fermi* a perfect observatory to study and monitor both the quiescent phase [8] and the eruptive phases of solar activity at high energies. Since the launch in June 2008, the LAT observed more than 40 solar flares above 30 MeV; this is particularly remarkable if compared with previous observations (Fig.3.7). A first collection of flares observed until May 2012 has been presented in [16]. It shows that high-energy emission is observed also in coincidence with moderate class flares and is more common than previously thought. Moreover it shows the capacity of the LAT to sample all the phases of solar flare emission; finally, all flares detected by the LAT are associated with fairly fast CME. In Fig.3.8 I show a summary of solar flares detected by the LAT and GBM up to October 2015: note again that gamma-ray emission is not only associated to extreme (X) class flares but also to M and C class flares [109]. Since then, only one solar flare has been detected by the LAT reflecting the fact that we are now approaching the

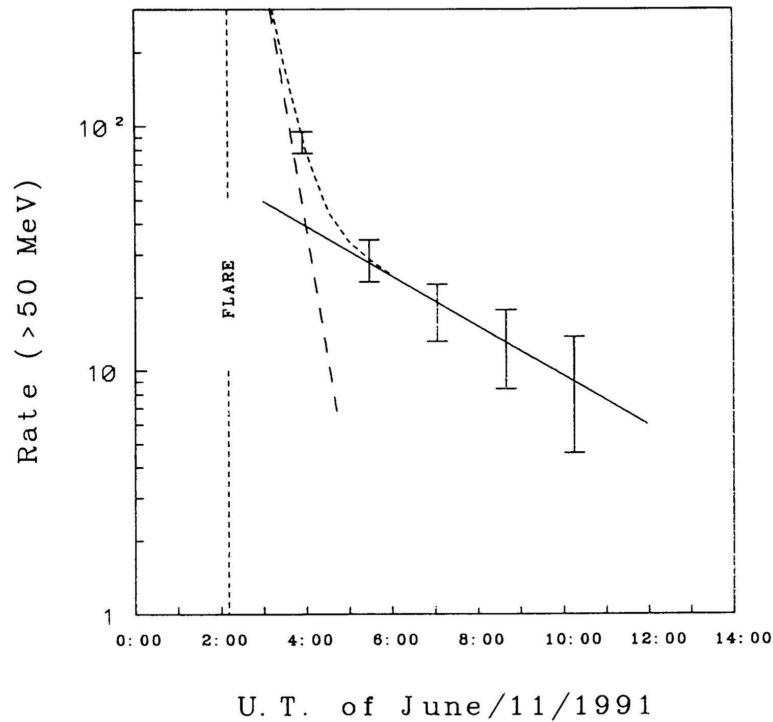


Figure 3.6: Time profile of the >50 MeV solar emission for the 1991 June 11 flare [100].

minimum of the solar cycle. On 2016 July 23, four flares triggered the GBM from 2 to 6 AM:

- trigger 160723.086 (at 02:04:29.56 UT), GOES class M5.0
- trigger 160723.153 (at 03:40:07.08 UT), GOES class C1.4
- trigger 160723.213 (at 05:07:23.19 UT), GOES class M7.6
- trigger 160723.227 (at 05:27:11.72 UT), GOES class M5.5

Despite the fact that all these flares occurred when the Sun was in the LAT FoV, I found that only the last one shows a LAT significant detection. As you can see, this flare is not the brightest in the sample (while the M7.6 flare is actually the strongest solar flare of 2016 up to now) but interestingly it is the only one that is reported to have an associated CME. A detailed study of correlation between gamma-ray detected flares and fast CME will be addressed in the catalog of solar flares detected by the LAT that is currently in preparation.

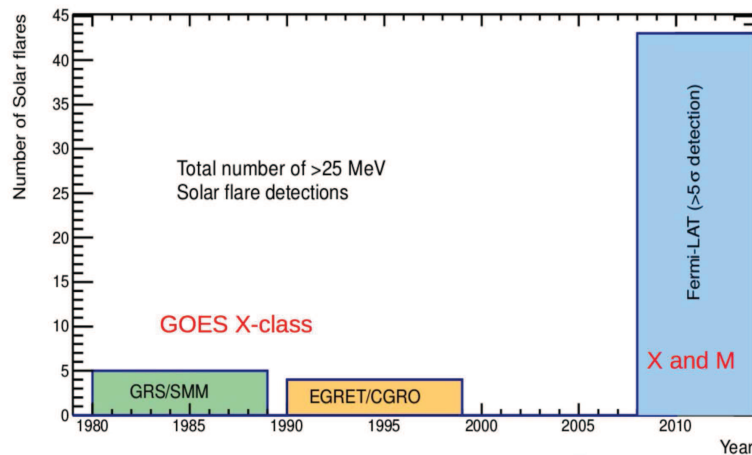


Figure 3.7: Summary of solar flares detected > 25 MeV from different instrumental facilities; adapted from [139].

The first impulsive solar flare detected by *Fermi* occurred on 2010 June 12 00:30 UT: the LAT and the GBM observed X and gamma-ray emission, from few keV up to ~ 400 MeV, in coincidence with a moderate GOES M2.0 class solar flare. For energies < 10 MeV the observed spectrum has been interpreted as a superposition of electron bremsstrahlung, nuclear lines and pion decay components. Above 30 MeV, high-energy electron bremsstrahlung or pion decay component are statistically equivalent in the fit given the large uncertainties; though theoretical speculation favor the hadronic model. The analysis of LAT data was performed using only the LAT LLE technique because the intense soft X-ray flux occurring during the prompt phase of the flare caused pile-up in the anti-coincidence detector of the LAT [15] resulting in a strong suppression of the rate of standard LAT Pass 6 / Pass7 on-ground photon classification (Fig.3.10).

I will show in next section (Sec. 3.3) that these issues have been carefully addressed in new Pass8 photon classification. LLE event selection, that does not suffer of ACD pile-up, uses less discriminating criteria then the standard on-ground processing, resulting in a larger effective area in particular at low-energies (< 100 MeV) and high inclination angles but a lower signal-to-noise ratio: LLE data are hence background dominated and not suitable for localization studies.

On 2012 March 7 two bright X-class flares originating from the active region NOAA AR 11429 ³ erupted within an hour of each other: the first flare (X5.4)

³Bright spots and illuminated arcs of solar material hovering in the sun's atmosphere are known as active regions; the National Oceanic and Atmospheric Administration (NOAA) numbers active

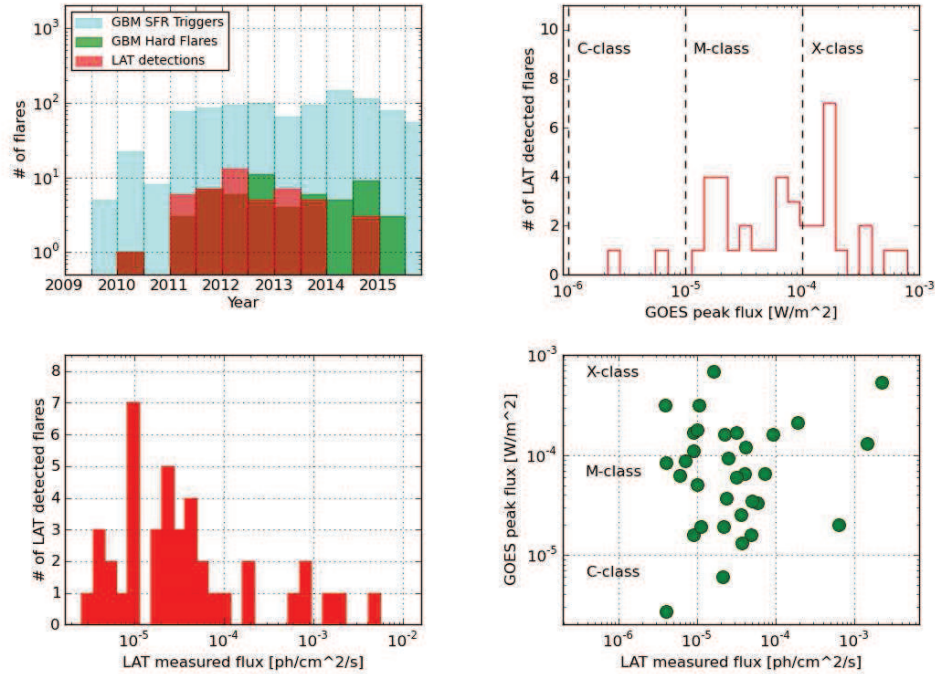


Figure 3.8: Summary of LAT and GBM detections up to October 2015 [109].

started at 00:02:00 UT while the second X1.3 class flare occurred at 01:05:00 UT. Orbital sunrise of Fermi occurred about six minutes after the peak of the first flare, detecting gamma-ray emission up to 4 GeV; the > 100 MeV count rate showed that the sun was about 100 times brighter than the Vela Pulsar and more than 1000 times brighter than the steady sun. Surprisingly the sustained emission above 100 MeV lasted for about 20 hours setting a new record. Looking at the temporal evolution, a softening of the spectrum with time was observed. Impulsive emission was found to correlate with the X-ray flux while sustained emission was better correlated with the evolution of the SEP. Thanks to the high statistics, it was also possible to perform time-integrated and time-resolved localization studies finding that the gamma-ray emission was consistent with the active region from which the flare originated (Fig.3.11). To achieve the required accuracy, the correction of the so-called fish-eye effect has been performed: it is a deviation introduced by the detector to photons arriving from high-inclination angles and it is particularly relevant at low energies (< 300 MeV) where most of solar flare emission is concentrated.

regions consecutively as they are observed on the sun.

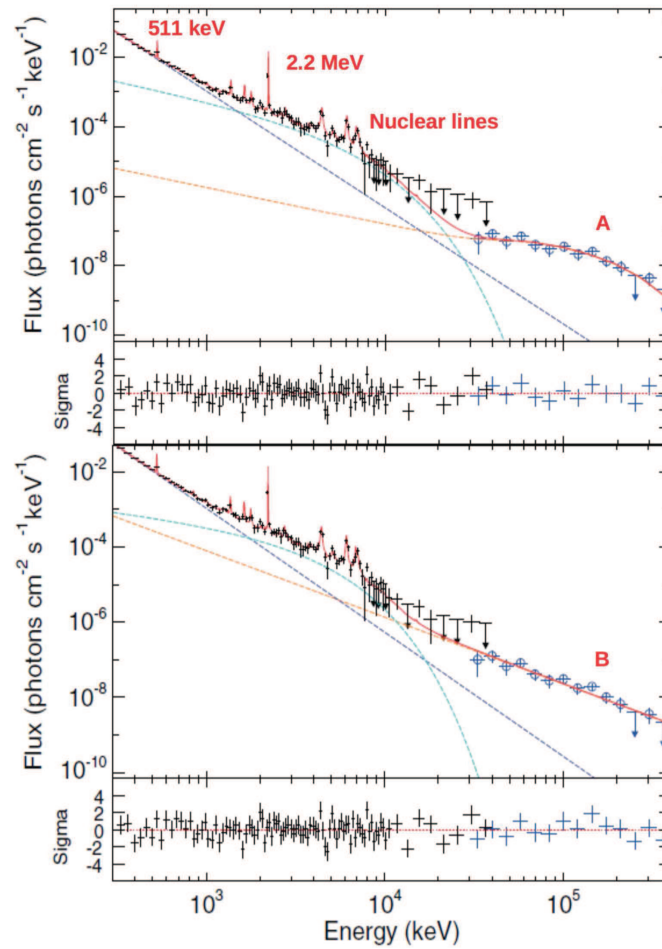


Figure 3.9: Combined GBM/LAT photon spectrum accumulated during the impulsive phase. The upper panel shows a pion-decay fit to the LAT spectrum; alternatively the lower panel shows a power-law fit, representing a third electron bremsstrahlung component. Figure and caption adapted from [15].

Lately, the LAT observed for the first time > 100 MeV emission from three solar flares originated behind the visible part of the sun ([141, 140]). The detection of such footpoint-occulted flares requires a careful analysis of different emission scenarios (Fig.3.12): since high values of optical depths rule out the gamma rays originating from the flare site (a) and a high-corona trap model requires very unusual conditions (b), a scenario in which some of the particles accelerated by the CME shock travel to the visible side of the Sun (c) producing the observed gamma rays may be at work.

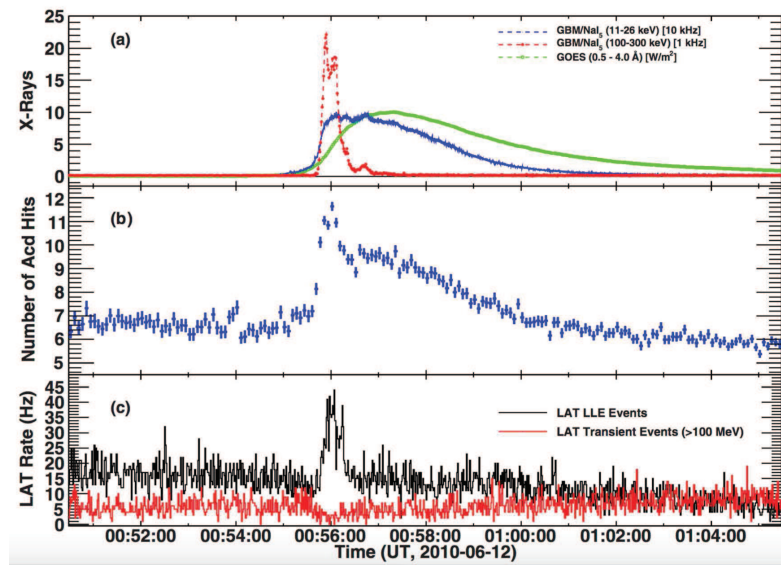


Figure 3.10: Time histories for the 2010 June 12 solar flare. (a) GOES 0.5-4 Å rates, and GBM NaI 11-26 keV and 100-300 keV relative rates; (b) LAT ACD hit rate >100 keV; (c) LLE and LAT Transient Class event rates. Figure and caption taken from [15].

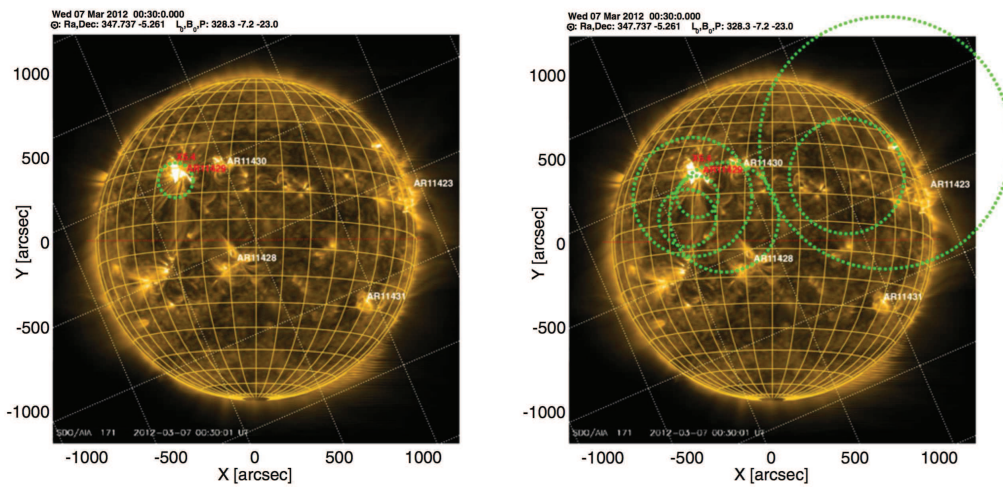


Figure 3.11: Location of the gamma-ray emission above 100 MeV for the time-integrated (left) and the time resolved (right) analyses. Active regions are flagged with their respective NOAA numbers. The region associated with the X-class flares is indicated with a red label. The green circles are the 68% source location uncertainty regions (with systematic error added in quadrature); picture and caption are taken from [29].

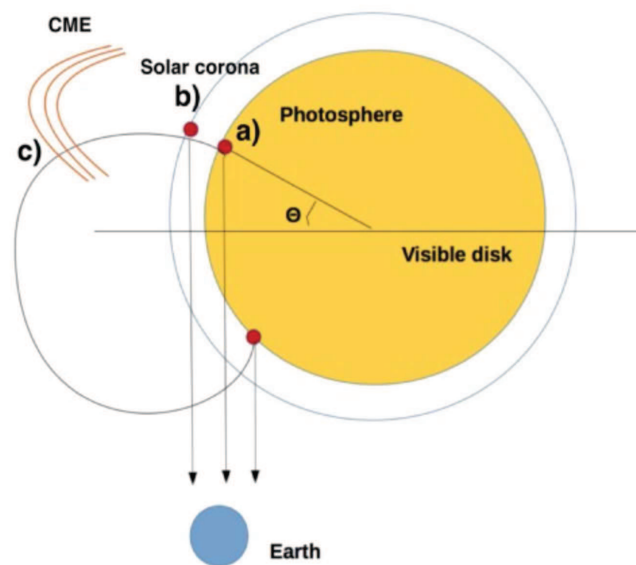


Figure 3.12: Cartoon representing different models for the observed gamma-ray emission associated to behind the limb flares. a) acceleration at the flare, gamma-ray emission site below the photosphere; b) acceleration at the flare, gamma-ray emission in the corona above the limb; c) acceleration (or re-acceleration) at the CME-shock, gamma-ray emission at the Sun. Figure and caption taken from [131]

3.3 Validation of new LAT event selections and improvements for solar flares studies

As previously explained, the event selection developed for the LAT has been periodically updated. Pass8 data represent a radical revision of the entire event-level analysis that includes every aspect of the data reduction process. The improvements include a significant reduction in background contamination, an increased effective area, a better point-spread function, a better control on the systematic uncertainties and an extension of the energy range below 100 MeV and above a few hundred GeV (See Par. 1.1.1). This means to improve the solar flares detection capabilities of the LAT, in particular at low energies; the increase in photon statistics will also allow to better constrain the spectral features and to reduce the uncertainties in localization studies. Moreover, a solar-flare dedicated event class selection has been developed by the Fermi-LAT collaboration: this alleviates the ACD pile-up effect present during impulsive phase solar flares [139].

Before the official release of Pass8 data (occurred in June 2015), we carefully tested the performances of new event classes comparing those specifically developed for solar flare analysis and those dedicated to the analysis of generic fast transient sources as GRBs. The checks have been performed on the whole sample of impulsive LLE-detected solar flares.

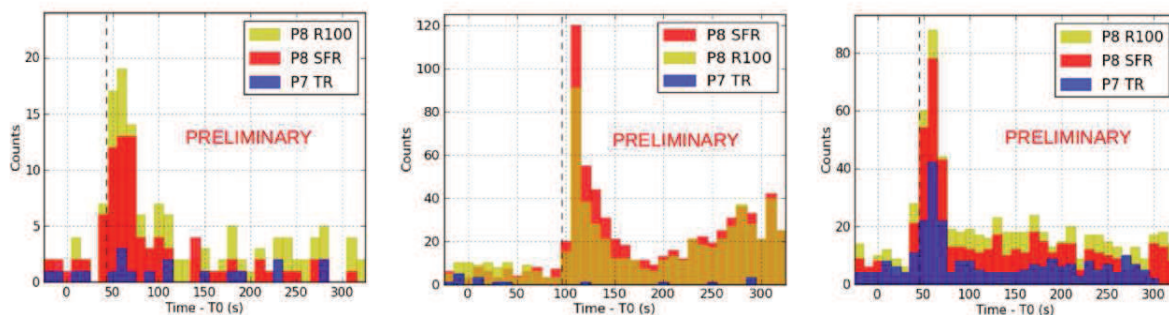


Figure 3.13: SOL2010-06-12 (left panel), SOL2011-09-06 (middle panel), SOL2012-06-03 (right panel). For each solar flare I compared the light-curves obtained using different event selections. Data are extracted in the energy range 35 MeV - 10 GeV. T0 is the GBM trigger time; the dashed line marks the P7-LLE detection time.

In Fig.3.13 I show a comparison of different LAT TRANSIENT data collected in the energy range 35 MeV - 10 GeV:

- P7 TR and P8 R100 are the loosest event classes for the the two different response functions Pass7 REP and Pass8;

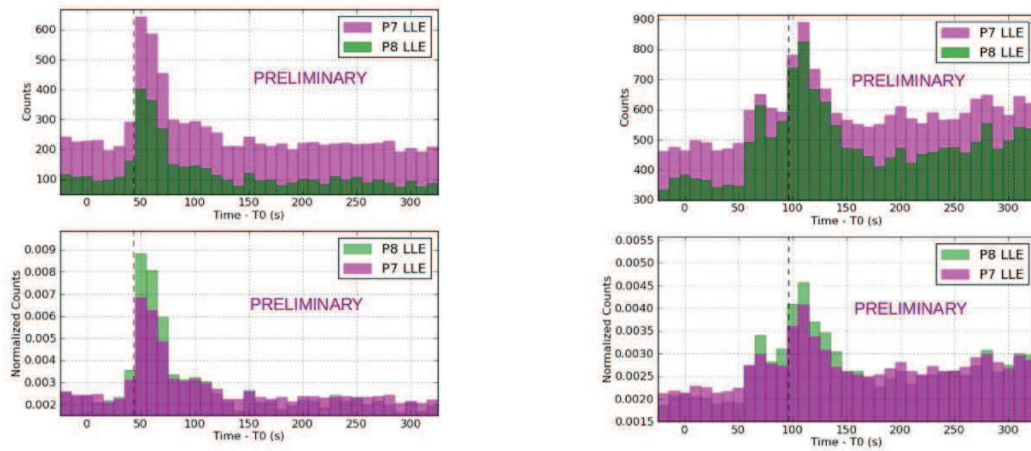


Figure 3.14: Light-curves obtained using Pass8 LLE data VS P7 LLE data for SOL2010-06-12 (left panel) and SOL2011-09-06 (right panel). For each flare, the upper plot shows the number of detected counts while the bottom plot shows the number of detected counts normalized to the total. T_0 is the GBM trigger time; the dashed line marks the P7-LLE detection time.

- P8 SFR is the solar flare optimized event class newly developed in Pass8.

Here I consider LAT observations of three different solar flares:

- SOL2010-06-12, M2.0 GOES class, already mentioned above;
- SOL2011-09-06, X2.1 GOES class, detected on 2011 September 06 22:17 UT;
- SOL2012-06-03, M3.3 GOES class, occurred on 2012 June 03 17:53 UT.

While impulsive and sustained gamma-ray emission from SOL2012-06-03 has been already detected using Pass7 standard event classes (even if with lower significance compared to Pass8 results), SOL2010-06-12 and SOL2011-09-06 were detected in Pass7 only through LLE technique [16]. Fig.3.13 shows that Pass8 event selection performs better both on previously detected and not-detected flares. Moreover, the P8 SFR event class, developed with a better treatment of ACD variables, produces a less noisy light-curve for all flares. In the case of SOL2011-09-06 (the highest GOES class flare of this sample), it results also in a greater number of total counts detected; the Pass7 signal is instead completely suppressed because of ACD pile-up caused by the intense X-ray flux.

I also tested the improvements of Pass8 event selection on LLE selection technique. In Fig.3.14 there is a comparison of light-curves obtained using Pass8 LLE data versus Pass7 LLE data for SOL2010-06-12 (left panel) and SOL2011-09-06

(right panel). The total number of detected counts (upper plots) is higher for P7 LLE since Pass8 event selection is less affected by background contamination but, as shown by the normalized number of detected counts (bottom plots), the P8 LLE light-curves provide a better signal-to-noise ratio.

Moreover, in order to validate the new LLE selection, that benefits not only from Pass8 improvements but also from a newly developed cut on ACD variables, and to determine the proper radius of acceptance for LLE data, two different types of event cuts have been tested. The first cut ("PSF1") allows to accept all events inside a radius that equals the LLE PSF acceptance radius; the second test has been performed using an acceptance radius twice times larger ("PSF2"). Calculating the Signal-to-Noise Ratio (SNR) for solar flares occurred at different inclination angle respect to the LAT z-axis, I found that (Fig.3.15):

- the "PSF1" selection gives a better SNR for all flares except the for high-inclination angles (magenta points are above the blue ones except for the last point at $\theta = 83$ deg corresponding to SOL2013-10-23);
- the new LLE selection, that take advantage of the new ACD cuts, clearly improves the SNR values (the stars are always above the dots).

To test the benefit of using Pass8 data for spectral analysis I produced LAT (40 MeV - 1 GeV) and GBM-BGO (0.3 - 40 MeV) spectra accumulated during the LLE-detection time range for SOL2011-09-06 and SOL2012-06-03. Using the tool XSPEC ⁴ I fit the data with these components (Fig.3.16 and Fig.3.17): a power-law for electron bremsstrahlung in the BGO energy range, a nuclear lines template, two Gaussian lines at 0.511 MeV and 2.223 MeV (related respectively to positron-electron annihilation and neutron capture) and a pion template in the high-energy part of the spectrum, similar to what has been done for the analysis of the June 2010 flare [15]. While a rigorous spectral analysis is beyond the scope of this specific plot, I'd like to stress that: spectral analysis is now possible using P8 standard event classes also during the impulsive phase of solar flares; and that for both flares analyzed, R100 data cover a slightly wider energy range compared with P7 LLE data.

⁴<http://heasarc.gsfc.nasa.gov/xanadu/xspec/>

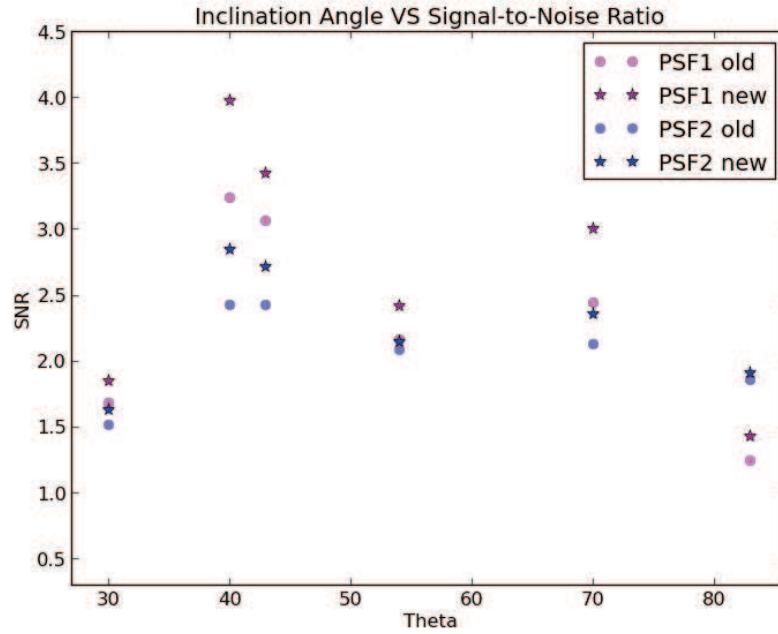


Figure 3.15: Estimation of the SNR for six LLE-detected solar flares using both 'old' and 'new' LLE cuts in order to understand which PSF cut is more appropriate according to the inclination angle of the flares respect to the LAT z-axis.

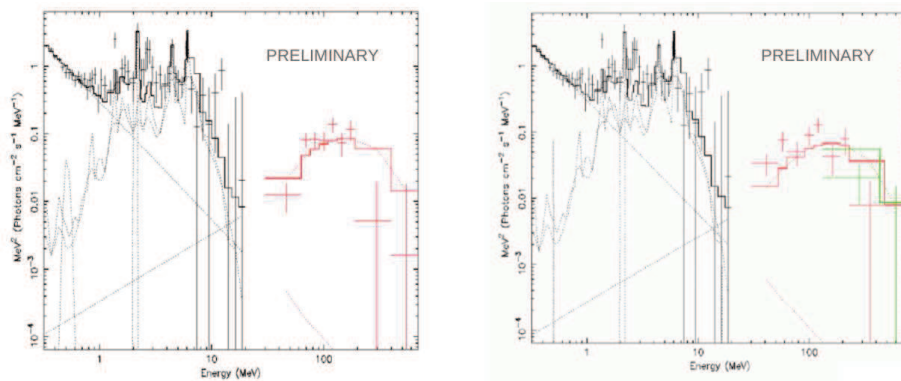


Figure 3.16: SOL2011-09-06: background subtracted count spectra obtained using GBM-BGO (black), P7 LLE (red, left panel), P8 LLE (red, right panel) and P8 R100 data (green, right panel).

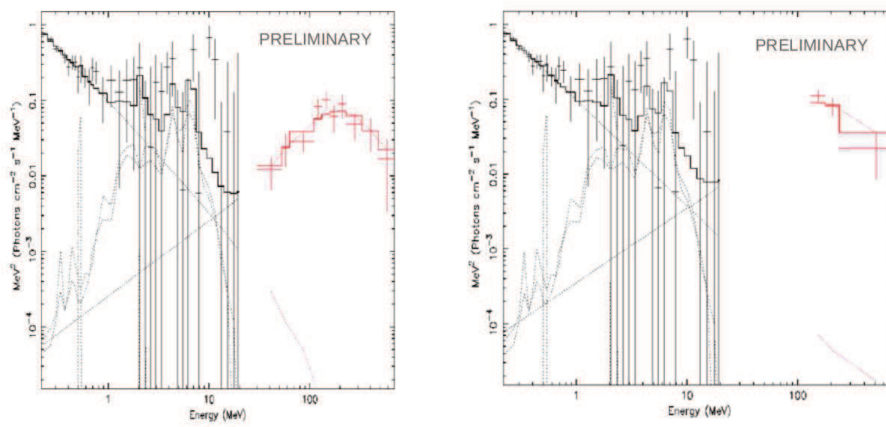


Figure 3.17: SOL2012-06-03: background subtracted count spectra obtained using GBM-BGO (black), P7 LLE (red, left panel) and P8 R100 data (red, right panel).

3.4 Spectral analysis of the impulsive phase of LLE-detected solar flares

I performed a detailed analysis of the impulsive phase of all solar flares detected using the LLE event selection (see first three and last two columns of the Table 3.1 for basic information.).

For each flare in this sample I performed a time integrated spectral analysis on a time bin coincident with the LLE detection interval. For this analysis I used GBM-BGO, LLE and, when available, LAT standard data. GBM NAI data usually suffer of pile-up (see e.g. the case of SF 110906) during the impulsive phase of solar flares so I preferred not including them in the spectral analysis.

GBM and LAT-LLE data have been downloaded from public repositories: the "Fermi-GBM Trigger catalogs"⁵ and the "Fermi LAT Low-Energy Events Catalog"⁶ respectively.

LAT standard data have been firstly downloaded from the public LAT data server⁷ and then extracted in the energy range 100 MeV - 10 GeV and in a Region of Interest (ROI) of 12 deg around the true sun position at GBM trigger-time. These last set of data has been included in the final joint spectral analysis only if a significant detection is found (i.e. for flares with $TS \geq 25$ ⁸ in table 3.1.)

3.4.1 Background estimation and fitting technique

To extract background and source spectra from LAT standard data I used the procedure described in [29] that consists of deriving the spectra directly from the models used in the standard LAT likelihood analysis, using the tools `gtlike` and `gtbkg`, and obtaining the response of the LAT using `gtrspgen`.

For GBM-BGO and LLE data I fitted the background using a polynomial function selecting two off-pulse regions right before and right after the detected emission. The procedure is performed using again the software `GtBurst`⁹ and it is the same procedure used by the Fermi-LAT collaboration for spectral analysis performed for the the first LAT GRBs' catalog (details in section 3.1 of [17]).

Response files for LLE data have been downloaded together with spectra from the above cited public website while GBM responses have been downloaded from the NASA web-page "Fermi Solar Flare X-Ray and Gamma-Ray Observations"¹⁰.

⁵<https://heasarc.gsfc.nasa.gov/W3Browse/fermi/fermigtrig.html>

⁶<https://heasarc.gsfc.nasa.gov/W3Browse/fermi/fermille.html>

⁷<http://fermi.gsfc.nasa.gov/cgi-bin/ssc/LAT/LATDataQuery.cgi>

⁸The source significance in sigmas is $\sim \sqrt{TS}$ assuming one degree of freedom.

⁹`GtBurst` is now released by the LAT collaboration together with the Fermi Science Tools.

¹⁰http://hesperia.gsfc.nasa.gov/fermi_solar/

Recall that the detector response matrices are needed in the spectral analysis software to relate observed count-rate spectra to model photon spectra.

The energy ranges selected for GBM-BGO data is 200 keV-40 MeV. I used LAT-LLE data from 40 MeV to 10 GeV if LAT standard data are not available. Otherwise I used only LAT standard data for $E > 100$ MeV.

I performed the combined Fermi-GBM and LAT fit using the XSPEC package [35]. The spectral fits were done minimizing the PGSTAT value which is likelihood function that takes into account Poisson errors on the source count spectrum and Gaussian errors on the background.

For each flare I also used a set of cut-offed power-laws to account for the low energy part of the spectrum and, when significant, two gaussian lines at 0.511 and 2.223 MeV and a template to reproduce the nuclear de-excitation induced spectrum. This last part consists of narrow (NRW) lines (with fractional widths of about 2% of the line energy), resulting from protons and a particles interacting with the ambient gas, and broad (BRD) lines (with fractional widths of about 20%) resulting from accelerated carbon and heavier nuclei interacting with ambient hydrogen and helium; in this last case the heavy nuclei retain a large fraction of their initial velocities, resulting in significant Doppler shifting. The nuclear lines templates used are based on a detailed study of the nuclear gamma-ray production from accelerated particle having a power-law distribution (with index s) interacting with elements in the solar atmosphere [126].

The high-energy part of the spectrum has been fitted testing a set of templates that reproduced the spectra expected from the π^0 decay produced by accelerated ions having differential power-law indices from -2.5 to -7.5. These templates are obtained using a model that represents a particle population with an isotropic pitch angle distribution and a power-law energy spectrum ($dN/dE \propto E^{-s}$, where E is the kinetic energy of the protons) interacting in a thick target medium with a coronal composition [153] taking $4\text{He}/\text{H} = 0.1$ [122].

The ratio of the fluxes of these two components is strongly dependent on the proton energy spectrum because the nuclear lines are produced mainly by lower energy protons (10-100 MeV), while the pions result from protons above at least several hundred MeV [122].

The results for the BRD/NRW lines, gaussian lines and pion-decay components are reported in Tab.3.2 only if adding them to the fit, the PGSTAT/DoF value gets lower.

3.4.2 Results

Tab. 3.1 shows a summary of likelihood analysis performed on LAT-only data. For each flare I reported the LAT event class that gives the highest TS, and the TS

| Trigger Name | Trigger Time | LLE start | LLE Stop | LAT re-processing | LAT event selection | TS PL | TS PL expcut | Theta | GOES class |
|--------------|---------------|-----------|----------|-------------------|---------------------|-------|--------------|--------|------------|
| bn100612038 | 297996907.645 | 44.293 | 74.393 | P8V2 | R020 | 33 | 28 | 70 deg | M2.0 |
| bn110809334 | 334569663.196 | 50.0 | 300.0 | P8V2 | 15S | 226 | 232 | 54 deg | X6.9 |
| bn110906929 | 337040239.88 | 50.0 | 150.0 | P8V2 | 15S | 312 | 333 | 43 deg | X2.1 |
| bn110924399 | 338549680.651 | 75.0 | 175.0 | P8V2 | LLE | – | – | 40 deg | X1.9 |
| bn120603745 | 360438755.902 | 46.922 | 67.022 | P8V2 | 15S | 286 | 293 | 30 deg | M3.3 |
| bn120806191 | 365920538.906 | 25.603 | 55.803 | P8V2 | LLE | – | – | 60 deg | M1.6 |
| bn121023135 | 372654884.555 | 52.042 | 72.042 | P8V2 | LLE | – | – | 83 deg | X1.8 |
| bn131025873 | 404427407.194 | 8.573 | 18.573 | P8V2 | LLE | – | – | 5 deg | M1.9 |
| bn131028083 | 404618343.902 | 14.988 | 85.288 | P8V2 | LLE | – | – | 5 deg | X1.0 |
| bn131028192 | 404627753.909 | 114.911 | 165.21 | P7REP | LLE | – | – | 5 deg | M5.1 |
| bn131028870 | 404686390.174 | 100.0 | 150.0 | P8V2 | LLE | – | – | 5 deg | M1.5 |
| bn140225029 | 414981690.957 | 200.0 | 600.0 | P8V2 | R020 | 119 | 120 | 81 deg | X4.9 |

Table 3.1: LLE-detected flares. Basic information and summary of LAT only analysis results.

obtained modeling the photon spectrum as a power-law (PL) and as a power-law with an high-energy exponential cut-off (PL exp-cut): in fact a curved spectrum at high-energies ($\gtrsim 60$ MeV) can reproduce the shape of the spectrum expected from the decay of neutral pions. Even if the curved model should better represent the physical emission process, sometimes, the TS obtained with the PL model is higher than the one obtained with the PL exp-cut model or the two TS values are comparable, with the second one not higher enough to justify the added complexity; this can be due to a lack of statistics in LAT standard data.

As reported also by [15], fitting the high-energy part of the spectrum using a PL can be justified thinking to a high-energy electrons bremsstrahlung component, but the hadronic origin is still preferred by theoretical speculation. This is why, in the joint spectral analysis, I used a pion-decay template to account for the high-energy part of the observed spectrum [122].

The best fit parameters of joint GBM and LAT spectral analyses together with photon flux estimates are summarized in Table 3.2.

These results can be used to obtain information on ions accelerated in the impulsive phase of these flares, as described in [123]. In particular, the nuclear de-excitation lines, neutron-capture line, and pion-decay fluences can be used to estimate the overall shape of the accelerated ion spectrum. These three emissions are produced by accelerated ions within distinct energy ranges: ~ 5 -20 MeV for the de-excitation lines, ~ 10 -50 MeV for the neutron capture line, and > 300 MeV for the pion-decay emission. Ratios of these emissions therefore determine the relative numbers of accelerated ions in the associated energy ranges. Moreover spectral indexes across these energy ranges can be inferred comparing measured ratios with

ratios from theoretical calculations (see [122] and the the subsequent [124, 125] based on updated nuclear cross sections).

Finally, the ratio of the flux in broad lines to the flux in narrow lines gives an estimate of the relative abundance of accelerated heavy particles to accelerated protons and is thus related to the composition of the solar cromosphere.

A summary of solar flares detected by the LAT until July 2012 has been already reported by [16]; comparing those results with results in Tab. 3.1 we can see that three (bn100612038, bn110809334, bn110906929) of the four flares now detected using Pass8 standard LAT data were not significantly detected using previous Pass7 event selection or the flux estimates were unreliable because of X-ray pile-up in the ACD. The work presented in this thesis is instead the first systematic combined spectral analysis of all impulsive LAT detected flares. Moreover, I developed a coherent analysis pipeline to perform such analyses: this is particularly useful because a re-analysis of these flares has to be performed as soon as all new GBM response files will be available. For solar flares science and especially for properly fitting lines, it is convenient to have ad-hoc response files of BGO detectors with 2999 true energy bins. This has been done for example for the analysis of the June 2010 flare [15] but the GBM team will provide them for all impulsive LLE-detected flares.

Looking at results listed in Tab.3.2 we can see that the proton index spans values from -2 to -6. When this value is poorly constrained or the pion component is not significant, higher values of the cut-off energies suggest that the cut-offed power law component account for part of the ≥ 60 MeV emission and that the bulk of emission observed in gamm-rays is concentrated below ~ 100 MeV. This is also confirmed by the fact that these flares are not significantly detected using the LAT standard event selection that is particularly efficient for the detection of ≥ 100 MeV emission.

Final results of the spectral analysis performed using final GBM response files will be important to characterize the global properties of impulsive flares and will be included in the first catalog of solar flares detected by the LAT (in preparation).

Another future improvement to the analysis could arise from performing a time resolved spectral analysis. In fact, for some solar flares (e.g. bn110906929 and bn140225029), the comparison of light curves obtained with LLE and in LAT-standard data showed a hint of spectral evolution. The time intervals for the time-resolved spectral analysis will be chosen using the Bayesian-blocks (BB) algorithm [160] implemented in the software GtBurst. Fig. 3.24 shows the LLE light curves for solar flares bn110906929 and bn140225029; the red dashed lines mark the P8-LLE detection time while T0 is the GBM trigger time. The BB algorithm has been applied and the obtained temporal bins are indicated by the black thin lines. All found variations have a significance larger than 3σ .

| | | | |
|---------------------|---------------|---------------|----------------|
| | bn100612038 | bn110809334 | bn11090929 |
| PG-stat (DoF) | 293 (168) | 3927 (169) | 287 (149) |
| Index 1 | 1.20 +/- 0.07 | 1.0 +/- 0.4 | 1.77 +/- 0.09 |
| Index 2 | 3.60 +/- 0.09 | 2.34 +/- 0.02 | 4.22 +/- 0.003 |
| Ecut (MeV) | 2.5 +/- 0.8 | 7.3 +/- 1.3 | 6.9 +/- 0.6 |
| proton index | 4.5 +/- 1.5 | 6.0 +/- 0.8 | 6.0 +/- 1.6 |
| n. capture line | significant | - | significant |
| e+/e- annihil. line | significant | - | - |
| s (BRD/NRW) | 4.2 +/- 0.5 | 4.2 +/- 0.8 | 4.2 +/- 0.2 |
| Flux | 80. +/- 10. | 2.4 +/- 2.3 | 3.5 +/- 0.2 |
| | bn110924399 | bn120603745 | bn120806191 |
| PG-stat (DoF) | 1036 (149) | 174 (168) | 175 (152) |
| Index 1 | 2.00 +/- 0.07 | 2.97 +/- 0.05 | 1.59 +/- 0.03 |
| Index 2 | 4.7 +/- 0.1 | 2.9 +/- 3.6 | 8.1 +/- 1.0 |
| Ecut (MeV) | 8.9 +/- 0.4 | 0.3 +/- 0.1 | 32 +/- 4 |
| proton index | 4.4 +/- 0.5 | 6.0 +/- 0.9 | 4.6 +/- 6.0 |
| n. capture line | significant | significant | - |
| e+/e- annihil. line | - | - | - |
| s (BRD/NRW) | 4.2 +/- 0.5 | 4.0 +/- 0.5 | - |
| Flux | 1.0 +/- 0.9 | 8.1 +/- 7.8 | 13. +/- 10. |
| | bn121023135 | bn131025873 | bn131028083 |
| PG-stat (DoF) | 255 (152) | 130 (152) | 681 (150) |
| Index 1 | 1.00 +/- 0.07 | 2.0 +/- 0.4 | 2.0 +/- 0.1 |
| Index 2 | 3.15 +/- 0.01 | 0.1 +/- 0.9 | 4.7 +/- 0.4 |
| Ecut (MeV) | 24 +/- 3 | 14 +/- 4 | 5.6 +/- 0.3 |
| proton index | - | - | 2.7 +/- 1.3 |
| n. capture line | - | - | - |
| e+/e- annihil. line | - | - | - |
| s (BRD/NRW) | 2.6 +/- 1.2 | 4.2 +/- 1.7 | 2.6 +/- 3.4 |
| Flux | 104 +/- 75 | 1.8 +/- 0.1 | 0.11 +/- 0.09 |
| | bn131028192 | bn131028870 | bn140225029 |
| PG-stat (DoF) | 1239 (150) | 431 (150) | 46101 (149) |
| Index 1 | 1.9 +/- 0.2 | 1.7 +/- 0.4 | 1.0 +/- 1.5 |
| Index 2 | 3.6 +/- 0.1 | 3.3 +/- 0.1 | 4.14 +/- 0.08 |
| Ecut (MeV) | 9 +/- 2 | 48 +/- 22 | 34 +/- 24 |
| proton index | 4.5 +/- 3.9 | 2.5 +/- 3.0 | 5.0 +/- 0.5 |
| n. capture line | - | - | significant |
| e+/e- annihil. line | - | - | - |
| s (BRD/NRW) | 2.8 +/- 0.4 | 2.6 +/- 1.0 - | 3.4 +/- 1.9 |
| Flux | 0.4 +/- 0.2 | 0.8 +/- 0.1 | 100 +/- 53 |

Table 3.2: LLE-detected flares: results of the joint GBM and LAT time-integrated spectral analysis. Flux (in units of 10^{-4} ph cm $^{-2}$ s $^{-1}$) calculated in range 40 MeV - 10 GeV.

LLE light curves for other flares in the sample are shown in Fig.3.25

Solar flare bn110906929: a test case

Figures 3.18 and 3.19 show an example of counts map for flare bn110906929: note the predominance of SFR events during the early phase.

Figures 3.20 and 3.21 show GBM light-curves: note that, as already mentioned, I did not use NAI data for the spectral analysis also because they often suffer of pile-up during impulsive flares.

Finally, Figures 3.22 and 3.23 show the combined GBM and LAT photon spectrum accumulated over the LLE-detection time interval; the last plot shows the fit for which parameters are reported also in Tab.3.2.

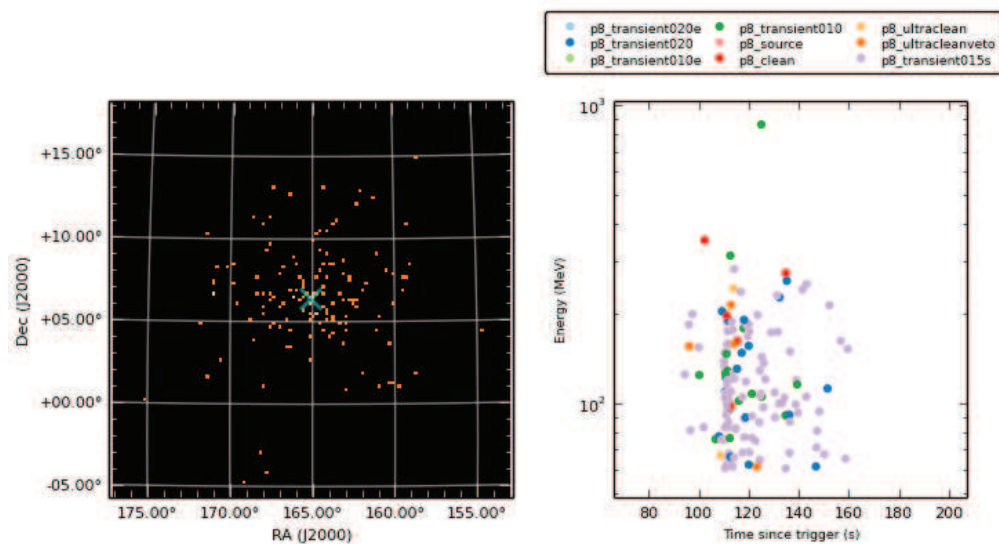


Figure 3.18: bn110906929: counts-map (left) and light-curve of LAT transient data accumulated \sim during the LLE-detection time interval. The violet dots indicates the event-class R15S, specifically developed for the analysis of the impulsive phase of solar flares.

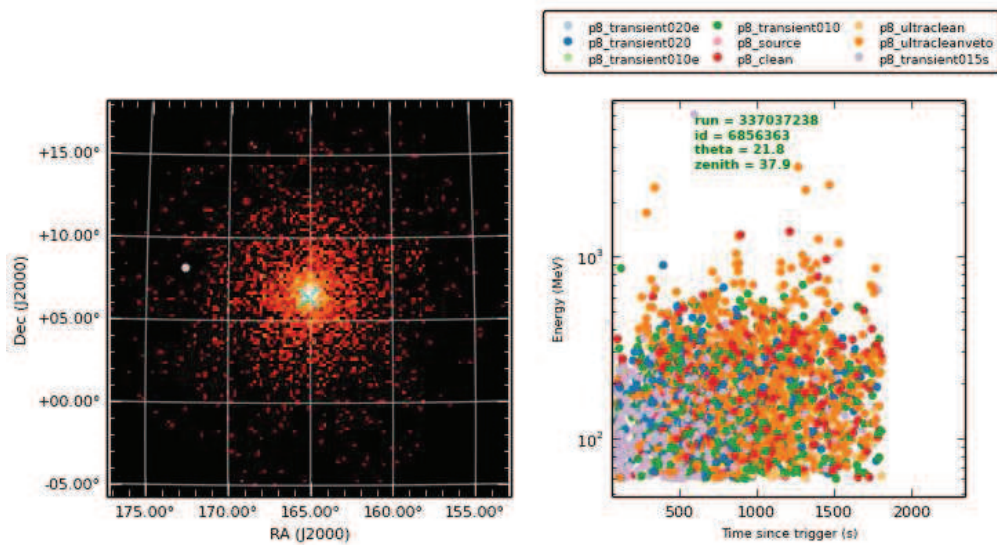


Figure 3.19: bn110906929: counts-map (left) and light-curve of LAT transient data accumulated during the first orbit i.e. when the Sun was still in the LAT FoV and before the spacecraft entered the SAA. Note that the R15S events dominates during the early/impulsive part of the flare emission while transient R010,SOURCE and cleaner event classes better sample the long-lasting emission.

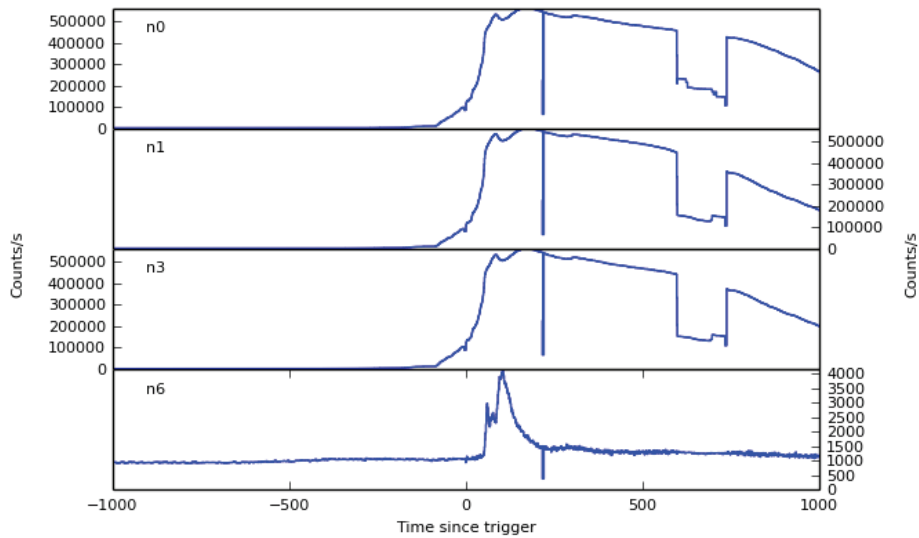


Figure 3.20: bn110906929: GBM-NAI light-curves of sunward detectors. I did not use these data for the spectral analysis since they suffered of pile-up and, in the case of b6, of occultation by part of the spacecraft itself.

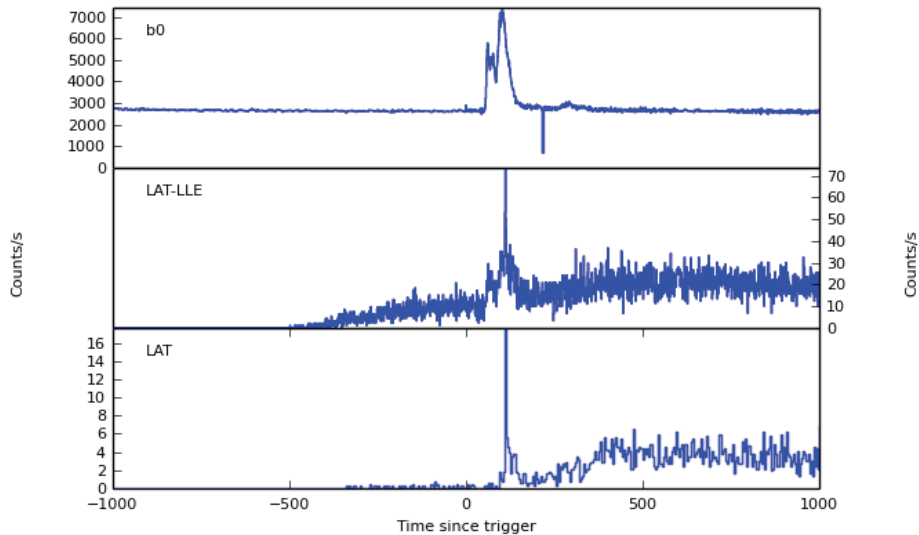


Figure 3.21: bn110906929: comparison between the BGO-b0, LAT-LLE and LAT transient light-curve. Note that the LLE data ($>30\text{MeV}$) correlate better with BGO respect to LAT standard ($>100\text{ MeV}$).

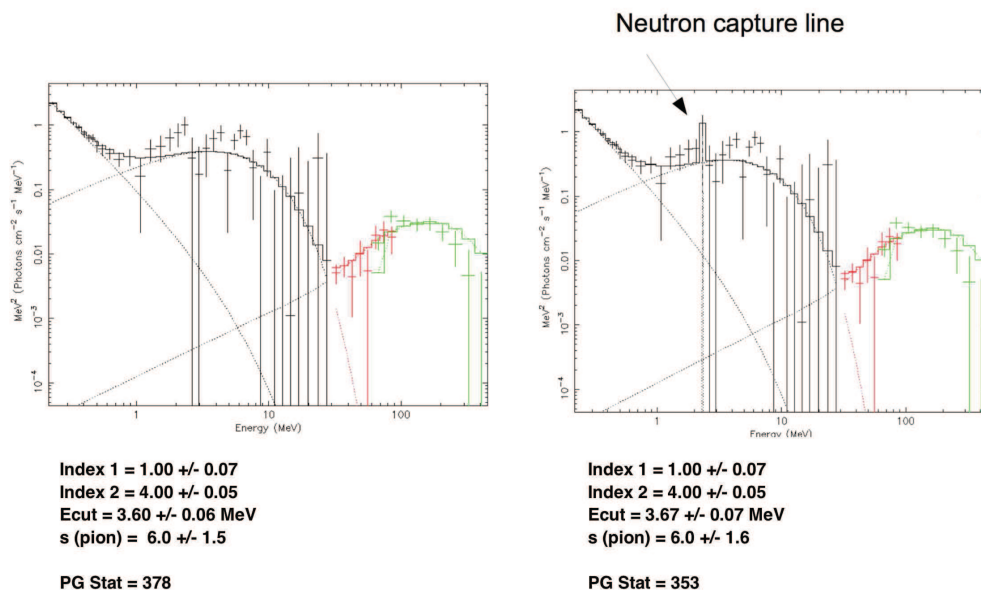
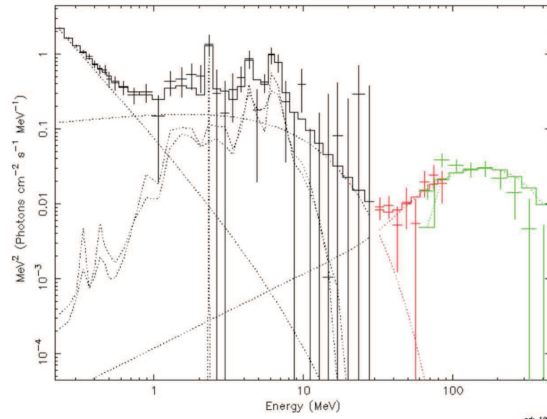


Figure 3.22: bn110906929: combined GBM and LAT photon spectrum accumulated over the LLE-detection time interval, fitted using only the "base model" (on the left) and adding a gaussian line representin the neutron capture line at 2.223 MeV (on the right).



Index 1 = 1.77 +/- 0.09
Index 2 = 4.22 +/- 0.03
Ecut = 6.9 +/- 0.6 MeV
s (pion) = 6.0 +/- 1.6
BRD/NRW s = 4.2 +/- 0.2

PG Stat = 287

Figure 3.23: bn110906929: combined GBM and LAT photon spectrum accumulated over the LLE-detection time interval. Here, a component to account for the nuclear de-excitations lines has been added to the model in Fig.3.22

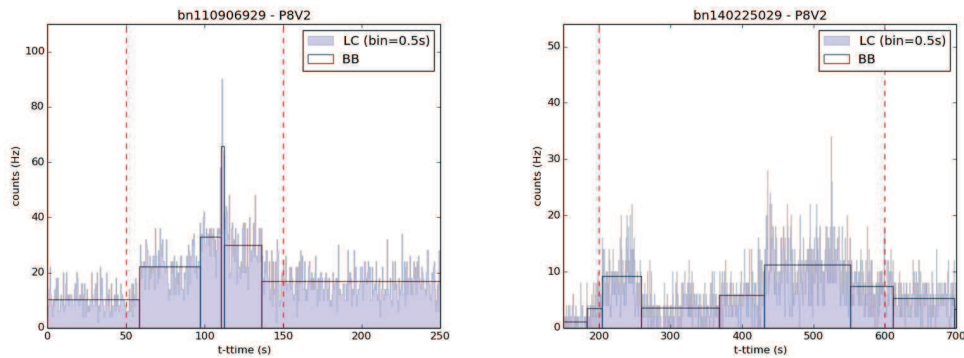
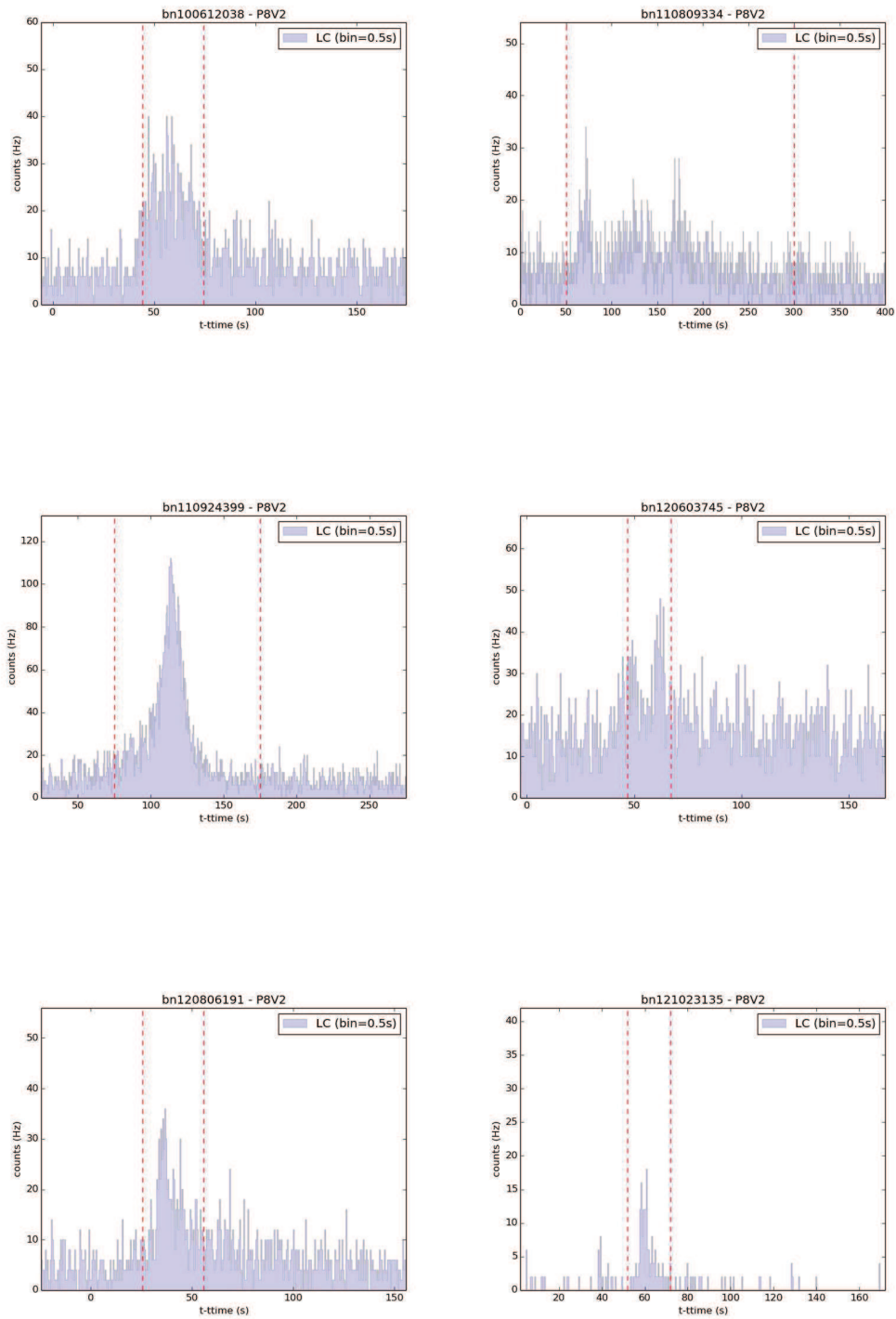


Figure 3.24: P8 LLE light curves for SF110906929 and SF140225038. The red dashed lines mark the P8-LLE detection time while T_0 is the GBM trigger time. The Bayesian-block algorithm has been applied and the obtained temporal bins are indicated by the black thin lines.



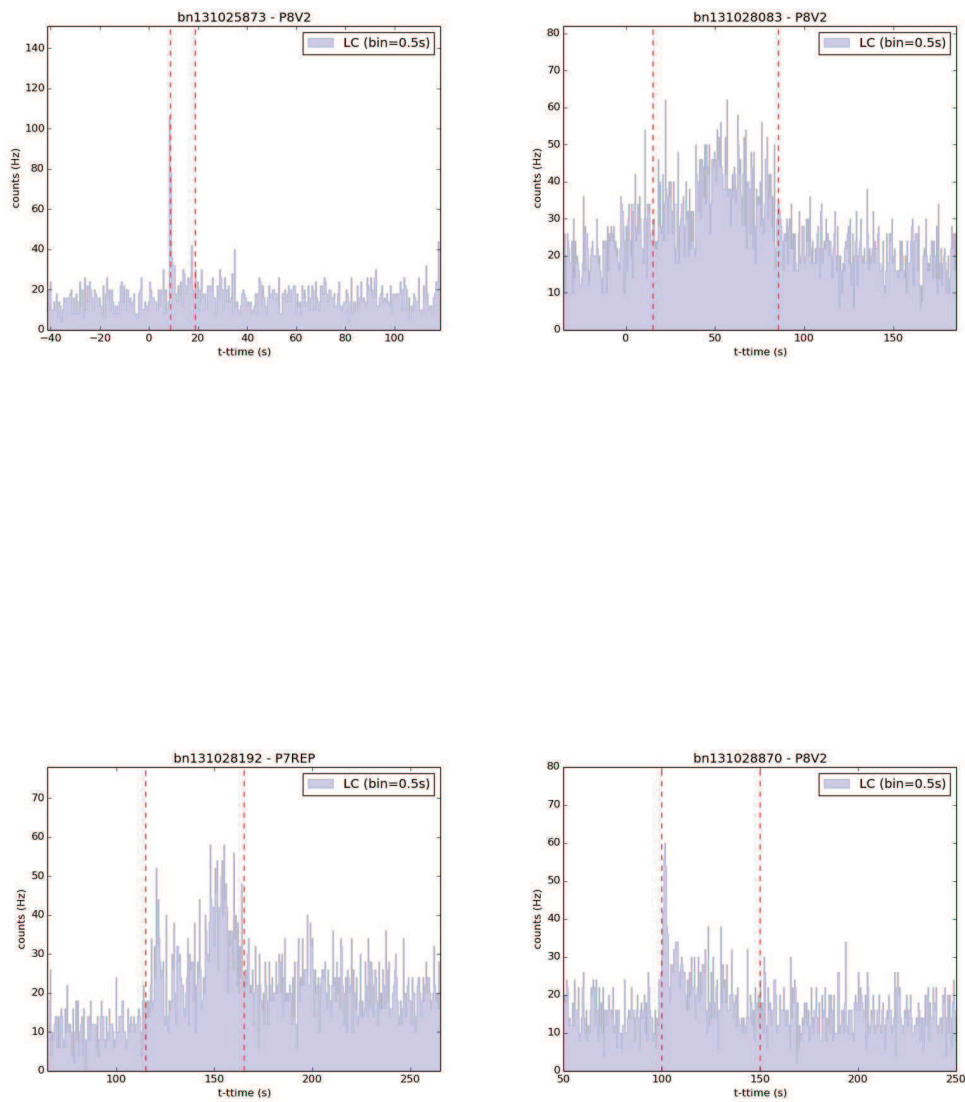


Figure 3.25: LLE light curve for all solar flares in my sample; the red dashed lines mark the P8-LLE detection time while T0 is the GBM trigger time.

Chapter 4

Active Galactic Nuclei

The term "Active Galactic Nuclei" (AGN) refers to galaxies showing evidence of energetic phenomena in their central region which cannot be attributed to stellar and/or dust emission. Most of the emission observed is indeed non-thermal and AGN are able to produce much more power than an entire galaxy in a volume which is comparable with our Solar System.

Historically, the two largest sub-classes of AGNs are considered *Seyfert galaxies* and *quasars*. The fundamental difference between them is in the amount of radiation emitted by the compact central source: for a typical Seyfert galaxy, the total energy emitted by the nuclear source at visible wavelengths is comparable to the energy emitted by all of the stars in the galaxy (i.e., $\sim 10^{11} L_{\odot}$), while in a typical quasar the central source is brighter than the stars by a factor of 100 or more [142]. Seyfert galaxies (named after Carl Seyfert who first described this class in 1943) display emission lines in optical spectra implying interactions with gas clouds having velocities from ~ 500 to 5000 km/s: faster and denser clouds are supposed to be very close to the nucleus while narrower lines arise from low density gas clouds at larger distances.

Quasars were first identified in the sixties thanks to the improvements achieved in radio astronomy; the name is an abbreviation of *quasi-stellar radio objects* because the optical telescopes identified these objects, which can be as extended as arcminutes in radio maps, as a point-like objects looking exactly like stars.

The first breakthrough in understanding the real nature of these objects came when Maarten Schmidt [163] found that the emission lines seen in the spectrum of 3C 273 were actually the hydrogen Balmer-series emission lines at an uncommonly large redshift ($z = 0.158$) probing its cosmological and not-stellar nature.

The process that powers the stars, i.e. thermonuclear reactions, is not enough to power quasars. For this reason it was soon speculated [159, 181, 112, 165] that at the core of these sources there is a massive black hole: matter around it is attracted by the black hole gravity, it is compressed and heated, and then radiates.

Another major advance came when X-ray observations (in the sixties and in the early seventies) established that quasars were strong X-ray emitters. Moreover with the improvements of the interferometric technique in the radio band, in the early seventies, radio telescopes could resolve details as close as a few tenths of a millisecond of arc enabling to discover that some radio emitting quasars have spots of radio emission which are observed to move: given the huge distances, this motion corresponds to velocities that exceed the speed of light: this "superluminal" motion corresponds to fast motion, but slower than the velocity of light, at an angle close to our line of sight [154].

Despite the fact that the first quasars discovered were radio-loud, we now know that these kind of AGNs are only about the 10% while the majority are radio-quiet [79, 142].

4.1 A model for AGN emission

The most widely accepted model that comprises the observed features of different active galaxies postulates that the basic structure of AGNs includes [79]:

- a black hole, with mass $10^6 M_{\odot} < M < 10^9 M_{\odot}$; it is likely spinning, due to energetic requirements, but there are still no measurements of the spin value.
- An accretion disk: matter attracted by the black hole gravity, spirals in and forms a disk; this is also the major source of power.
- An X-ray corona, around the accretion disk: it is supposed to be a hot layer, or an ensemble of clumpy regions particularly active in the inner parts of the disk.
- An obscuring torus located at several parsec¹ from the black hole, intercepting some fraction of the radiation produced by the disk and re-emitting it in the infrared.
- A region of many small clouds at a distance < 1 pc from the hole, moving rapidly ($\sim 3000 \text{ km s}^{-1}$). As cited above, the clouds intercept $\sim 10\%$ of the ionizing radiation of the disk, and re-emit it in the form of lines broadened via Doppler shifts; this region is called Broad Line Region (BLR).
- Another region, at larger distance (~ 100 pc), where less dense clouds are moving slower; it is called Narrow Line Region (NLR).

¹The parsec (pc) is a unit of length used to measure large distances to objects outside our Solar System. It's defined as the distance at which one astronomical unit subtends an angle of one arc-second. One parsec is equal to about 3.26 light-years (3.08×10^{16} m).

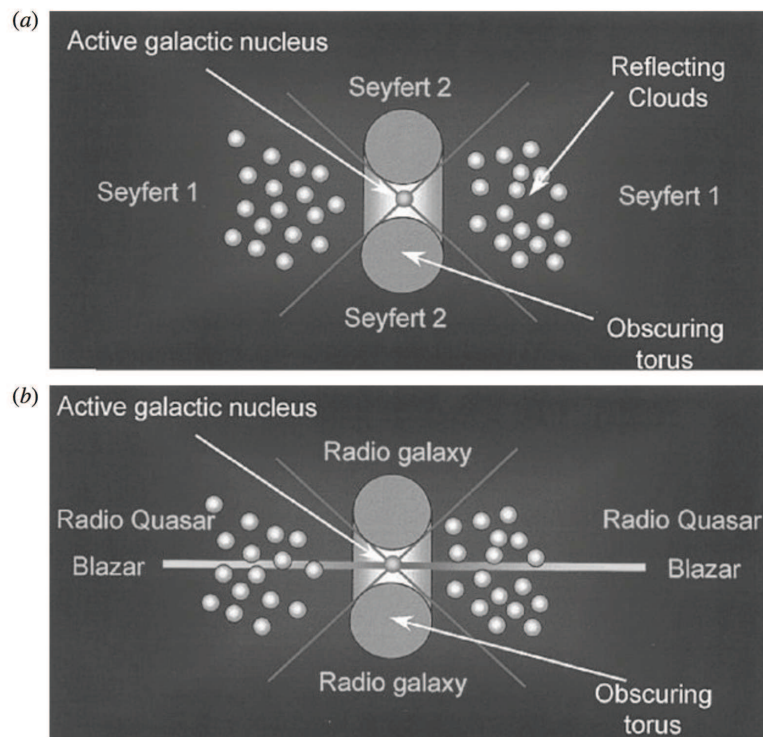


Figure 4.1: A schematic diagram illustrating the unified picture for AGNs. In particular, the (b) panel illustrates the unified model for radio galaxies and radio quasars: quasars are observed when the axis of the radio source lies within about 45 deg of the line of sight. When observations are made almost along the axis of the radio jet, superluminal radio sources and blazars are observed [108].

Finally, about 10% of AGNs, are able to expel matter in two oppositely directed jets. Their direction likely traces the rotational axis of the spinning black hole and the material inside these jets is moving at relativistic speeds: therefore the jet emission is highly beamed, and their appearance depends on the viewing angle. AGNs whose jets are pointing at us, or are observed at a small inclination angle, are called *blazars*.

Fig.4.1 show the widely accepted unification model for AGNs.

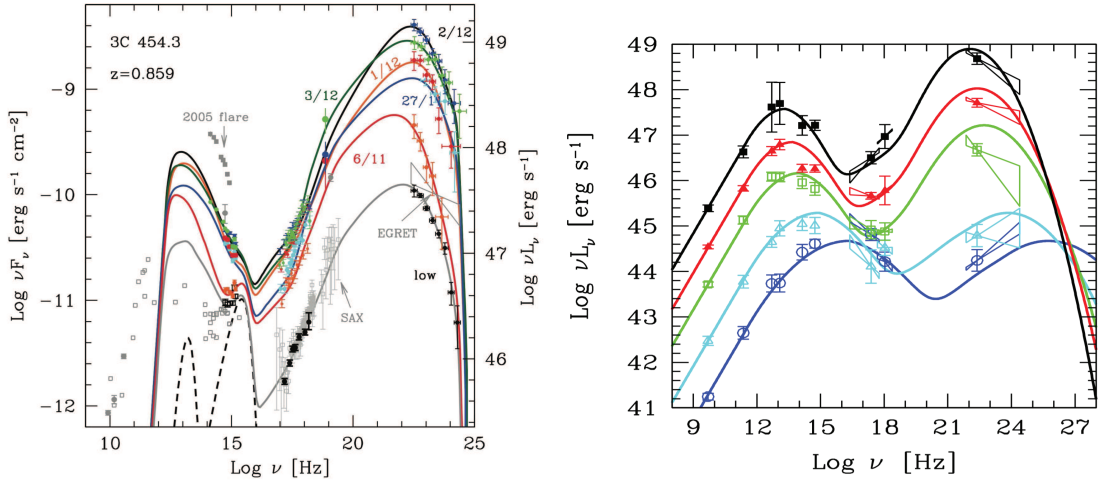


Figure 4.2: On the left: broadband SED of 3C 454.3 (dates refer to 2009): note the large amplitude variability, even daily. Lines correspond to different fitting models [48]. On the right: the so called "blazar sequence". As the bolometric luminosity increases, the peak of the two humps shifts to smaller frequencies, and the high energy hump becomes more important. It was constructed taking the average luminosity in selected bands, and considering ~ 100 blazars coming from radio and X-ray samples [67].

4.1.1 Blazars: main characteristics and variability

Blazars are usually divided in two classes. *BL Lac objects* (BL Lacs) that have weak or absent optical lines with equivalent width² $< 5 \text{ \AA}$. *Flat Spectrum Radio Quasars* (FSRQs) instead show strong emission lines, with $\text{EW } 5 > \text{ \AA}$, reflecting dense BLR material and strong illuminating accretion-disk radiation.

Blazars emit over the entire electromagnetic spectrum, from the radio ($\lesssim 10^7$ Hz) to the TeV energy band (up to 10^{27} Hz). Their overall spectral energy distribution (SED) plotted in νF_ν , shows two broad peaks: the first peak is between the mm and the soft-X-ray band, while the high energy peak is in the MeV-GeV band. The high energy hump often dominates the power output. Blazars are variable, at all frequencies, but especially at high energies with minimum variability timescales between weeks and tens of minutes. The variability is often simultaneous in different energy bands. In restricted energy ranges, the observed spectrum is a power law.

²The equivalent width is a measure of the strength of a spectral line: it is the width of a rectangle centered on a spectral line that, on a plot of intensity against wavelength, has the same area as the line.

Fig.4.2 (left panel) shows the SED of 3C 454.3, a powerful FSRQ and one of the brightest blazar detected in γ -rays. The extraordinary variability, encompassing 2 orders of magnitude in flux, both in the γ -ray band and in the optical can be noted.

It seems also that blazars form a sequence of SEDs, according to their observed bolometric luminosity (Fig.4.2 on the right). Note that low powerful objects have both peaks at a similar level of luminosity, and located at higher frequencies than in more powerful objects. In the BL Lac class, the first kind of sources were named High frequency peaked BL Lacs (HBL) while the latter subclass was called Low frequency peaked BL Lacs (LBL) [136].

The first hump of the SED is universally thought to be non-thermal synchrotron emission from relativistic jet electrons. Since it sometimes varies rapidly and simultaneously (at least in optical, UV and soft-X-rays bands), it is believed to be produced in a single region of the jet.

The higher frequency hump, which peaks from $\lesssim 100$ MeV to VHE, is widely thought to originate from inverse Compton scattering of ambient photons by the same electrons producing the synchrotron radiation. The ambient synchrotron radiation provides a target field in all models. In **synchrotron self-Compton** (SSC) models, only the synchrotron photons provide targets while in **external Compton** (EC) models, photons are produced outside the jet and intercept the jet to be scattered.

4.1.2 Gamma-ray observations

A big contribution to the current understanding of the blazar phenomenon has been provided by EGRET, which found that blazars are the largest class of identified and variable gamma-ray sources at energies above 100 MeV. EGRET blazars showed variations on timescales from days to months. Gamma-ray flares on short timescales (1-3 days) have been detected from various sources [129, 174] and some giant γ -ray outbursts were also observed [88].

Very rapid variability at VHE was also reported e.g. by HESS in 2006 in for PKS 2155-304 [25] and in 2009-2010 by MAGIC in the case of IC 310 [31].

Given its characteristics, in particular in terms of FoV, energy range and effective area, the LAT represented an unprecedented instrument to monitor the variability emission of blazars in gamma-rays.

Only using data from the first eleven months of survey, the LAT collaboration was able to characterize the variability of 106 bright blazars [12]. More than 50% of these sources are found to be variable with high significance, where high states do not exceed 1/4 of the total observation range. Variation amplitudes are larger for FSRQs and low/intermediate synchrotron frequency peaked BL Lac objects. The study of variability is particularly important in gamma ray astronomy; it

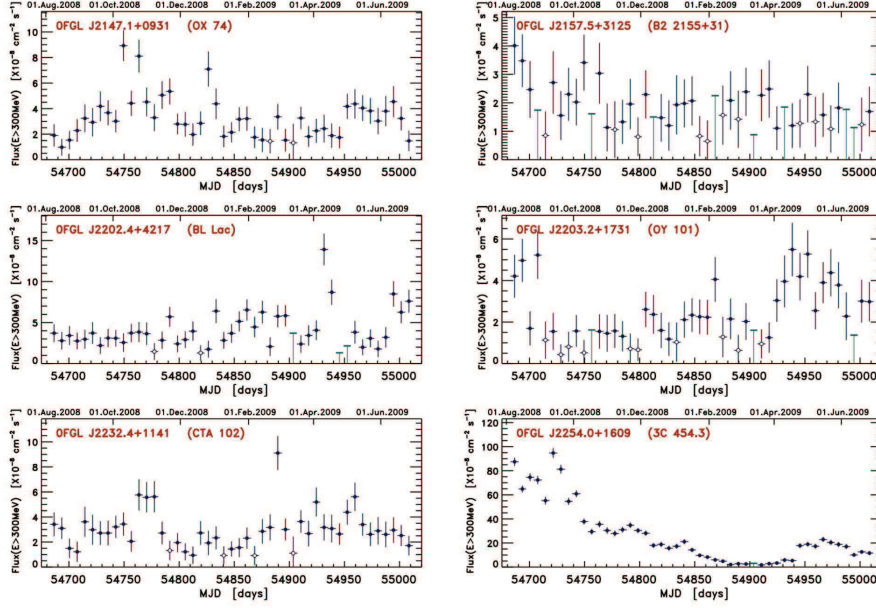


Figure 4.3: A diversity of blazars gamma-ray light-curves observed by Fermi [12].

assists in detecting faint sources, discriminating between real point sources and back-ground fluctuations. Moreover, correlated multi-wavelength variability helps to recognize and identify the correct radio/optical/X-ray source counterparts within the gamma-ray position error box. Finally, the detailed characterization of gamma-ray variability for unidentified sources can also help in identifying the correct source class [129].

The apparent γ -ray luminosities of blazars averaged over time scales of years range from $\sim 10^{44}$ erg s^{-1} to $\lesssim 10^{49}$ erg s^{-1} [22]. During flaring episodes, the luminosity can be much higher: for example 3C 454.3 reached a record $\sim 2 \times 10^{50}$ erg s^{-1} (measured in the energy range 100 MeV - 200 GeV) during its exceptionally active period in November 2010 [11]. Note that the absolute luminosities are reduced from the apparent luminosities by a beaming factor $\sim 10^2$, which gives the fraction of the solid angle into which the radiation is beamed. Even so, the luminosities are enormous, especially considering that the Eddington luminosity for a black hole with mass $\sim 10^9 M_{\odot}$ is $\sim 10^{47}$ erg s^{-1} . The measured variability times can be also much shorter than a day (see, e.g., [31]); causality arguments require that the radiation originates from a compact region of light days or less. The light-crossing time corresponding to the Schwarzschild radius of a $10^9 M_{\odot}$ black hole is $\sim 10^4$ s. Again, the simplest and only widely accepted explanation for the enormous luminosities and short timescales is that the blazar engine is a supermassive black

hole [64].

The Third LAT Catalog of Active Galactic Nuclei [19] using the first four years of the Fermi-LAT data lists 1444 γ -ray AGN: $\sim 30\%$ FSRQs (404 sources), $\sim 40\%$ BL Lac objects (604 sources), $\sim 30\%$ blazars of unknown type (402 sources, typically associated to high-latitude γ -ray excesses over the background associated with counterpart radio sources having poor optical follow-up). Less than 2% of the sample (only 24 sources) are non-blazar AGNs (mainly radio galaxies, radio-loud narrow line Seyfert galaxies, and candidate Seyfert AGNs).

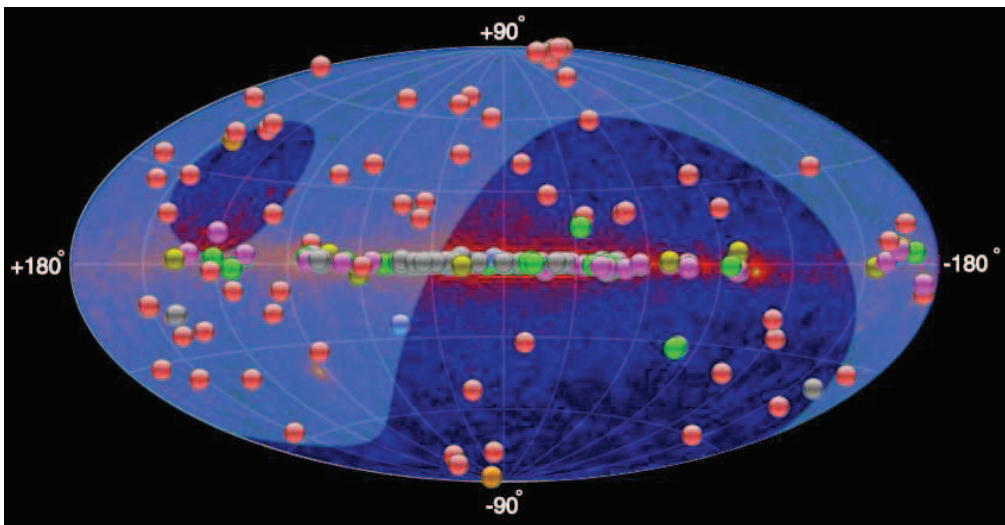


Figure 4.4: An image of the sky taken from TeVCat. The red dots refers to active galaxies. The contours indicate the portion of the sky available for MAGIC observations while a LAT sky-map is visible as background image.

Observational VHE astronomy has made tremendous progress over the last decade (see e.g. [93]) thanks to current generation of ground based IACTs, such as H.E.S.S., MAGIC and VERITAS; this is especially true for the detection of AGN at VHE. The number of confirmed detected blazars in the TeV range, according to the current version of the on-line catalog TeVCat³, is ~ 63 . Among these, only five are FSRQs while the main part (46) are HBL (see. Fig.4.4).

While the classification between the various kinds of blazars is still a matter of debate, it is clear in any case that the sample of AGN detected at VHE includes more than 90% of presumably beamed sources. The AGN sample is largely dominated by the HBL sources which, following the blazar sequence, have a synchrotron peak at high frequencies above 10^{15} Hz [168].

³tevcats.uchicago.edu, more details in [179].

The redshift distribution, as reported by the TeV-Cat, spans values from 0.00183, referred to the nearby radiogalaxy Cen A, to above 0.9 with the two distant blazars S30218+35 and PKS1441+25. Most of the sources detected at the moment are at redshift smaller than 0.3, which is due both to the sensitivity of the current experiments but also to the fact that VHE gamma-rays interact with the extragalactic background light (EBL), inducing pair creation, and can therefore be significantly absorbed during their propagation in the intergalactic space.

Despite a relatively poor time coverage due to the IACTs duty cycle, most of blazars appear variable at VHE, over timescales from a few minutes to years.

Because of the extremely variable nature of blazars, multiwavelength campaigns have to be organized by different observational facilities in order to obtain simultaneous or contemporaneous measurements of the SEDs. As a result of these campaigns, the multi-wavelength spectra for a few dozen blazars are fairly well measured from radio to VHE γ -ray energies.

Studies of flares and variability in different spectral bands and correlations of multi-waveband variability patterns allow to shed light on the physical processes in action in blazars, such as particle acceleration and emission mechanisms, relativistic beaming, origin of flares and size, structure and location of the emission regions.

In addition to AGN physics, the AGN flares can also be used to study the EBL and investigate fundamental physics topics e.g. searching for Lorentz Invariance Violation and Axion Like Particles. Finally the flares also have great discovery potential: usually FSRQs and low synchrotron peaking sources in general, can only be detected when they are flaring; this is true also for very distant blazars and can be true also for those classes of γ -ray AGN that are still undetected in the VHE regime e.g. the Narrow line Seyfert1 galaxies.

4.2 Fermi-LAT and MAGIC joint observational effort

The main part of TeV sources have been detected during pointed observations of selected targets, already known from multiwavelength data to be potentially active at VHE. In fact IACTs have relatively small FoV and low duty cycle ($\sim 10\%$) especially compared with Fermi-LAT, that, as already mentioned, can observe $\sim 20\%$ of the sky at any time and has a much higher duty cycle ($\sim 85\%$).

For this reason a prompt communications between the different observatories in order to trigger multiwavelength observations of variable sources is very useful. This is usually done through the Astronomer's Telegram network⁴ (ATel), the Gamma-ray Coordinates Network⁵ (GCN) and thanks to ad-hoc agreements between the different scientific collaborations.

In order to have more detailed prompt information about the evolution of the flux and especially on the spectral shape of sources in "high-state", I developed an analysis pipeline to perform real-time fast analyses of Fermi data on a selected number of interesting sources to provide a feedback useful for the AGN MAGIC working group for a decision about the re-pointing of the telescopes.

This work has been done in collaboration with the MAGIC/Fermi group at Udine University and INFN Trieste and is part of a scientific proposal carried on by the MAGIC collaboration dedicated to the ToO observations of flaring AGNs based on optical, X-ray and γ -ray triggers, the so-called "Mother of ToO Proposal".

4.2.1 Automated Fermi-LAT analysis pipelines

Technical description

The analysis pipelines are currently running on a virtual machine at Udine University⁶. We started our monitor analysis at the beginning of 2013; since then we have been improving the initial basic strategy of analysis and the list of sources to monitor in agreement with the MAGIC scientific goals.

Up to now we have implemented two different kind of analysis strategies: the first one, called "*Fermi-weather*", is focused on interesting sources which show some kind of activity in other wavelengths in a time period very close to the current observing time and that contemporaneously lay in the MAGIC FoV. To have an idea of the number of sources usually in this list, we are now monitoring ~ 70 sources on a daily basis; the results of these analyses are available at about 12

⁴<http://www.astronomerstelegram.org>

⁵<http://gcn.gsfc.nasa.gov/>

⁶Technical details: 8 CPU, 32 GB RAM, 1 TB hard disk space and about 8 effective TB available on an external storage.

AM CET every day and distributed by email at the MAGIC AGN and galactic working-group members. Each sources is analyzed using data updated at 6 PM UTC of the day before. This choice has been done because we had to find a trade-off between two needs: using most updated data and having results in time to eventually trigger target-of-opportunity (ToO) observations and to carefully plan the MAGIC observing schedule for the upcoming night.

MA⁴U report (generated Wednesday 27th July, 2016 @ 11:34 CET)

| source | model | analysis start (MET) | analysis end (MET) | f ux [photons · s ⁻¹ · cm ⁻²] | test statistics | expected counts | spectral index | |
|-----------------|-------------------------------|--|------------------------------------|---|-------------------------|---|--------------------------------|--|
| B2 2113+29 | pow2 | 2016-07-25@12:00:00 (491140803) | 2016-07-26@12:00:00 (491227203) | (42 ± 15) × 10 ⁻⁸ | 2.923 × 10 ³ | 2.388 × 10 ³ | (-214 ± 26) × 10 ⁻² | |
| | | [1.00 × 10 ² , 3.00 × 10 ²] MeV | | | | | | |
| | | total | | galactic | x/ galactic | f ux / f ux _{2FGL} ≈ 16 vs. 137 | | |
| | | test statistics | 2.923 × 10 ³ | 1.643 × 10 ² | 7.731 | [photons · s ⁻¹ · cm ⁻²] | | |
| photons f ux | (42 ± 15) × 10 ⁻⁸ | (629 ± 27) × 10 ⁻⁶ | (10 ± 4) × 10 ⁻⁵ | | | | | |
| expected counts | 2.388 × 10 ³ | 1.147 × 10 ² | 9.094 × 10 ¹ | | | | | |
| PKS 1510-08 | pow2 | 2016-07-25@12:00:00 (491140803) | 2016-07-26@12:00:00 (491227203) | (78 ± 19) × 10 ⁻⁸ | 6.806 × 10 ³ | 4.093 × 10 ³ | (-229 ± 21) × 10 ⁻² | |
| | | [1.00 × 10 ² , 3.00 × 10 ²] MeV | | | | | | |
| | | total | | galactic | x/ galactic | f ux / f ux _{2FGL} ≈ 1 vs. 4 | | |
| | | test statistics | 6.806 × 10 ³ | 1.335 × 10 ² | 1.701 × 10 ¹ | [photons · s ⁻¹ · cm ⁻²] | | |
| photons f ux | (78 ± 19) × 10 ⁻⁸ | (54 ± 7) × 10 ⁻⁵ | (19 ± 5) × 10 ⁻⁵ | | | | | |
| expected counts | 4.093 × 10 ³ | 3.658 × 10 ² | 1.726 × 10 ² | | | | | |
| 3C 454.3 | pow2 | 2016-07-25@12:00:00 (491140803) | 2016-07-26@12:00:00 (491227203) | (274 ± 18) × 10 ⁻⁸ | 4.288 × 10 ² | 1.454 × 10 ² | (-226 ± 6) × 10 ⁻² | |
| | | [1.00 × 10 ² , 3.00 × 10 ²] MeV | | | | | | |
| | | total | | galactic | x/ galactic | f ux / f ux _{2FGL} ≈ 1 vs. 17 | | |
| | | test statistics | 4.288 × 10 ² | 6.415 × 10 ¹ | 4.012 × 10 ¹ | [photons · s ⁻¹ · cm ⁻²] | | |
| photons f ux | (274 ± 18) × 10 ⁻⁸ | (45 ± 4) × 10 ⁻⁵ | (186 ± 17) × 10 ⁻⁶ | | | | | |
| expected counts | 1.454 × 10 ² | 1.758 × 10 ² | 1.636 × 10 ² | | | | | |
| PKS 1725+044 | pow2 | 2016-07-25@12:00:00 (491140803) | 2016-07-26@12:00:00 (491227203) | (11 ± 5) × 10 ⁻⁹ | 1.091 × 10 ¹ | 1.018 | (-2 ± 4) × 10 ⁻¹ | |
| | | [1.00 × 10 ² , 3.00 × 10 ²] MeV | | | | | | |
| | | total | | galactic | x/ galactic | f ux / f ux _{2FGL} ≈ 0 vs. 50 | | |
| | | test statistics | 1.091 × 10 ¹ | 7.258 × 10 ² | 3.539 | [photons · s ⁻¹ · cm ⁻²] | | |
| photons f ux | (11 ± 5) × 10 ⁻⁹ | (490 ± 11) × 10 ⁻⁶ | (89 ± 21) × 10 ⁻⁶ | | | | | |
| expected counts | 1.018 | 6.088 × 10 ² | 6.425 × 10 ² | | | | | |
| 4C +01.02 | pow2 | 2016-07-25@12:00:00 (491140803) | 2016-07-26@12:00:00 (491227203) | (160 ± 17) × 10 ⁻⁸ | 1.675 × 10 ² | 7.765 × 10 ¹ | (-246 ± 11) × 10 ⁻² | |
| | | [1.00 × 10 ² , 3.00 × 10 ²] MeV | | | | | | |
| | | total | | galactic | x/ galactic | f ux / f ux _{2FGL} ≈ 10 vs. 185 | | |
| | | test statistics | 1.675 × 10 ² | 1.023 × 10 ² | 9.835 | [photons · s ⁻¹ · cm ⁻²] | | |
| photons f ux | (160 ± 17) × 10 ⁻⁸ | (68 ± 5) × 10 ⁻⁵ | (105 ± 18) × 10 ⁻⁶ | | | | | |
| expected counts | 7.765 × 10 ¹ | 1.801 × 10 ² | 8.992 × 10 ¹ | | | | | |




Figure 4.5: An example of daily report produced by the "long-term monitor" analysis-pipeline.

The second analysis pipeline currently in place is the so-called "long-term monitor". This pipeline runs along the night and is intended to plan MAGIC observations on a longer time scale. The list of sources analyzed by this pipeline counts about 300 FSRQs and BLLacs chosen according to the scientific goals specified in the "Mother of ToO Proposal"; the list includes also fourteen gravitationally lensed blazars with measured delays between different images and/or already detected GeV emission.

Only about 100 sources are analyzed on a daily basis. In fact every day are analyzed only data relative to sources that have at least 10 hours of visibility in the

upcoming MAGIC observing period⁷. For the FSRQs in this list, we also compare the flux observed every day with the flux reported in the 2nd Fermi Gamma-ray LAT catalog of point sources (2FGL) [130]. If a source shows a flux that exceeds a certain threshold (in units of 2FGL-observed-flux) and/or shows a particularly hard spectral shape, this triggers a request for a ToO observation. The so called flux "alert-threshold" for each source has been calculated by [169] taking into account MAGIC sensitivity at 10 hours and EBL absorption⁸. Fig.4.5 shows the typical report that is automatically produced by the "*long-term monitor*" analysis-pipeline every day.

Since the purpose of this monitoring effort is to provide a real-time analysis, public Fermi-LAT data are automatically downloaded every four hours in order to keep our database updated.

Each source is analyzed using the Fermi Science Tools⁹ and especially the python package pyLike¹⁰. Currently the LAT event selection used for the analysis is the P8R2_SOURCE_V5 and the XML models for the likelihood analysis are produced using the 3FGL catalog [14]. The templates that we use to model the galactic and extra-galactic background are in agreement with the LAT collaboration prescriptions¹¹. Moreover, the pipeline has been promptly updated when a change in Fermi Science Tools and/or LAT instrument response function has been announced.

The first part of the analysis is devoted to select photons in space, time and energy:

- only data inside a Region of Interest (ROI) of 15 degrees around the known source position are analyzed;
- a cut to discard earth-limb contamination is applied;
- the selected energy range is, usually, 100 MeV - 500 GeV;
- time intervals when the data quality is not classified as 'Good' are finally excluded.

All these cuts are performed using the tools `gtselect` and `gtmktime`.

During the very first step, a list of photons with energy ≥ 10 GeV and having a distance ≤ 0.7 deg (which is roughly the 95% containment of LAT 'BACK' PSF at 10 GeV) is saved in a dedicated text file.

⁷MAGIC observations are planned and divided into periods that follow the moon phases; data taking is not possible during full moon.

⁸ $z = 0.9$ is assumed for unknown- z sources

⁹Current version: ScienceTools-v10r0p5-fssc-20150518

¹⁰See http://fermi.gsfc.nasa.gov/ssc/data/analysis/scitools/python_tutorial.html for details.

¹¹<http://fermi.gsfc.nasa.gov/ssc/data/access/lat/BackgroundModels.html>

The second part of the analysis consists in the calculation of exposure maps to see the amount of time the LAT spent observing the selected region of interest. This is done through the tools `gtl1cube` and `gtexpmap`. Details about this step can be found at the "Livetime and Exposure" web-page at FSSC ¹².

The last part is the likelihood analysis itself where the probability of obtain the observed data given an input model is calculated.

A detailed description of all these analysis steps can be found at the web-page "Unbinned Likelihood Tutorial"¹³.

On request, each analysis can be easily performed also in other two energy ranges to better monitor the low-energy versus the high-energy activity of some specific sources. This is justified by the fact that the energy threshold of interest for VHE possible follow-up observations is usually 1 GeV or 10 GeV (see e.g. Fig.4.15).

When the TS found at the end exceed the value of 25 ($\sim 5\sigma$ detection) the results are automatically sent by e-mail to the Fermi/MAGIC Udine/Trieste working group (the "shifters") and added by-default to a report. When all daily analyses have been completed and quickly checked by a human-in-the-loop, the report is then circulated within the MAGIC collaboration. The information about high-energy photons detected is also included in the same report.

For each source, if the analysis results fulfill the criterium of having a detection significance greater than ~ 9 sigma or if more than two hard photons are detected inside the PSF or finally if there is at least one photon with energy ≥ 50 GeV, an SED is automatically produced in five logarithmically spaced energy bins from 100 MeV to 500 GeV. In order to not delay the arrival of the final report, this step starts only when likelihood analyses relative to all the sources are successfully completed. The plots showing the SED and the TS values in each energy bin (see e.g. Fig.4.6) are then automatically added as attachments to another e-mail promptly sent to the the "shifters" and then eventually circulated in the MAGIC collaboration on request: the plots are particularly useful for people involved in the process of scheduling the night-by-night observations (e.g. the scheduler in charge, working-group conveners, PI of specific sources, ..)

If the detection of the source is instead not significant, a $2\text{-}\sigma$ upper-limit is then calculated.

Results: MAGIC detections and scientific outcome

All results obtained using the both the "Fermi-weather" and the "Long-term monitor" analysis pipelines are stored in text files and in a MySQL database respectively.

¹²http://fermi.gsfc.nasa.gov/ssc/data/analysis/documentation/Cicerone/Cicerone_Data_Exploration/livetime_a

¹³http://fermi.gsfc.nasa.gov/ssc/data/analysis/scitools/likelihood_tutorial.html

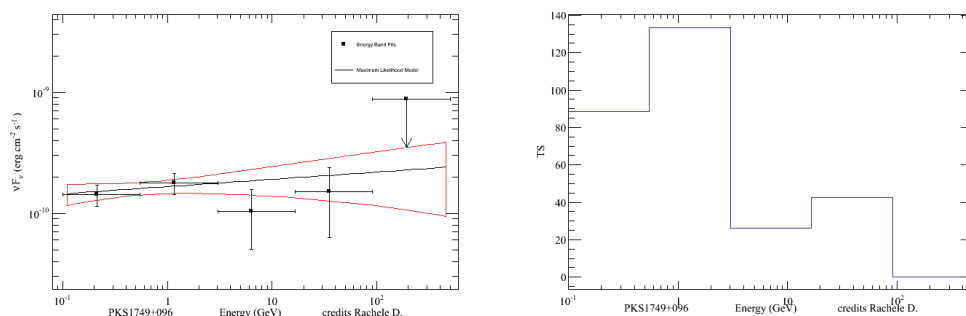


Figure 4.6: An example of plots produced automatically by the "Fermi-Weather" analysis pipeline when the results fulfill the criteria for the SED computation. These specific plots have been produced on 2016 July 24 and refers to the source PKS 1749+096. Similar results, together with the high-flux and hard state were announced also via ATel by Swift and Fermi (#9620) and triggered a MAGIC ToO observation: PKS 1749+096 (aka OT 081 or 4C +09.57) was significantly detected by MAGIC during the subsequent night. The detection of this source, observed at VHE for the first time, was then announced via ATel (#9267).

The stored results can be then used to produce useful plots to keep track of the "historical behavior" of each source in order to "tune" the MAGIC response to an alert and to help in the scheduling process.

Fig.4.7 shows for example the light-curve, spectral index vs spectral shape and histogram of flux, TS values and number of predicted counts for the source 3C 454.3. It is a powerful distant blazar at redshift $z=0.859$ showing high activity in HE/Fermi energy range (see e.g. [53, 48]). It has been observed by MAGIC several times but there is no evidence of TeV emission so far. Our monitoring suggests that, even when the >100 MeV analysis gives a hard spectral index, the SED (Fig.4.8) shows the evidence for a spectral cut-off at ~ 10 GeV. For other details on our collected results about this source see also Fig.4.9 and 4.11.

Fig.4.9 and 4.10 show a summary of results from the "long-term monitor" analysis pipeline. While the total number of sources analyzed is ~ 300 , only 81 sources have been significantly detected ($TS \geq 25$) at least once from March 2014 up to August 2016. Each of these sources has been analyzed about 527 times¹⁴. I show in white the number of significant detections while in shades of blue the number of times for which the measured flux exceeded a certain value. In particular the

¹⁴This is a mean value; each source is analyzed or not according to the visibility criteria cited above.

blue color indicates the number of times when the flux exceeded the above cited "alert-threshold" (F_{th}) [169]. These plots show clearly the diversity of behaviors associated to flaring AGNs that reflects the physical differences among the sources. Some sources are frequently quite bright in gamma-rays but never/rarely reached the "alert-threshold" (see e.g. 3C 454.3, 4C +01.02, 3C 279); some other sources are rarely significantly detected but, when it happens, show a flux that is close to F_{th} (e.g. PMN J2345-1555, S4 0110+49, 4C +21.35) and finally some sources show an intermediate behavior (e.g. PKS 1510-08, TON 599, PKS1441+25). Note also that the majority of these sources are faint and rarely reach the alert criteria. In this context, it is particularly useful having an automated analysis pipeline that runs over a large number of sources of interest in order to maximize the chance to catch a somehow not-expected flare.

Fig. 4.11, 4.12 and 4.13 show the flux values versus the spectral index distribution for some selected sources. Yellow/red dots also indicate the detection of photons with energy ≥ 10 GeV consistent with the position of our source of interest¹⁵. Again the diversity of behavior associated to various sources is quite clear. Some sources as 3C 454.3 and PKS 1510-08 show a broad distribution of flux values with the first never reaching the alert threshold even when the LAT detected some hard photons; PKS 1441+25 and 3C 279 have instead a narrow distribution of flux values even if the spectral indexes cover a wide range of values.

From March 2013 up to now, our analyses helped in the scheduling of about fifty ToO observations; about 15 of them triggered only by our results.

It is important to stress that, even when the first alert about source in high-state does not come from our analysis but from other multiwavelength facilities, we promptly provide important feedback on the evolution of the high-energy flux and hardness of the source in order to properly plan the upcoming observations. This is particularly useful since it happens that full moon, weather conditions, other already planned maintenance and test operations, can sometimes delay the MAGIC observation of the source of interest.

Note also that all plots showed in this chapter can be easily obtained on-request for each source in our database using a set of ready-to-go python-Matplotlib¹⁶ scripts.

Using the analysis pipelines described above we actively contributed to multi-wavelength observational campaigns that followed and/or led to the discovery of HE and VHE emission from various interesting AGNs, e.g.:

- the gravitationally lensed blazar QSO B0218+357: this kind of sources can be used for testing the achromaticity of gravitational lensing at sub-TeV energies while to study the delay between individual images and changes in the flux

¹⁵Distance $\lesssim 0.7$ deg i.e. roughly the 95% containment of LAT 'BACK' PSF at 10 GeV.

¹⁶<http://matplotlib.org/> [97]

ratio of the two images can be used to strongly constrain the location, size and velocity of emission region (see also Fig.4.14 and 4.13);

- the very distant FSRQ PKS 1441+25 ($z=0.9397$): the VHE spectrum observed during the highest activity seen in the LAT energy range in April 2015 has been used to probe the EBL at an unprecedented distance scale for ground-based gamma-ray observatories [27];
- PG 1553+113: this source interestingly shows evidence for quasi-periodic modulation in the flux [20]; the origin of the modulation is still debated and multiwavelength coordinated observations are useful to finally shed light on the physical processes in action in the region nearby the central black-hole (see also Fig. 4.15);
- the recently MAGIC discovered blazars: PKS 1749+096 (ATel (#9267), Fig. 4.6), 1ES 1959+650 (ATel#9010), S2 0109+22 (ATel #7844) and S4 0954+65 (ATel#7080).

This last source (having $z=0.368$) underwent to an exceptionally bright flare in LAT energy range ($E > 100$ MeV) in February 2015; we showed in [170] that such a flaring blazar showing flux of $\gtrsim 1.0 \times 10^{-6}$ photons $\text{cm}^{-2} \text{s}^{-1}$ and a hard spectral index (< 2.0) detected by Fermi-LAT on daily timescales is a promising target for follow-up by ground-based TeV telescopes to discover high-redshift blazars. In fact it allows to investigate their temporal variability and spectral features in the VHE band, and also constrain the intensity of the EBL.

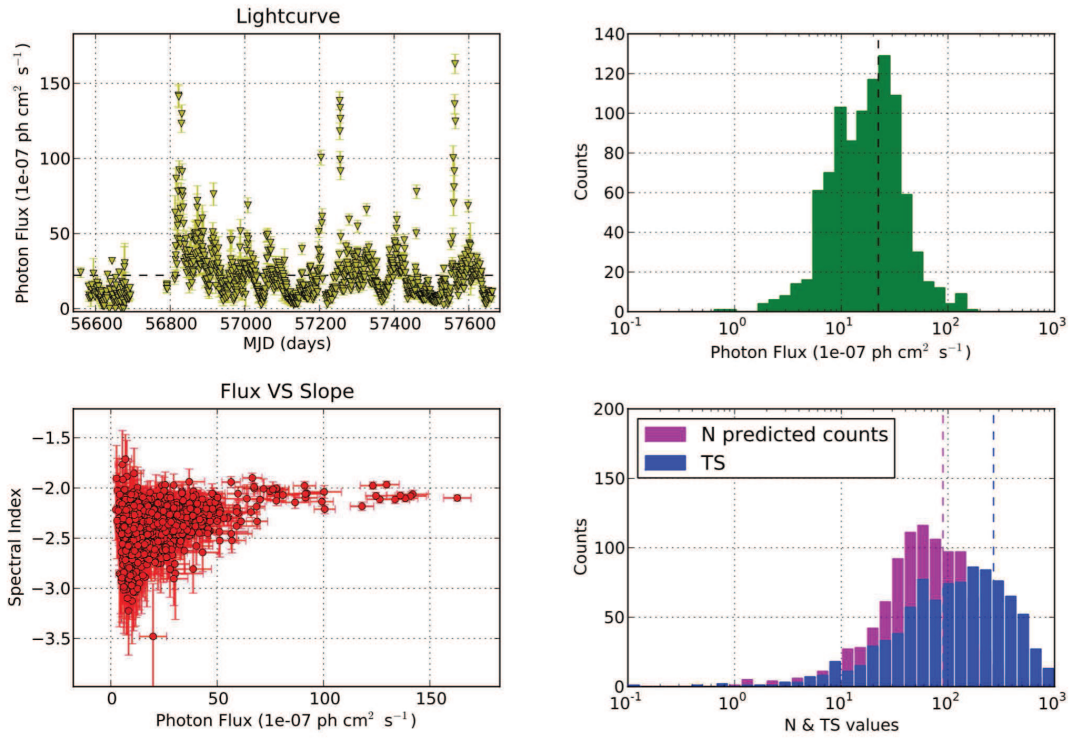


Figure 4.7: Light-curve, spectral index vs spectral shape and histogram of flux, TS values and number of predicted counts for the blazar 3C 454.3 as measured by the "Fermi-weather" analysis pipeline; the dashed lines indicate the measured mean values.

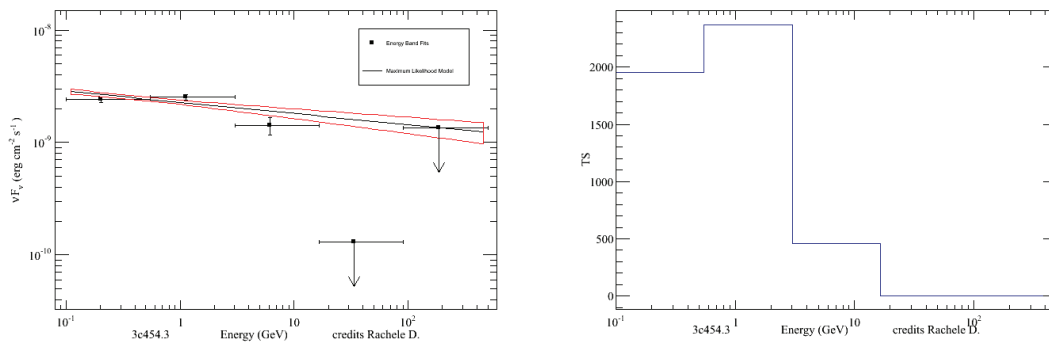


Figure 4.8: 3C 454.3: SED and TS distribution in energy bins automatically produced on 2016 June 23-24. The source was showing a hard spectrum in the full $E \geq 100$ MeV energy range and four photons with energies between 10 and 15 GeV were detected. Despite this the SED showed a spectral cut-off at ~ 10 GeV. This kind of information is useful to help in the scheduler process when more than one source, competing for the same observing time, show some kind of activity in other wavelengths.

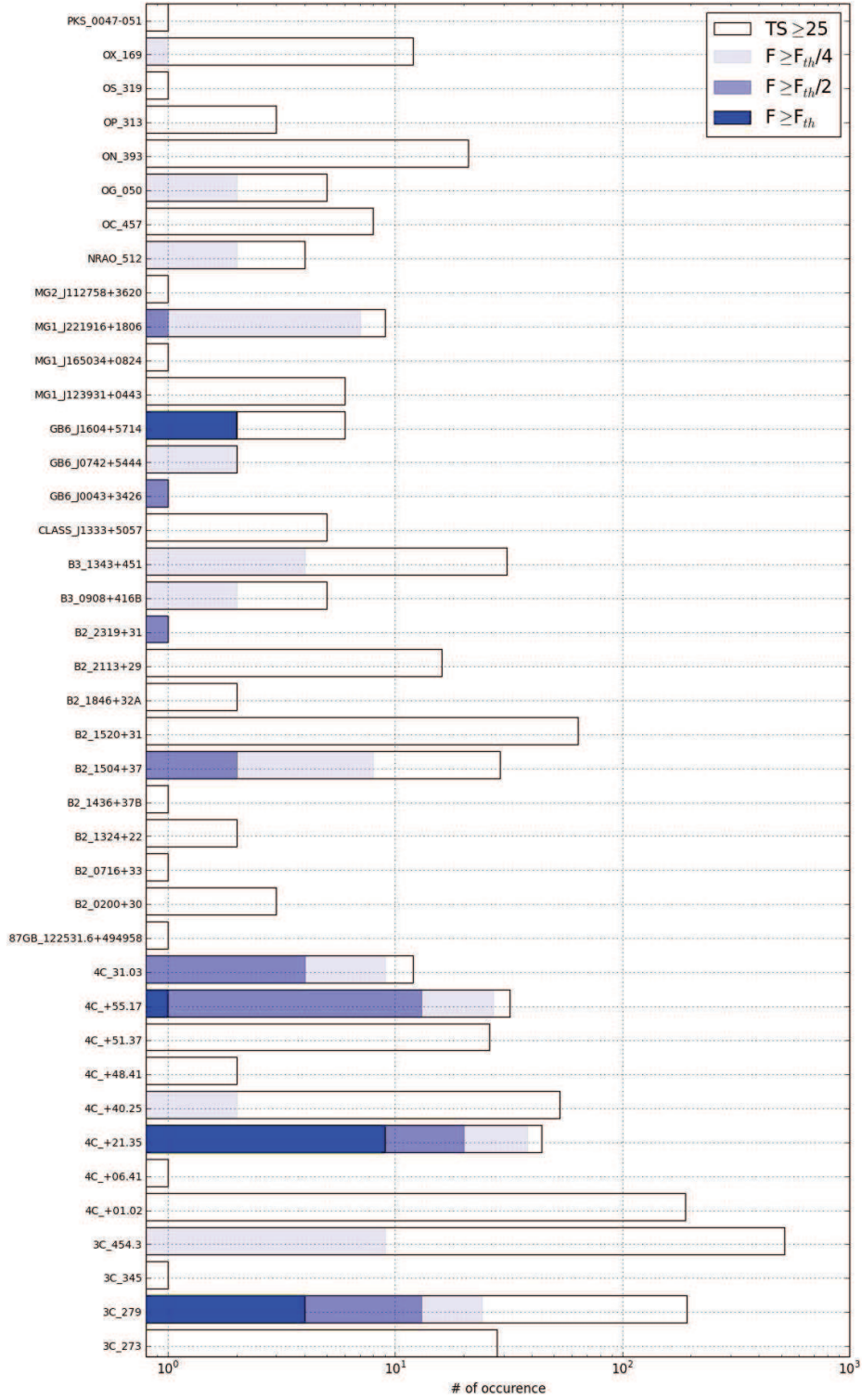


Figure 4.9: To be continued in next figure.

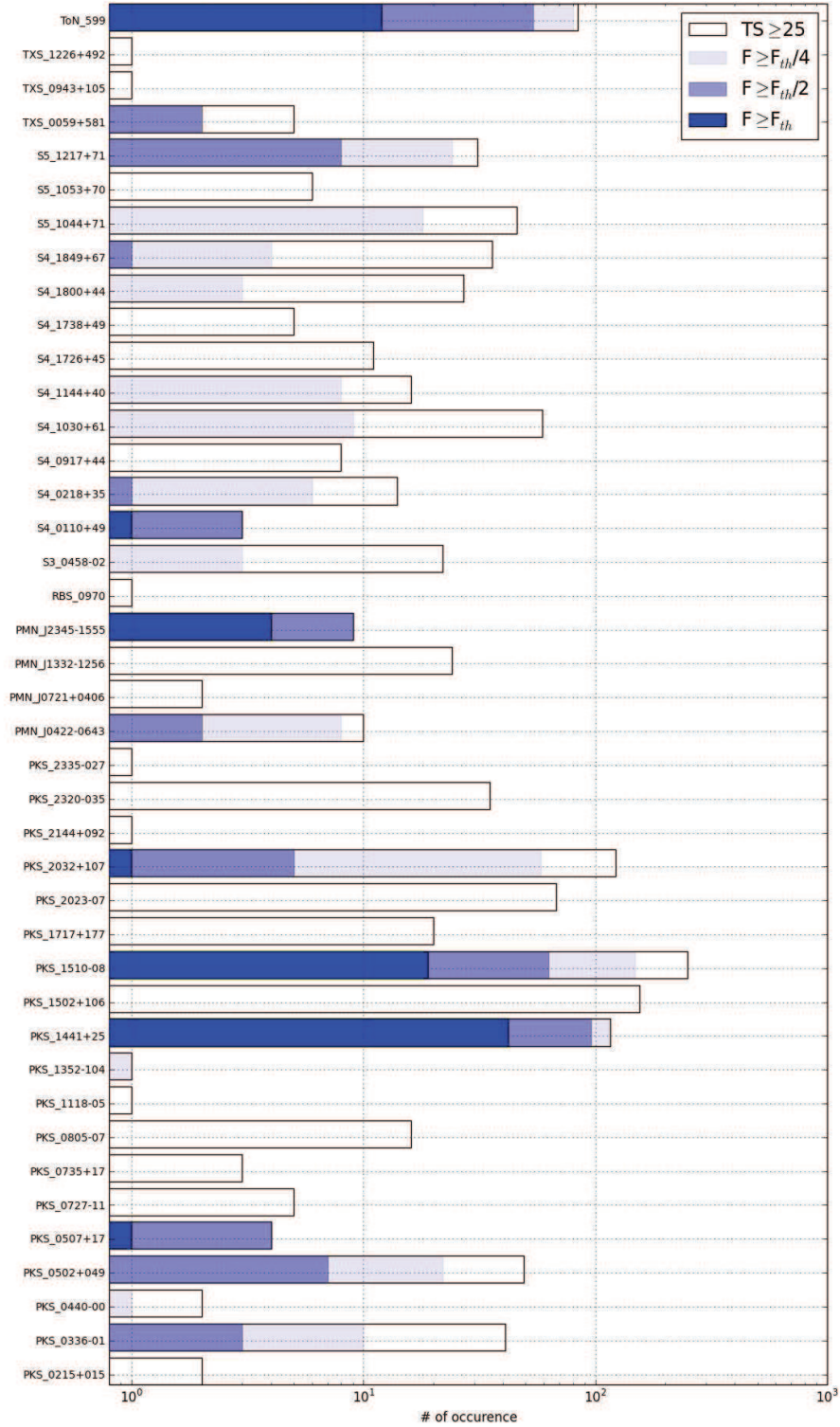


Figure 4.10: For each source that has been significantly detected ($TS \geq 25$) at least once I report the number of times that the flux measured was above the alert threshold (blue) or above a fraction of that alert value (shades of blue); the total number of significant detection has been reported in white. Note that each of these sources has been analyzed about 520 times, on average, on a daily time scale from March 2014 to August 2016 according to visibility criteria explained in the text.

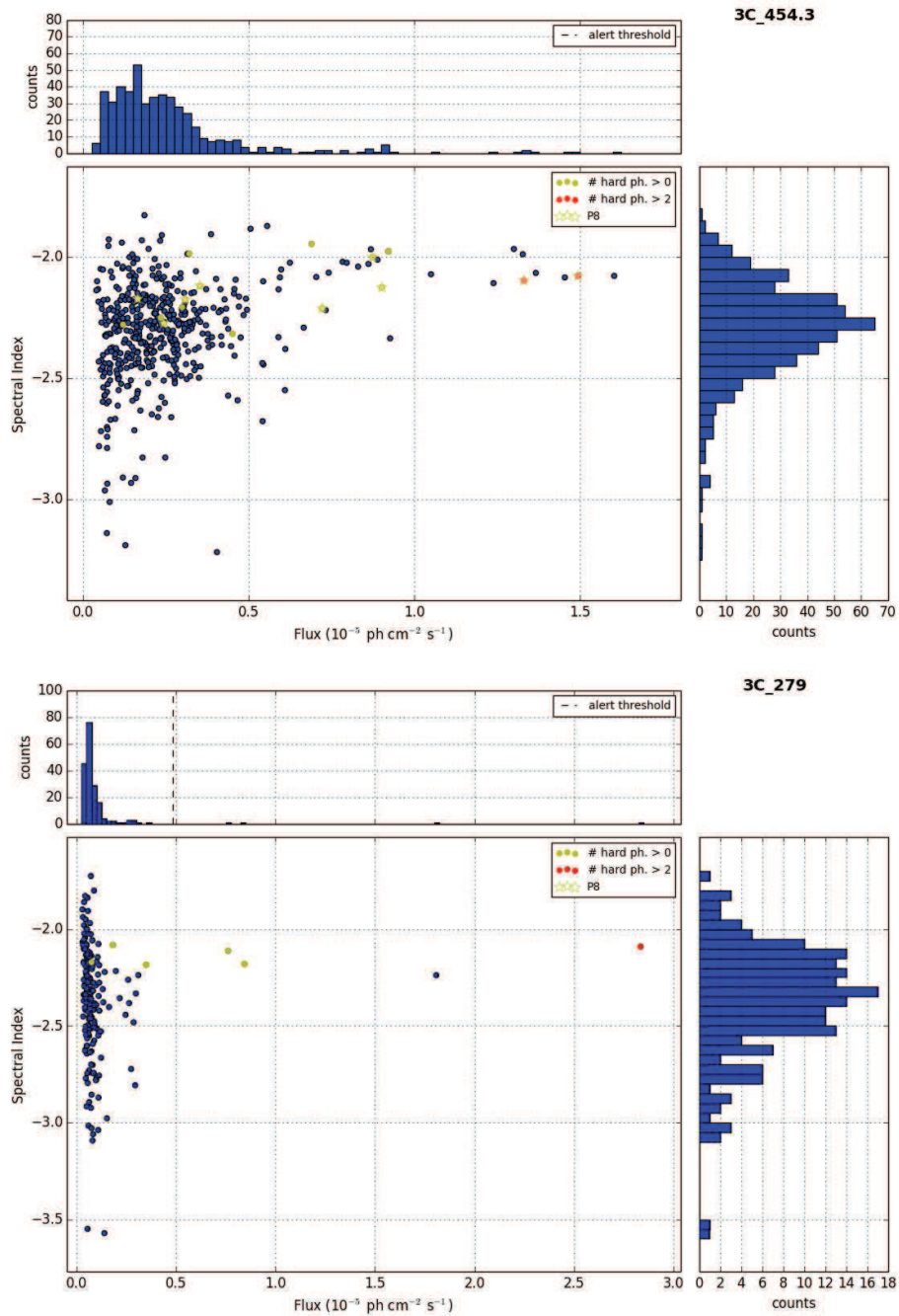


Figure 4.11: Photon flux and spectral index for the blazar 3C 454.3 (top panel) and 3C 279 (bottom panel) as observed by the LAT during the "long-term monitor" observing period (Mar 2014 - Aug 2016) when the source fulfilled the observing criteria. When showed, the black dashed line indicates the alert threshold flux; the yellow and/or red dots indicate the detection of hard (≥ 10 GeV) photons at a position consistent with the source of interest (i.e. inside the LAT BACK PSF).

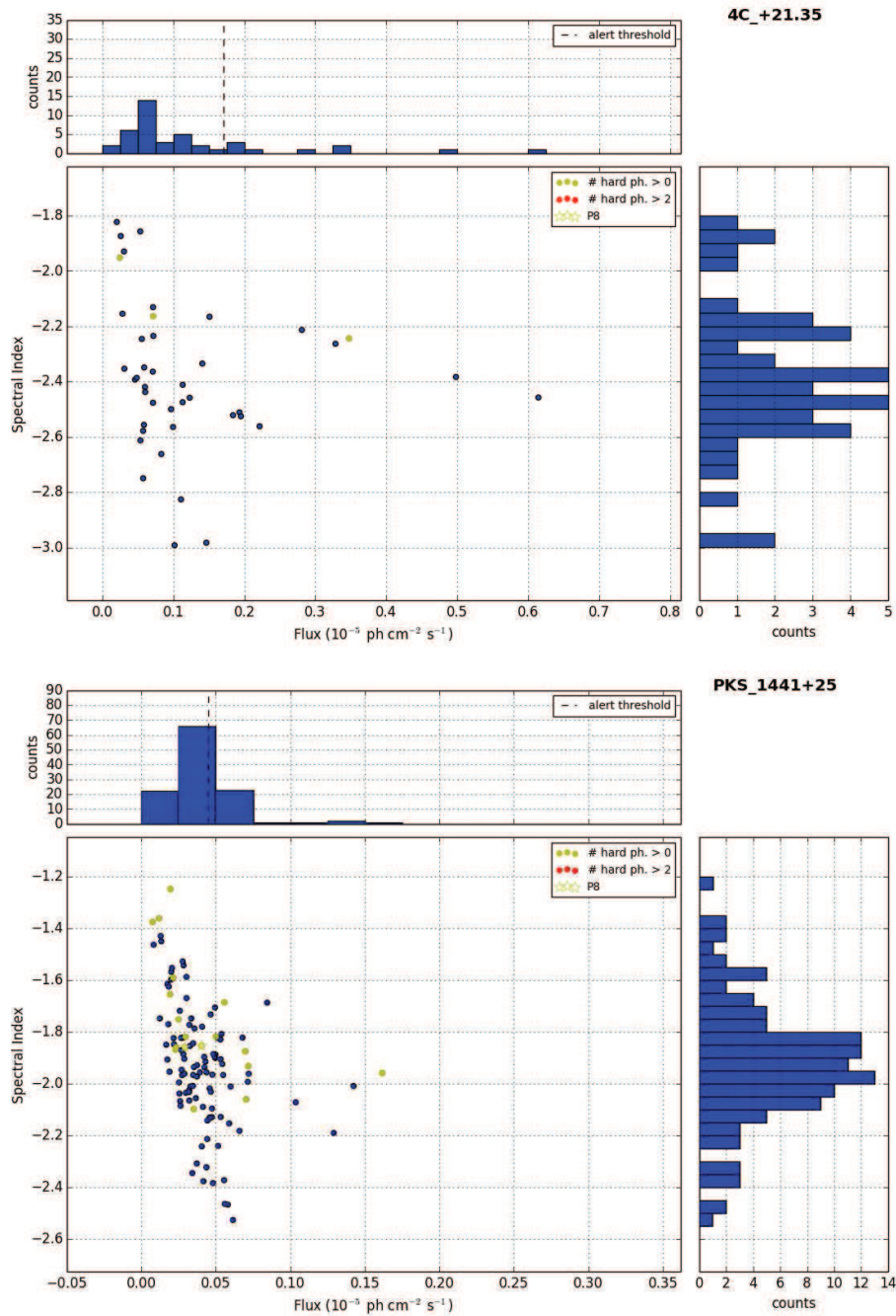


Figure 4.12: Photon flux and spectral index for the blazar 4C +21.35 (top panel) and PKS 1441+25 (bottom panel) as observed by the LAT during the "long-term monitor" observing period (Mar 2014 - Aug 2016) when the source fulfilled the observing criteria. When showed, the black dashed line indicates the alert threshold flux; the yellow and/or red dots indicate the detection of hard (≥ 10 GeV) photons at a position consistent with the source of interest (i.e. inside the LAT BACK PSF).

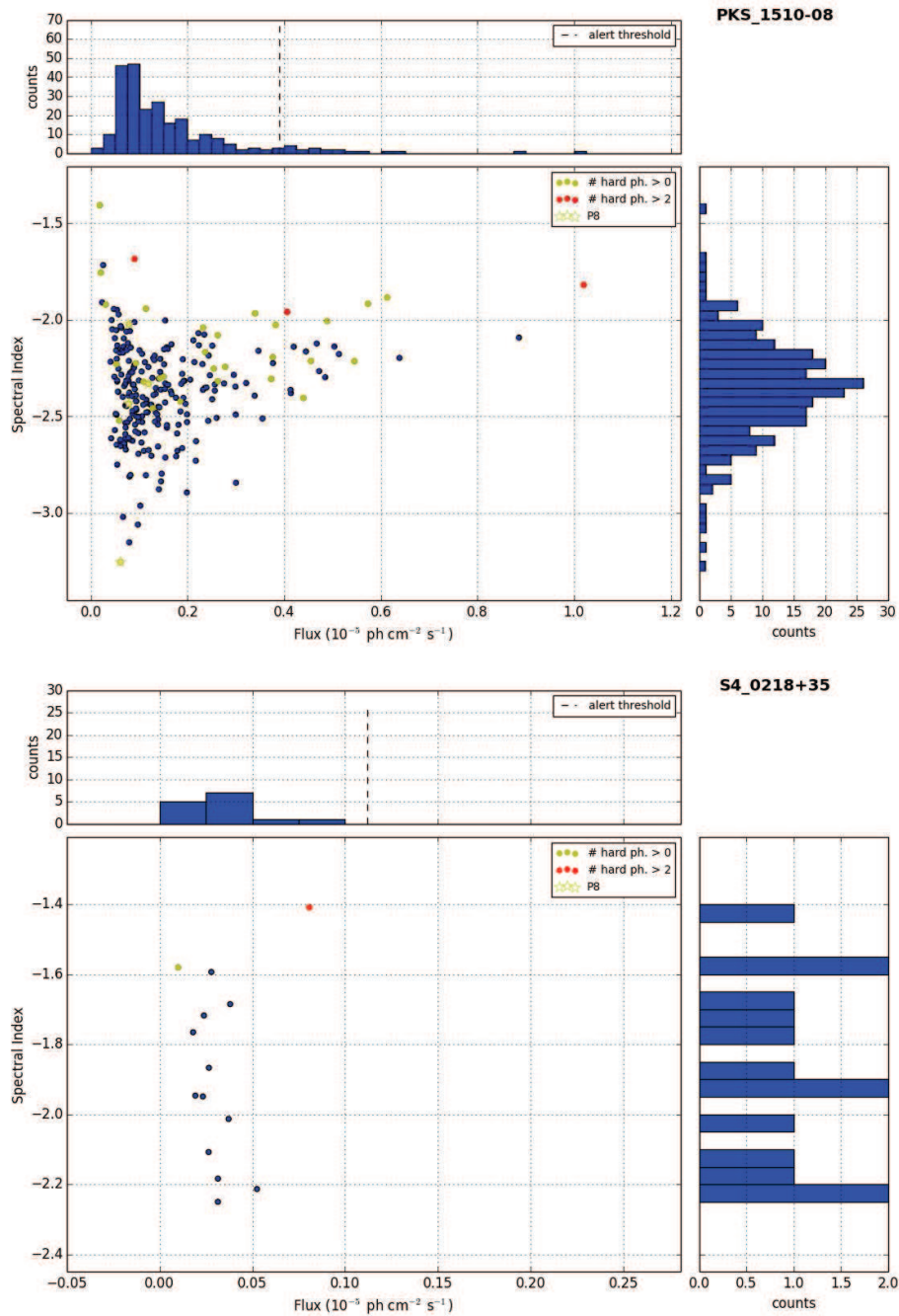


Figure 4.13: Photon flux and spectral index for the blazar PKS 1510-089 and S4 0218+35 (aka QSO B0218+357) as observed by the LAT during the "long-term monitor" observing period (Mar 2014 - Aug 2016) when the source fulfilled the observing criteria. When showed, the black dashed line indicates the alert threshold flux; the yellow and/or red dots indicate the detection of hard (≥ 10 GeV) photons at a position consistent with the source of interest (i.e. inside the LAT BACK PSF).

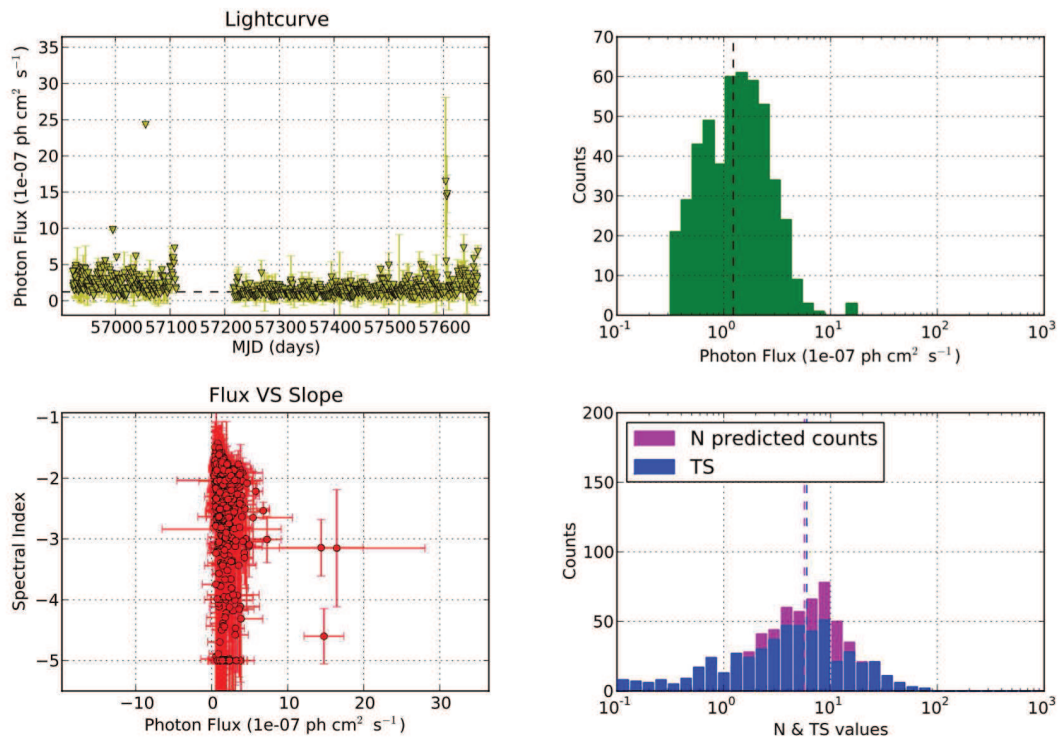


Figure 4.14: Light-curve, spectral index vs spectral shape and histogram of flux, TS values and number of predicted counts for the gravitationally lensed blazar QSO B0218+357 (aka S4 0218+35) as measured by the "Fermi-weather" analysis pipeline; the dashed lines indicate the measured mean values.

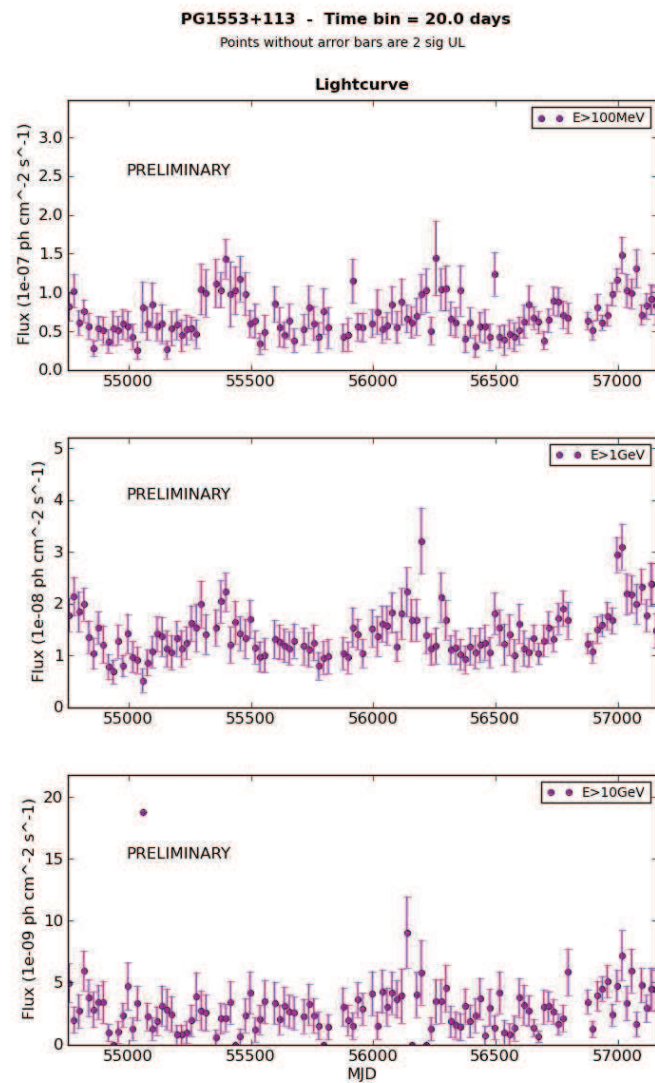


Figure 4.15: PG1553+113: observed 20-days binned light-curve for in three different energy ranges (from top to bottom panel, $E_{\text{min}}=100 \text{ MeV}$, 1 GeV , 10 GeV); this kind of analysis is useful to monitor the behavior of the high-energy flux compared to the full $>100 \text{ MeV}$ emission.

Chapter 5

Novae

When a white dwarf is the primary component of a semi-detached binary stellar system, the result may be a classical nova, a recurrent-symbiotic nova, a dwarf nova or a Type I supernova. All these phenomena involve mass transfer from one component to the other and subsequent explosions that can lead, in the latter case, also to the complete destruction of the white dwarf. The term *nova*, from Latin "new", derives from the fact that all these types of outbursts, that actually involve very different mechanisms, are related to transient phenomena of increased brightness visible to the naked eye that appeared as new stars in the sky.

Novae are thermonuclear explosions triggered on the surfaces of white dwarf stars due to mass accretion from the companion in a binary system [103].

Classical novae belong to the class of Cataclysmic Variables. These systems are typically small, at average roughly the size of the Earth-Moon system, have short orbital periods (1-10 h) and contain white dwarf components together with cool M-type secondaries that fill their Roche lobes. They provide valuable information on the final stages of stellar evolution and are also important for studying accretion disk evolution properties.

Recurrent novae belongs instead to the class of Symbiotic Binaries. These are long-period (typically range between 200 and 1500 days) interacting binaries consisting of an M giant (sometimes a pulsating Mira-type variable) and a accreting component that can be a white dwarf or a sub-dwarf or a low-mass main-sequence star ($M \lesssim 1.1 M_{\odot}$). The common feature of these systems is that accretion occurs through the wind of the cool component onto its hot companion. Generally speaking, symbiotic stars are like overgrown cataclysmic variables, but with less violent eruptions.

Recurrent novae are very rare in fact only ten are currently known [161]. Classical novae are instead very common: the rate of Galactic novae is highly uncertain, but a range of ~ 20 -50 per year can be considered plausible [164].

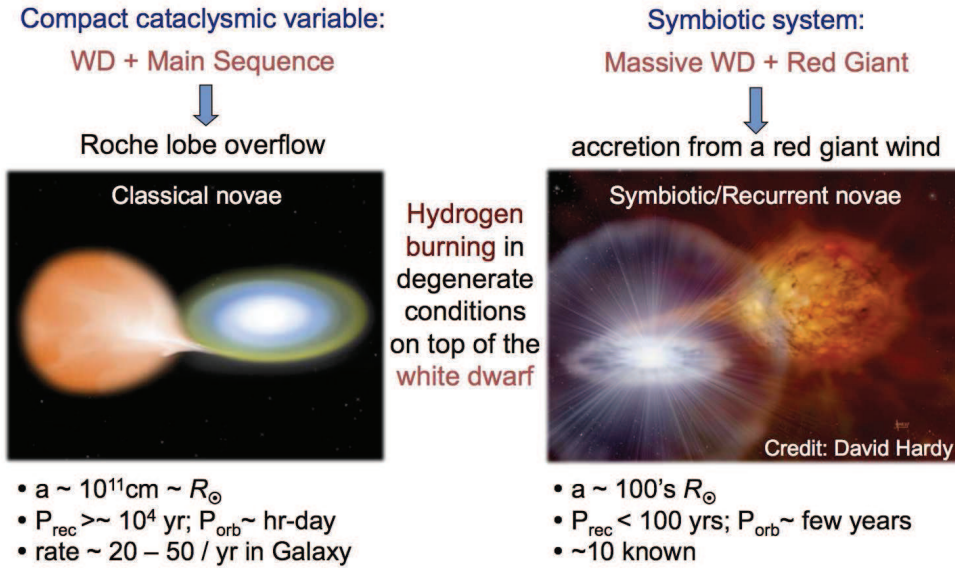


Figure 5.1: Schematic view and summary of characteristics of classical and symbiotic binary systems (adapted from [90] and [54]).

5.1 Fermi-LAT observations of novae

In March 2010, the LAT serendipitously discovered variable γ -ray (0.1-10 GeV) emission from the optical detected nova of the symbiotic star V407 Cygni (V407 Cyg) [10]. After that, other five classical novae were detected from the LAT from 2012 to 2015 at energies $> 100 \text{ MeV}$ with significances comprised between $10\text{-}20\sigma$. These are: V959 Monocerotis 2012 (V959 Mon), V1324 Scorpii 2012 (V1324 Sco), V339 Delphini 2013 (V339 Del), V1369 Centauri 2013 and V5668 Sagittarii 2015 No.2 [23] [55].

When a nova explodes in a symbiotic binary system, the ejecta from the white dwarf surface expand within the circumstellar wind of the red giant companion and high-energy particles can be accelerated in a blast wave driven in the high-density environment so that variable γ -ray emission can be produced. In a classical nova, by contrast, the ejecta quickly expand beyond the confines of the compact binary into a much lower density environment. High-energy particle acceleration could therefore be related to a bow shock driven by the ejecta in the interstellar medium, or to turbulence and eventually weaker internal shocks formed in the inhomogeneous ejecta itself.

It's important to note that even LAT-detected classical novae show different

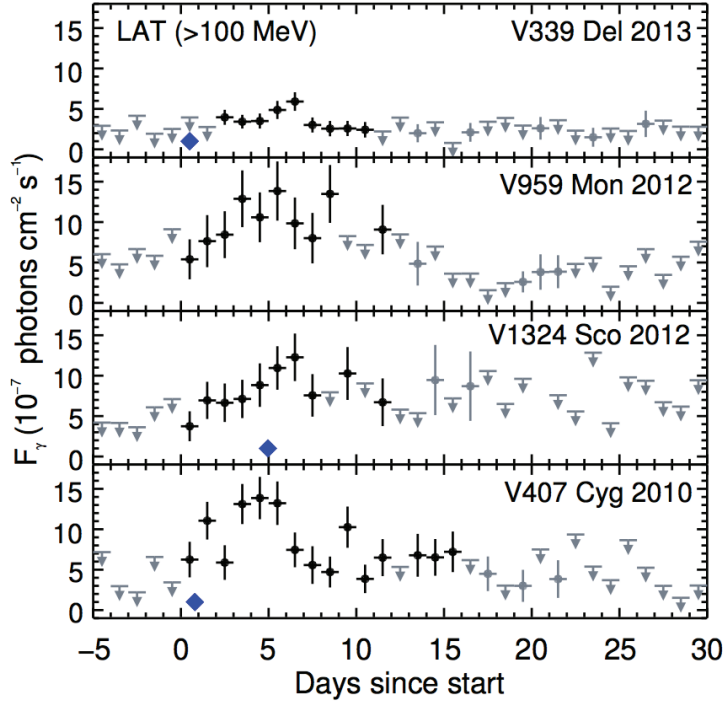


Figure 5.2: Fermi-LAT 1-day binned light curves of the first four γ -ray detected novae. Vertical bars indicate 1σ uncertainties for data points with significance $> 3\sigma$ (black) and $2-3\sigma$ (gray); otherwise, 2σ upper limits are indicated with gray arrows. Start times (from top to bottom panels: 2013 August 16, 2012 June 19, 2012 June 15, and 2010 March 10) were defined as the day of the first γ -ray detection. Blue diamonds indicate the epoch of the optical peak [23].

optical/ultraviolet properties; for example, V959 Mon has been identified as an explosion from an oxygen-neon (ONe) nova, while V1324 Sco and V339 Del appear to be carbon-oxygen (CO) novae.

Despite these differences, the observed γ -ray light curves (Fig.5.2) for the first four well studied novae (detailed analysis can be found in [23]) appear similar, being brighter initially with most of the emission observed within 2 weeks, and total detected durations of 17-27 days.

The peak phase lasts for 2-3 days occurring 3-5 days after the initial LAT detections. The observed optical peak preceded the γ -ray peak by 2 days in V1324 Sco and 6 days in V339 Del. V959 Mon was discovered first by Fermi-LAT and identified as a γ -ray transient in the Galactic plane while close to the Sun; it was then identified as a nova 2 months later following its optical detection so that a

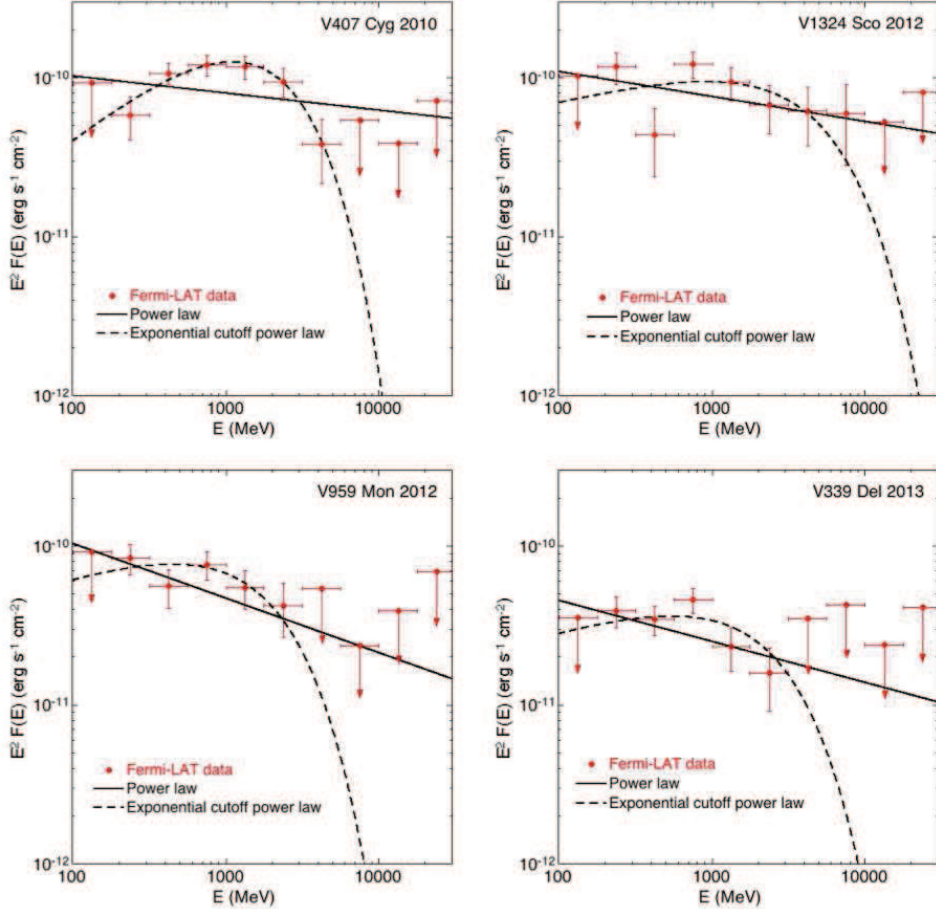


Figure 5.3: Fermi-LAT spectra of the four novae over the full durations. Vertical bars indicate 1σ uncertainties for data points with significances $> 2\sigma$; arrows indicate 2σ upper-limits [23].

comparison of the optical and γ -ray peak is not possible. Because the early optical light variations of the ejecta in novae are driven by line opacity changes in the ultraviolet during the expansion, the rise to peak optical brightness coincides with the maximum flux redistribution toward lower energies as the optically thick surface moves outward. The initial lack of detected γ -rays could be caused by the fact that the ejecta are opaque and > 100 MeV emission produced is absorbed via photon-atom interactions, with γ -rays appearing at later times when the density drops and the ejecta become transparent. The γ -ray detection occurred during a time of high X-ray and ultraviolet/optical opacity. A few days' delay of the γ -ray

peak relative to the optical peak was observed in V407 Cyg too but this may be related to interactions with its red giant companion [23].

The observed > 100 MeV spectra of the four novae are also similar. A curved spectral shape (power-law with high-energy exponential cut-off) is preferred over a simple power-law with $2-4\sigma$ improvement. Fig.5.3 shows the broad spectral peaks that cutoff at energies 1-4 GeV; power-law indices are in the range 1.2-1.8 with the classical novae having softer spectral indices respect to V407 Cyg. Significant emission is observed up to 6-10 GeV (V1324 Sco). In order to check whether the spectral characteristics changed during the γ -ray flares, data sets for each nova was split into two time intervals (a 6 days a phase of stronger activity followed by a 21 days decaying phase): no spectral variability has been significantly detected.

Gamma-ray emission mechanisms involve interactions of the accelerated high-energy protons (hadronic scenario) or electrons (leptonic scenario) within the ejecta. In the hadronic scenario, high-energy protons that interact with nuclei produce neutral pions decaying into two γ -rays. In the leptonic case, accelerated electrons produce γ -rays through a combination of inverse Compton scattering with low-energy photons and bremsstrahlung with atoms in the vicinity of the nova. Spectral fits with hadronic and leptonic models were statistically indistinguishable because of the poorly constrained spectral slopes.

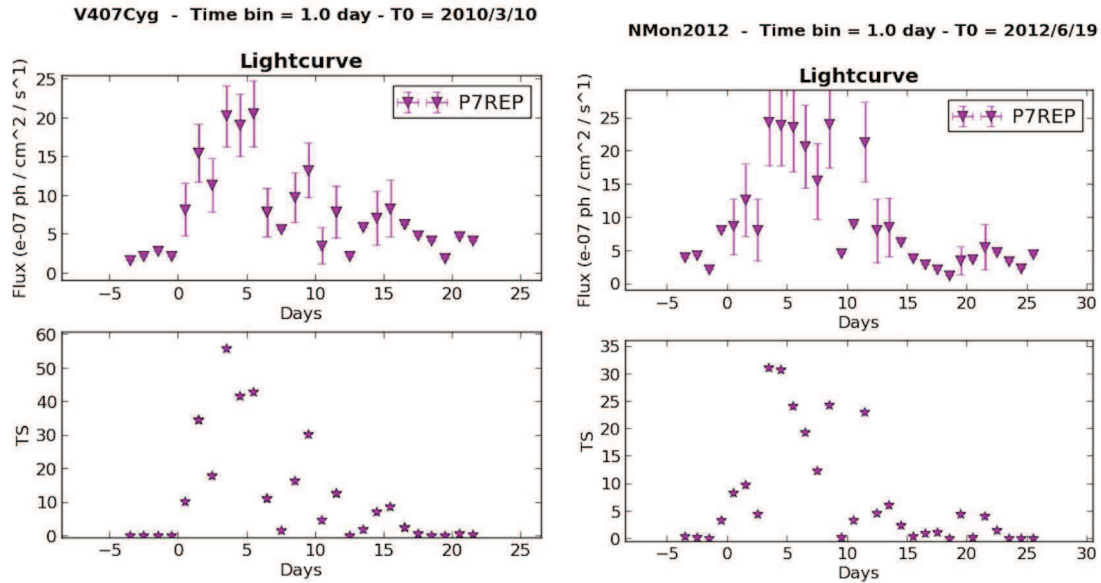


Figure 5.4: Light-curve and TS evolution for V1369 Cyg and V959 Mon (on the left and on the right respectively).

The results discussed until now were obtained using P7 data [23]. Before the

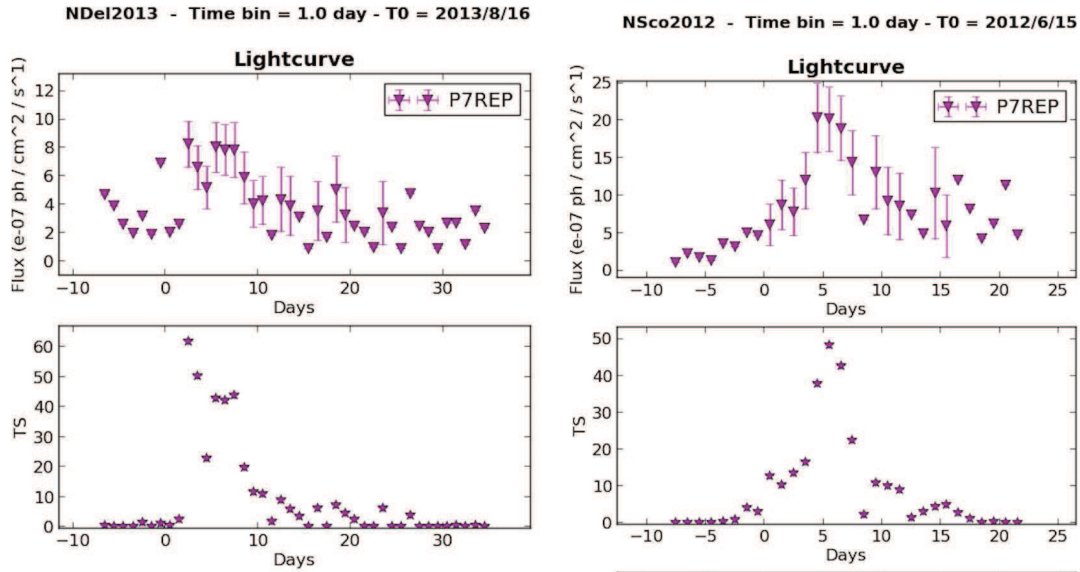


Figure 5.5: Light-curve and TS evolution for V339 Del and V1324 Sco (on the left and on the right respectively).

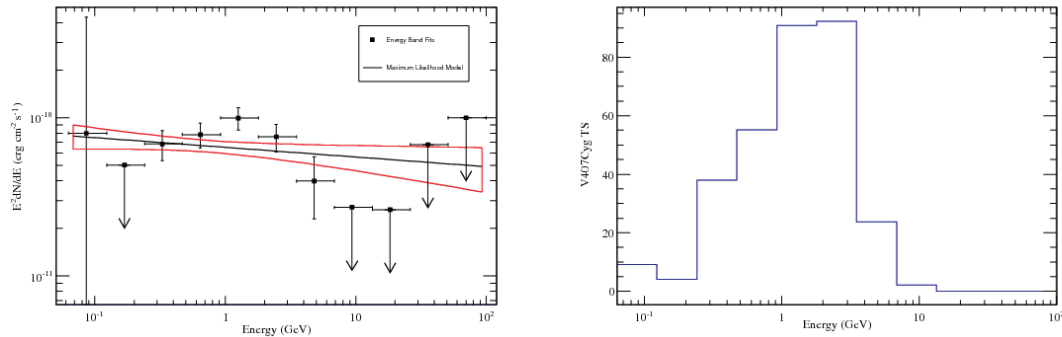


Figure 5.6: V1369 Cyg: spectral energy distribution and TS values extracted in 11 logarithmically spaced bins from 70 MeV to 100 GeV.

above paper was published, I carefully checked light-curves and spectra in order to be sure that the conclusions about the duration and the origin of the observed emission remain unchanged when using the more recent P7Rep event selection (see Fig.5.4, 5.5, 5.6, 5.7, 5.8, 5.9).

We recently reported the observation of other two classical novae, V1369 Cen and V5688 Sgr , detected by the LAT in 2013 and 2015 respectively [56]. These two

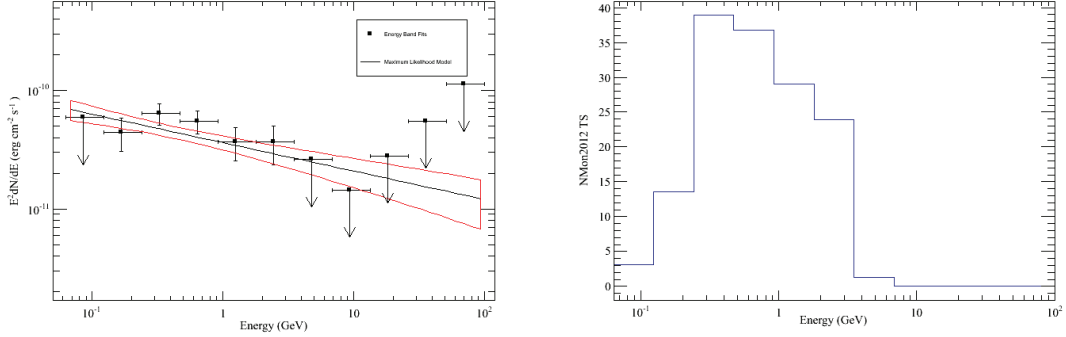


Figure 5.7: V959 Mon: spectral energy distribution and TS values extracted in 11 logarithmically spaced bins from 70 MeV to 100 GeV.

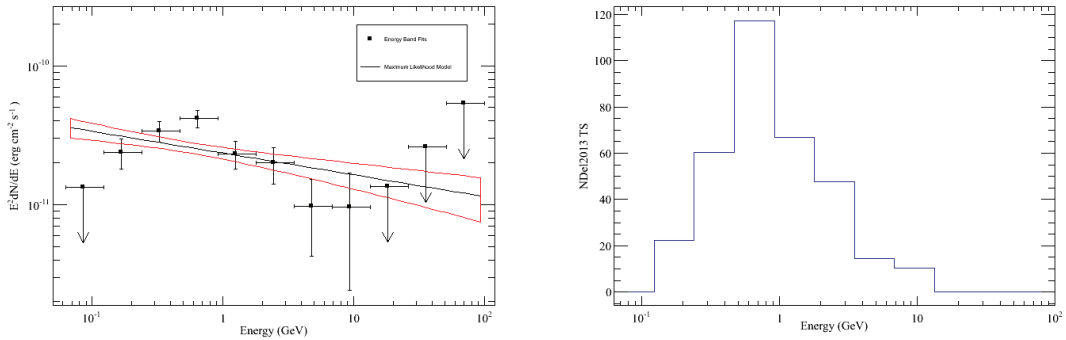


Figure 5.8: V339 Del: spectral energy distribution and TS values extracted in 11 logarithmically spaced bins from 70 MeV to 100 GeV.

novae were detected thanks to ToO observations triggered by the optical discovery and the onset of LAT emission is ~ 2 days after their respective first optical peak. The increased exposure achieved thanks to the ToO (approximately twice that of the nominal sky survey) was crucial for the gamma-ray detection since these sources are found to be intrinsically fainter than others previously detected.

The spectral characteristics are found to be in agreement with others while the light curves show that the emission lasted longer ($\sim 1.5 - 2$ months). However, since the respective cumulative significance of V1369 Cen and of V5668 Sgr is lower than the previous cases, it is difficult to derive good constraints on the curvature of the spectra and on temporal variations.

Since the γ -ray properties of the novae detected so far by the LAT are similar

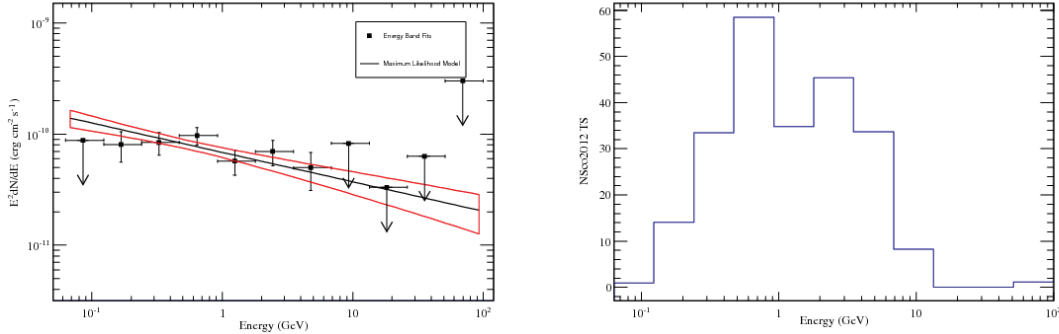


Figure 5.9: V1324 Sco: spectral energy distribution and TS values extracted in 11 logarithmically spaced bins from 70 MeV to 100 GeV.

and their underlying properties are unremarkable, it appears that all novae can be considered to be candidate γ -ray emitters. Their detection may imply close proximity, in fact all the LAT-detected novae have estimated distances of less than 4-5 kpc. So far, the γ -ray detection rate of novae is about one per year; this is consistent with the lower end of a plausible extrapolation of 1-4 nova occurring per year at distances comparable with those of LAT-detected ones.

Comparing V1369 Cen and V5668 Sgr in the context with other classical novae, they show lower values of total energy output as well as total number of emitted photons. However, this intriguing apparent inverse relationship of these quantities with gamma-ray durations (Fig. 5.10), can also be due to selection effects related to the Fermi-LAT sensitivity or to other uncertainties, e.g., on the distances.

A more extensive sample of LAT detected novae could help to understand whether this relation is in fact due to physics of the outbursts, particle acceleration, and ejecta parameters.

At this end, it's important the rapid communication with multi-wavelength facilities, but also the efforts made by the *Fermi* team in reducing the processing and transmission latencies in the ground network and to streamline the process for making ToO observations [4].

Further investigation using Pass8 data are also ongoing in order to explore the possibility of better constrain the low-energy (< 100 MeV) part of observed spectra and to possibly enlarge the detected sample taking advantage of Pass 8 improvements [74].

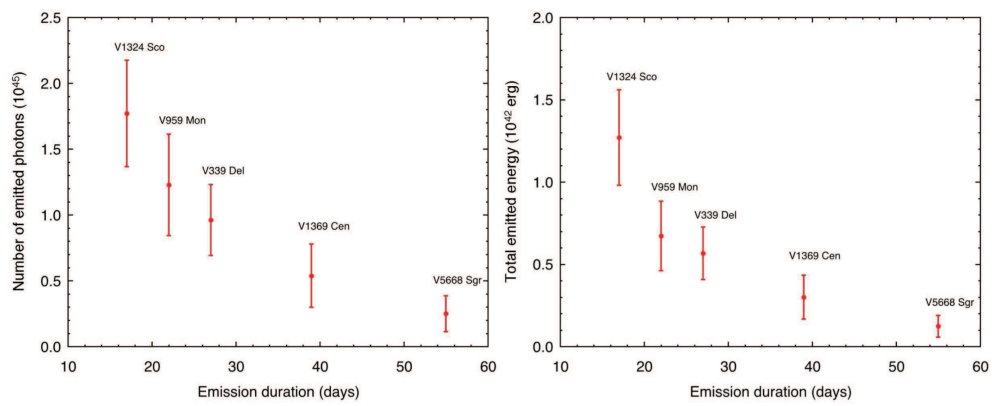


Figure 5.10: For the five classical novae detected by the LAT (thus excluding the symbiotic nova V407 Cyg), the total number of >100 MeV γ -ray photons emitted (left panel) and total emitted energies (right panel) are plotted versus the LAT-measured durations. Figures and caption taken by [56].

5.2 Searching for very-high-energy emission with Fermi-LAT and MAGIC

As explained above, gamma-ray emission (>100 MeV) from several classical novae has been detected by Fermi-LAT suggesting that these thermonuclear explosions in our Galaxy routinely accelerate particles to high energies. Although the observation of shocked material associated with the ejecta provides feasibility for gamma-ray production, the mechanism driving the acceleration is not yet well understood and the maximum energy attained is not known. Coordinated observations of LAT-detected novae performed by TeV telescopes can offer a chance to probe the energies reached in these explosive events. After summarizing the observations of novae YYHer and ASASSN-13ax, I will present the results of a joint study using LAT and MAGIC data and in particular the outburst detected by LAT from Nova V339 Del in 2013.

5.2.1 Fermi-LAT data analysis

I analyzed the LAT data in the energy range 100 MeV - 300 GeV using an unbinned maximum likelihood method [113] as implemented in the Fermi Science Tools v9r32p5. I applied the P7REP_SOURCE_V15 LAT Instrument Response Functions (IRFs) and used the associated standard Galactic and isotropic diffuse emission models matched to the Pass 7 reprocessed SOURCE class event selection¹. Events have been selected within a region of interest (ROI) of 15 deg in radius centered on:

- the LAT best-fit position reported by [23] for V339 Del,
- positions reported by the AAVSO International Database ² for YYHer and ASASSN-13ax.

I required a maximum zenith angle of 100 deg to avoid contamination by Earth limb photons ³. Because some of the LAT data were acquired during pointed mode observations, I applied an appropriate filter ⁴, selecting good quality data at times when either the rocking angle was less than 52 deg or the edge of the analysis region did not exceed the maximum zenith angle at 100 deg. Sources from the 2FGL catalog [130] located within the ROI were included in the model used to perform the fitting procedure.

¹The P7REP data, IRFs, and diffuse models (gll_iem_v05_rev1.fit and iso_source_v05.txt) are available at <http://fermi.gsfc.nasa.gov/ssc> .

²<https://www.aavso.org/aavso-international-database>

³Gamma-ray photons that arise from cosmic ray interactions with the Earth's atmosphere.

⁴http://fermi.gsfc.nasa.gov/ssc/data/analysis/documentation/Cicerone/Cicerone_Likelihood/Exposure.html

YYHer and ASASSN-13ax

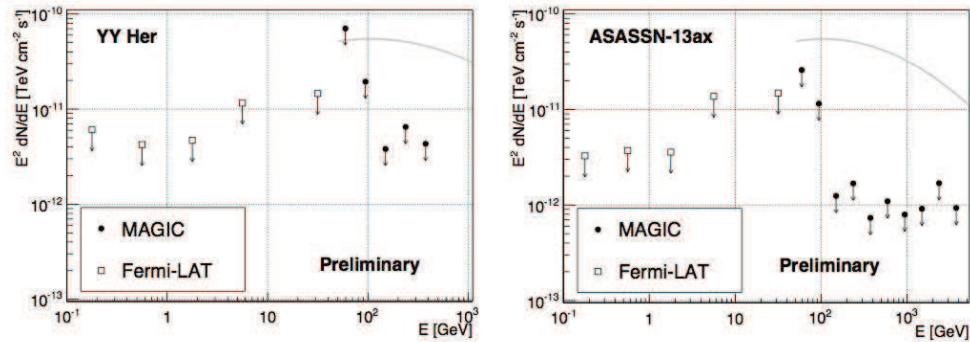


Figure 5.11: Differential upper limits on the flux from YYHer (on the left) and (on the right) as measured by Fermi-LAT (empty squares) and MAGIC (full circles). For comparison, a spectrum of Crab Nebula is shown in grey. [167]

YY Her is a symbiotic nova that undergoes a recurrent pattern of outbursts. MAGIC observations of YY Her occurred on the night of 2013 April 22/23, 7 days after the optical maximum but no significant VHE gamma-ray emission was detected. Analysis of Fermi-LAT data has been performed over a longer interval (2013 April 10 to April 30) but no emission was detected. Upper limits at 95% confidence level were set as 2.8×10^{-8} ph cm $^{-2}$ s $^{-1}$ above 100 MeV.

ASASSN-13ax belongs to a different class of cataclysmic variables, the dwarf novae, which are known for significantly weaker optical outbursts (2-6 magnitudes) than classical novae. Instead of undergoing thermonuclear explosions on the surface of the white dwarfs, these outbursts are caused by the gravitational energy release from a partial collapse of the accretion disk surrounding the white dwarf itself. MAGIC observations were performed on two consecutive nights starting on 2013 July 4, soon after the optical outburst but again no significant VHE gamma-ray emission was detected. Moreover, no high-energy emission was detected by the LAT over the interval 2013 June 25 to July 15. Upper limits at 95% confidence level were set as 1.6×10^{-8} ph cm $^{-2}$ s $^{-1}$ above 100 MeV. Differential upper limits obtained from the Fermi-LAT and MAGIC observations of YYHer and ASASSN-13ax are shown in Fig.5.11 [167].

V339 Del

As already said, V339 Del was a fast, classical CO nova detected by optical observations on 2013 August 16 (CBET #3628). The nova was exceptionally bright

reaching a magnitude of $V \sim 5$ mag (top panel of Fig.5.12), and it triggered follow-up observations at frequencies ranging from radio to VHE γ -rays. Nearly a month after the optical detection, X-ray emission was detected in the 1-10 keV energy band by Swift/XRT [137]; afterwards, the object became a low energy X-ray source with most of the photons detected in the 0.3-1 keV energy range, as reported by [132]. The pre-outburst optical images revealed the progenitor of nova V339 Del to be a blue star [63].

MAGIC observations of V339 Del were motivated by its extreme optical outburst and by the subsequent detection of GeV emission by the Fermi-LAT. MAGIC acquired data starting on the night of 2013 August 16 but these were marred by poor weather (affected by Calima, a dust layer originating from Sahara). The good quality data used for most of the analysis spans 8 nights between 2013 August 25 and September 4 for a total effective time of 11.6 h. No VHE γ -ray signal was found from the direction of V339 Del but night-by-night integral upper limits above 300 GeV have been computed (bottom panel of Fig.5.12) and differential upper limits for the whole good quality data set binned in energy are showed in Fig.5.13.

Nova V339 Del was the subject of a Fermi Target of Opportunity observation [89] triggered by the optical discovery: the pointed observation started on 2013 August 16 and lasted for 6 days. The γ -ray emission peaked on 2013 August 22 and entered a slow decay phase afterwards (Fig. 5.12). I fitted the flux for the light curves shown in the middle panel of Fig.5.12 by assuming a power-law spectral model with the normalization left free to vary and the photon index fixed to a single value. I then selected a fixed value for the photon index of 2.3 by calculating the average of the most significant 1-day bins (Test Statistic values $TS > 9$)⁵. The spectral energy distribution (SED) for V339 Del shown in Fig. 5.13 was extracted in 5 logarithmically spaced energy bins from 100 MeV to 100 GeV. Similarly to the light curves, energy-binned data shown in Fig.5.13 were fitted using a power law and calculating a 95% C.L. upper limit for bins with $TS < 9$. In the period coincident with the MAGIC observations (2013 August 25 to September 4 th), the Fermi-LAT spectrum can be described by a power law with an index of 2.4 ± 0.2 and flux of $(0.15 \pm 0.04) 10^{-6}$ ph cm⁻² s⁻¹ above 100 MeV. Only statistical error is included since they dominated over systematic error in these data ⁶. The spectral fit for this period had a TS of 49 and did not permit a constraint on an exponential cut-off energy. The Fermi-LAT analysis for the full decay phase, 2013 August 22 to September 12, provided a more significant signal ($TS=121$) and a similar value of flux above 100 MeV of $(0.13 \pm 0.03) 10^{-6}$ ph cm⁻² s⁻¹. The spectrum for the longer time period was fitted by an exponentially cut-off power law with an index

⁵Recall that the source significance in sigmas is $\sim \sqrt{TS}$ assuming one degree of freedom.

⁶Systematic uncertainties have been estimated by the LAT team as $\sim 8\%$ for the fluxes and ~ 0.1 in photon indices [24]

of 1.4 ± 0.3 and a cut-off energy of 1.6 ± 0.8 GeV. The fit improved in significance by 3.3σ with respect to a power-law model. The most energetic photon associated with V339 Del (89% probability for the best-fit model) has an energy $E=5.9$ GeV and was recorded on 2013 August 30, i.e., within the time period covered by the MAGIC observations.

The GeV emission observed by the LAT can be interpreted in terms of an inverse Compton process of electrons accelerated in a shock. In this case it is expected that protons in the same conditions can be accelerated to much higher energies. Consequently they may produce a second component in the γ -ray spectrum at TeV energies. The aim of the MAGIC-Fermi joint study was to explore the very-high-energy domain to search for γ -ray emission above 50 GeV and to shed light on the acceleration process of leptons and hadrons in nova explosions. As seen, no significant TeV emission was found from the studied sources but the combined GeV and TeV observations of V339 Del limit the ratio of proton to electron luminosities to $\frac{L_p}{L_e} \lesssim 0.1$. The increased power in electrons compared to protons may be related to how particles with different mass are injected in the acceleration process. The appearance of energetic e^+e^- pairs from nuclear decays produced in the nova explosion could help to inject them preferentially into the shock acceleration process. On the other hand, it is suggested in [162] that in a low- β plasma⁷, acceleration of electrons is preferred over protons if the particles are accelerated out of a thermal population. Both effects could lower the L_p/L_e ratio.

Details about MAGIC observations and the interpretation model can be found in [28].

⁷In plasma physics, β refers to the ratio of the plasma pressure to the magnetic pressure.

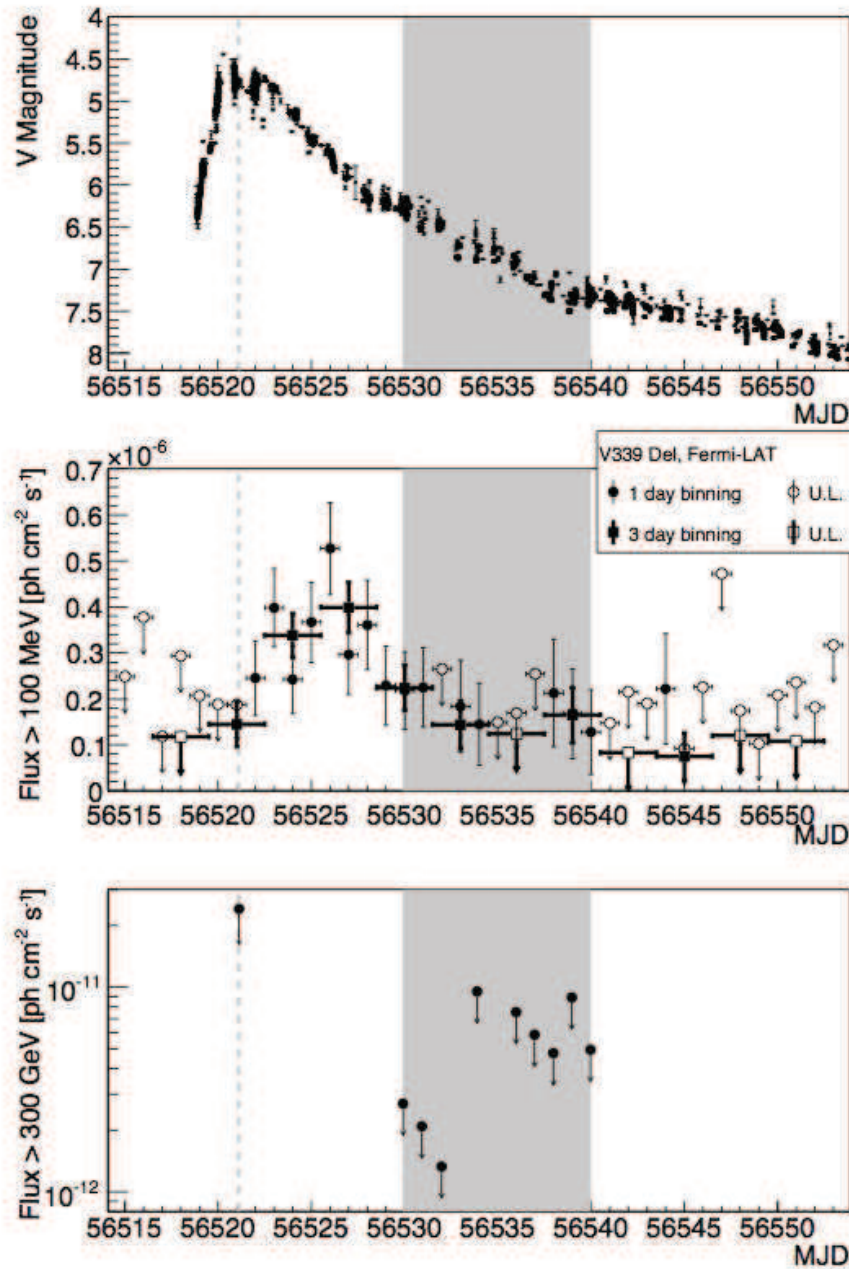


Figure 5.12: Multi-wavelength light curve of V339 Del during the outburst in August 2013. Top panel: Optical observations in the V band (obtained from the AAVSO-LCG service). Middle panel: Fermi-LAT flux (filled symbols) and upper limits (empty symbols) above 100 MeV in 1- day (circles, thin lines) or 3-day (squares, thick lines) bins. Bottom panel: Upper limit on the flux above 300 GeV observed with MAGIC telescopes. The gray band shows the observation nights with MAGIC while dashed gray line shows a MAGIC observation night affected by bad weather [28].

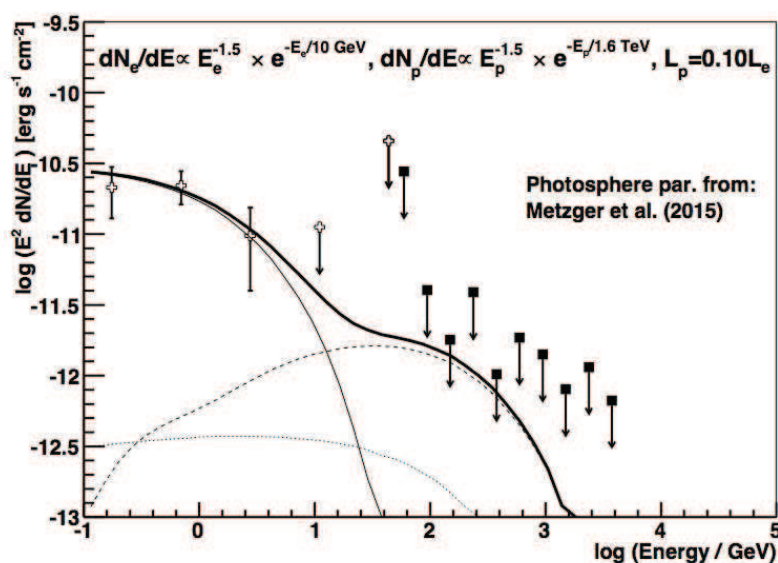


Figure 5.13: Differential upper limits on the flux from V339 Del as measured by MAGIC (filled squares) and Fermi-LAT (empty crosses) in the same time period (2013 August 25 to September 4). The thin solid line shows the IC scattering of thermal photons in the nova’s photosphere. The dashed line shows the γ -rays coming from the decay of π^0 from hadronic interactions of the relativistic protons with the nova ejecta. The dotted line shows the contribution of γ -rays coming from IC of e^+e^- originating from $\pi^+ \pi^-$ decays. Thick solid lines show the total predicted spectrum. The total energy of electrons is 6×10^{41} erg and the assumed proton to electron luminosity ratio is $\frac{L_p}{L_e} = 0.1$. Details about the modelling can be found in [28].

Chapter 6

Conclusions

In this thesis I presented different methods to optimize the analyses of different gamma-ray transient sources observed by the *Fermi* Large Area Telescope in the energy range 30 MeV - 500 GeV.

For short duration analyses (from fractions of second to hundreds of seconds), like those on the impulsive phase of GRBs and solar flares I used also the LAT Low-Energy data and the GBM data exploiting the *Fermi* low-energy capabilities. For the analyses of AGN and novae, the integration times span values from hours to weeks; in this case I showed analyses performed in the context of coordinated observations with the MAGIC very-high-energy Cherenkov telescope.

In Chapter 2, I presented results obtained by using an ad-hoc developed pipeline to optimize the spectral analysis of the impulsive phase of GRBs detected by the LAT through the LLE event selection.

Different spectral models, related to possible different physical models of the GRB's phenomenon, have been tested. For all GRBs in my sample, the Band function (see eq.2.3 and/or [43]) is found to not be the best-fit model reinforcing the recent evidence of a "Band-model crisis" (see, e.g., [86]): additional components (like power-law, exponential cut-offs and black-body photospheric component) are required to account for the observed spectra.

I reported the detailed results obtained in the spectral fit together with the measured fluence and an estimate of the Lorentz factor values for those GRBs showing a cut-off, in the assumption that it is due to γ - γ opacity.

These results also provide evidence that LLE data are very useful to better study the low-energy part of GRBs spectrum especially in the case of faint bursts, as also reported in some recent papers (e.g., [171, 121]).

The analysis method proposed here will be used for a forthcoming publication (in preparation) that will be the first systematic analysis of LLE-detected GRBs.

In Chapter 3, I presented the results of the spectral analysis of the impulsive phase of all solar flares in the sample of LLE detections using also GBM data.

For each flare, I tested different spectral models related to the different high-energy emission processes taking place in the solar atmosphere when magnetic reconnection phenomena occur accelerating particles at relativistic energies.

To better constrain the different spectral components at \sim keV-MeV energy range, ad-hoc GBM detector response matrices, generated with finer energy resolution, will be used to refine the analysis presented here. Ratios of emission observed by the GBM and LAT can be used to determine the relative numbers of accelerated ions in the associated energy ranges [123].

The final results will be part of the first catalog of solar flares detected by the LAT (in preparation).

In Chapter 4, I show the analysis strategy implemented using LAT data and an automated real-time analysis pipeline for the monitoring of possibly flaring AGN to provide a feedback for the repointing of the MAGIC telescopes.

The diversity of AGN flaring behavior and the intrinsically low duty cycle of Cherenkov telescopes makes necessary coordinated multiwavelength observations in order to maximize the chance to detect sources in high-state. I showed some high-lights of results obtained thorough the daily analysis of a large number¹ of AGN. The majority of these sources are faint and rarely reach the flux threshold necessary to be detected by MAGIC: for this reason it is of particular interest having an automated pipeline that routinely performs a large number of real-time analyses.

The LAT measurement of high-flux and hard spectral state, demonstrated to be a proxy for the discovery of VHE emission from ground-based Cherenkov telescopes (see, e.g., also [170, 133]). In this context, and also taking advantage of the LAT improved sensibility at high energies reached with Pass 8 data, the prompt follow-up of LAT results is very useful.

In Chapter 5, I presented the results of a joint MAGIC and LAT study on some galactic novae showing in details the observations performed on Nova V339 Del during its outbursts in August 2013.

Gamma-ray emission from several novae has been detected for the first time by the LAT suggesting that these thermonuclear explosions occurring in our Galaxy routinely accelerate particles to high energies. Coordinated observations of LAT-detected novae performed by TeV telescopes offer a chance to probe the energies reached in these explosive events and, as we showed in [28], to shed light on the acceleration process of leptons and hadrons in nova explosions.

The results obtained in this thesis show the importance of *Fermi*-LAT as a wide field instrument in the high-energy band to perform analyses on various classes of gamma-ray transient sources whose emission models show a large variety of

¹About 350 sources have been analyzed at least once from March 2013 up to now; \sim 150 of these are currently analyzed every day and results are distributed internally the MAGIC collaboration.

temporal and spectral characteristics.

For the future, the *Fermi* team is developing new strategies to leverage the Pass 8 enhancements to the LAT performance and the accumulated LAT observations of the γ -ray sky [4]. This is of particularly interest for the detection and study of transient sources: changes in operations will decrease data transmission and processing latencies and will enable more frequent ToO observations allowing near-simultaneous multi-wavelength and multi-messenger observations and studies. Such studies are key to revealing the nature of jet physics, particle acceleration and interaction processes at high-energies.

Bibliography

- [1] The Fermi Spacecraft. URL <https://www-glast.stanford.edu/pictures.html>.
- [2] Fermi LAT Performance, . URL https://www.slac.stanford.edu/exp/glast/groups/canda/lat_Performance.html.
- [3] Summary of LAT characteristics, . URL http://fermi.gsfc.nasa.gov/ssc/data/analysis/documentation/Cicerone/Cicerone_Introduction/LAT_overview.html.
- [4] 2016 Senior Review Proposal. URL <https://science.nasa.gov/astrophysics/2016-senior-review-operating-missions/>.
- [5] GRB 970228 observed by Beppo-SAX. URL <http://www.asdc.asi.it/bepposax/first/grb970228.html>.
- [6] Fermi Gamma Ray Burst Observations. URL <http://fermi.gsfc.nasa.gov/ssc/observations/types/grbs/>.
- [7] A. A. Abdo and et al. Gamma-Ray Flares from the Crab Nebula. *Science*, 331:739, February 2011. doi: 10.1126/science.1199705.
- [8] A. A. Abdo and et al. Fermi Large Area Telescope Observations of Two Gamma-Ray Emission Components from the Quiescent Sun. *ApJ*, 734:116, June 2011. doi: 10.1088/0004-637X/734/2/116.
- [9] A. A. Abdo, M. Ackermann, M. Ajello, J. Ampe, B. Anderson, W. B. Atwood, M. Axelsson, R. Bagagli, L. Baldini, J. Ballet, and et al. The on-orbit calibration of the Fermi Large Area Telescope. *Astroparticle Physics*, 32: 193–219, October 2009. doi: 10.1016/j.astropartphys.2009.08.002.
- [10] A. A. Abdo, M. Ackermann, M. Ajello, W. B. Atwood, L. Baldini, J. Ballet, G. Barbiellini, D. Bastieri, K. Bechtol, R. Bellazzini, and et al. Gamma-Ray Emission Concurrent with the Nova in the Symbiotic Binary V407 Cygni. *Science*, 329:817–821, August 2010. doi: 10.1126/science.1192537.

-
- [11] A. A. Abdo, M. Ackermann, M. Ajello, and et al. Fermi Large Area Telescope Observations of Misaligned Active Galactic Nuclei. *ApJ*, 720:912–922, September 2010. doi: 10.1088/0004-637X/720/1/912.
- [12] A. A. Abdo, M. Ackermann, and et al. Gamma-ray Light Curves and Variability of Bright Fermi-detected Blazars. *ApJ*, 722:520–542, October 2010. doi: 10.1088/0004-637X/722/1/520.
- [13] A. A. Abdo et al. Fermi Observations of High-Energy Gamma-Ray Emission from GRB 080916C. *Science*, 323:1688–, March 2009. doi: 10.1126/science.1169101.
- [14] F. Acero and et al. Fermi Large Area Telescope Third Source Catalog. *ApJS*, 218:23, June 2015. doi: 10.1088/0067-0049/218/2/23.
- [15] M. Ackermann and at al. Fermi Detection of γ -Ray Emission from the M2 Soft X-Ray Flare on 2010 June 12. *ApJ*, 745:144, February 2012. doi: 10.1088/0004-637X/745/2/144.
- [16] M. Ackermann and at al. High-energy Gamma-Ray Emission from Solar Flares: Summary of Fermi Large Area Telescope Detections and Analysis of Two M-class Flares. *ApJ*, 787:15, May 2014. doi: 10.1088/0004-637X/787/1/15.
- [17] M. Ackermann and et al. The First Fermi-LAT Gamma-Ray Burst Catalog. *ApJS*, 209:11, November 2013. doi: 10.1088/0067-0049/209/1/11.
- [18] M. Ackermann and et al. Fermi-LAT Observations of the Gamma-Ray Burst GRB 130427A. *Science*, 343:42–47, January 2014. doi: 10.1126/science.1242353.
- [19] M. Ackermann and et al. The Third Catalog of Active Galactic Nuclei Detected by the Fermi Large Area Telescope. *ApJ*, 810:14, September 2015. doi: 10.1088/0004-637X/810/1/14.
- [20] M. Ackermann and et al. Multiwavelength Evidence for Quasi-periodic Modulation in the Gamma-Ray Blazar PG 1553+113. *ApJ*, 813:L41, November 2015. doi: 10.1088/2041-8205/813/2/L41.
- [21] M. Ackermann, M. Ajello, and et al. Detection of a Spectral Break in the Extra Hard Component of GRB 090926A. *ApJ*, 729:114, March 2011. doi: 10.1088/0004-637X/729/2/114.

- [22] M. Ackermann, M. Ajello, and et al. The Second Catalog of Active Galactic Nuclei Detected by the Fermi Large Area Telescope. *ApJ*, 743:171, December 2011. doi: 10.1088/0004-637X/743/2/171.
- [23] M. Ackermann, M. Ajello, A. Albert, L. Baldini, and et al. Fermi establishes classical novae as a distinct class of gamma-ray sources. *Science*, 345:554–558, August 2014. doi: 10.1126/science.1253947.
- [24] M. Ackermann et al. The Fermi Large Area Telescope on Orbit: Event Classification, Instrument Response Functions, and Calibration. *ApJS*, 203: 4, November 2012. doi: 10.1088/0067-0049/203/1/4.
- [25] F. Aharonian and et al. An Exceptional Very High Energy Gamma-Ray Flare of PKS 2155-304. *ApJ*, 664:L71–L74, August 2007. doi: 10.1086/520635.
- [26] F. Aharonian, A. G. Akhperjanian, A. R. Bazer-Bachi, and et al. Observations of the Crab nebula with HESS. *A&A*, 457:899–915, October 2006. doi: 10.1051/0004-6361:20065351.
- [27] M. L. Ahnen, S. Ansoldi, L. A. Antonelli, P. Antoranz, A. Babic, B. Banerjee, P. Bangale, U. Barres de Almeida, J. A. Barrio, W. Bednarek, and et al. Very High Energy γ -Rays from the Universe’s Middle Age: Detection of the $z = 0.940$ Blazar PKS 1441+25 with MAGIC. *ApJ*, 815:L23, December 2015. doi: 10.1088/2041-8205/815/2/L23.
- [28] M. L. Ahnen, et al. for the MAGIC collaboration, R. Desiante, and E. Hays. Very high-energy γ -ray observations of novae and dwarf novae with the MAGIC telescopes. *A&A*, 582:A67, October 2015. doi: 10.1051/0004-6361/201526478.
- [29] M. Ajello, A. Albert, and at al. Impulsive and Long Duration High-energy Gamma-Ray Emission from the Very Bright 2012 March 7 Solar Flares. *ApJ*, 789:20, July 2014. doi: 10.1088/0004-637X/789/1/20.
- [30] C. Akerlof and et al. Observation of contemporaneous optical radiation from a γ -ray burst. *Nature*, 398:400–402, April 1999. doi: 10.1038/18837.
- [31] J. Aleksić and et al. Detection of Very High Energy γ -ray Emission from the Perseus Cluster Head-Tail Galaxy IC 310 by the MAGIC Telescopes. *ApJ*, 723:L207–L212, November 2010. doi: 10.1088/2041-8205/723/2/L207.
- [32] J. Aleksić and et al. Performance of the MAGIC stereo system obtained with Crab Nebula data. *Astroparticle Physics*, 35:435–448, February 2012. doi: 10.1016/j.astropartphys.2011.11.007.

- [33] J. Aleksić, S. Ansoldi, L. A. Antonelli, and et al. The major upgrade of the MAGIC telescopes, Part I: The hardware improvements and the commissioning of the system. *Astroparticle Physics*, 72:61–75, January 2016. doi: 10.1016/j.astropartphys.2015.04.004.
- [34] J. Aleksić, S. Ansoldi, L. A. Antonelli, and et al. The major upgrade of the MAGIC telescopes, Part II: A performance study using observations of the Crab Nebula. *Astroparticle Physics*, 72:76–94, January 2016. doi: 10.1016/j.astropartphys.2015.02.005.
- [35] K. A. Arnaud. XSPEC: The First Ten Years. In G. H. Jacoby and J. Barnes, editors, *Astronomical Data Analysis Software and Systems V*, volume 101 of *Astronomical Society of the Pacific Conference Series*, page 17, 1996.
- [36] K. Asano and S. Inoue. Prompt GeV-TeV Emission of Gamma-Ray Bursts Due to High-Energy Protons, Muons, and Electron-Positron Pairs. *ApJ*, 671: 645–655, December 2007. doi: 10.1086/522939.
- [37] W. Atwood, A. Albert, L. Baldini, M. Tinivella, J. Bregeon, M. Pesce-Rollins, C. Sgrò, P. Bruel, E. Charles, A. Drlica-Wagner, A. Franckowiak, T. Jogler, L. Rochester, T. Usher, M. Wood, J. Cohen-Tanugi, and S. Zimmer for the Fermi-LAT Collaboration. Pass 8: Toward the Full Realization of the Fermi-LAT Scientific Potential. *ArXiv e-prints*, March 2013.
- [38] W. B. Atwood, A. A. Abdo, M. Ackermann, W. Althouse, B. Anderson, M. Axelsson, L. Baldini, J. Ballet, D. L. Band, G. Barbiellini, and et al. et al. The Large Area Telescope on the Fermi Gamma-Ray Space Telescope Mission. *ApJ*, 697:1071–1102, June 2009. doi: 10.1088/0004-637X/697/2/1071.
- [39] W. B. Atwood, L. Baldini, J. Bregeon, P. Bruel, A. Chekhtman, J. Cohen-Tanugi, A. Drlica-Wagner, J. Granot, F. Longo, N. Omodei, M. Pesce-Rollins, S. Razzaque, L. S. Rochester, C. Sgrò, M. Tinivella, T. L. Usher, and S. Zimmer. New Fermi-LAT Event Reconstruction Reveals More High-energy Gamma Rays from Gamma-Ray Bursts. *ApJ*, 774:76, September 2013. doi: 10.1088/0004-637X/774/1/76.
- [40] W. B. Atwood et al. Design and initial tests of the Tracker-converter of the Gamma-ray Large Area Space Telescope. *Astroparticle Physics*, 28:422–434, December 2007. doi: 10.1016/j.astropartphys.2007.08.010.
- [41] M. Axelsson and et al. GRB110721A: An Extreme Peak Energy and Signatures of the Photosphere. *ApJ*, 757:L31, October 2012. doi: 10.1088/2041-8205/757/2/L31.

- [42] L. Baldini et al. Preliminary results of the LAT Calibration Unit beam tests. In S. Ritz, P. Michelson, and C. A. Meegan, editors, *The First GLAST Symposium*, volume 921 of *American Institute of Physics Conference Series*, pages 190–204, July 2007. doi: 10.1063/1.2757300.
- [43] D. Band et al. BATSE observations of gamma-ray burst spectra. I - Spectral diversity. *ApJ*, 413:281–292, August 1993. doi: 10.1086/172995.
- [44] D. L. Band et al. Prospects for GRB Science with the Fermi Large Area Telescope. *ApJ*, 701:1673–1694, August 2009. doi: 10.1088/0004-637X/701/2/1673.
- [45] A. O. Benz. Flare Observations. *Living Reviews in Solar Physics*, 5, February 2008. doi: 10.12942/lrsp-2008-1.
- [46] E. Berger, P. A. Price, S. B. Cenko, A. Gal-Yam, A. M. Soderberg, M. Kasliwal, D. C. Leonard, P. B. Cameron, D. A. Frail, S. R. Kulkarni, D. C. Murphy, W. Krzeminski, T. Piran, B. L. Lee, K. C. Roth, D.-S. Moon, D. B. Fox, F. A. Harrison, S. E. Persson, B. P. Schmidt, B. E. Penprase, J. Rich, B. A. Peterson, and L. L. Cowie. The afterglow and elliptical host galaxy of the short γ -ray burst GRB 050724. *Nature*, 438:988–990, December 2005. doi: 10.1038/nature04238.
- [47] E. Bissaldi and et al. First-year Results of Broadband Spectroscopy of the Brightest Fermi-GBM Gamma-Ray Bursts. *ApJ*, 733:97, June 2011. doi: 10.1088/0004-637X/733/2/97.
- [48] G. Bonnoli, G. Ghisellini, L. Foschini, F. Tavecchio, and G. Ghirlanda. The γ -ray brightest days of the blazar 3C 454.3. *MNRAS*, 410:368–380, January 2011. doi: 10.1111/j.1365-2966.2010.17450.x.
- [49] J. Bregeon, E. Charles, and M. Wood for the Fermi-LAT collaboration. Fermi-LAT data reprocessed with updated calibration constants. *ArXiv e-prints 1304.5456*, April 2013.
- [50] D. N. Burrows, A. Falcone, G. Chincarini, D. Morris, P. Romano, J. E. Hill, O. Godet, A. Moretti, H. Krimm, J. P. Osborne, J. Racusin, V. Mangano, K. Page, M. Perri, M. Stroh, and Swift XRT Team. X-ray flares in early GRB afterglows. *Philosophical Transactions of the Royal Society of London Series A*, 365:1213–1226, May 2007. doi: 10.1098/rsta.2006.1970.
- [51] P. Carlson, T. Francke, C. Fuglesang, N. Weber, and M. Suffert. Long narrow CsI(Tl) rods as calorimeter elements. *Nuclear Instruments and Methods in*

- Physics Research A*, 376:271–274, February 1996. doi: 10.1016/0168-9002(96)00198-2.
- [52] R. C. Carrington. Description of a Singular Appearance seen in the Sun on September 1, 1859. *MNRAS*, 20:13–15, November 1859. doi: 10.1093/mnras/20.1.13.
- [53] M. Cerruti, C. D. Dermer, B. Lott, C. Boisson, and A. Zech. Gamma-Ray Blazars near Equipartition and the Origin of the GeV Spectral Break in 3C 454.3. *ApJ*, 771:L4, July 2013. doi: 10.1088/2041-8205/771/1/L4.
- [54] C. C. Cheung and et al. Gamma-Ray Novae. *GammaSIG Meeting 2015*, 2015.
- [55] C. C. Cheung and et al. Fermi Reveals New Light on Novae in Gamma rays. *Proceedings of Science 386 (ICRC2015), 34th ICRC, 880*, 2015.
- [56] C. C. Cheung, P. Jean, S. N. Shore, Ł. Stawarz, R. H. D. Corbet, J. Knödlseher, S. Starrfield, D. L. Wood, R. Desiante, F. Longo, G. Pivato, and K. S. Wood. Fermi-LAT Gamma-Ray Detections of Classical Novae V1369 Centauri 2013 and V5668 Sagittarii 2015. *ApJ*, 826:142, August 2016. doi: 10.3847/0004-637X/826/2/142.
- [57] E. L. Chupp, D. J. Forrest, P. R. Higbie, A. N. Suri, C. Tsai, and P. P. Dunphy. Solar Gamma Ray Lines observed during the Solar Activity of August 2 to August 11, 1972. *Nature*, 241:333–335, February 1973. doi: 10.1038/241333a0.
- [58] S. A. Colgate. Prompt gamma rays and X-rays from supernovae. *Canadian Journal of Physics Supplement*, 46:476, 1968.
- [59] V. Connaughton and et al. Localization of Gamma-Ray Bursts Using the Fermi Gamma-Ray Burst Monitor. *ApJS*, 216:32, February 2015. doi: 10.1088/0067-0049/216/2/32.
- [60] A. Cucchiara, A. J. Levan, D. B. Fox, N. R. Tanvir, T. N. Ukwatta, E. Berger, T. Krühler, A. Küpcü Yoldaş, X. F. Wu, K. Toma, J. Greiner, F. E. Olivares, A. Rowlinson, L. Amati, T. Sakamoto, K. Roth, A. Stephens, A. Fritz, J. P. U. Fynbo, J. Hjorth, D. Malesani, P. Jakobsson, K. Wiersema, P. T. O’Brien, A. M. Soderberg, R. J. Foley, A. S. Fruchter, J. Rhoads, R. E. Rutledge, B. P. Schmidt, M. A. Dopita, P. Podsiadlowski, R. Willingale, C. Wolf, S. R. Kulkarni, and P. D’Avanzo. A Photometric Redshift of $z \sim 9.4$ for GRB 090429B. *ApJ*, 736:7, July 2011. doi: 10.1088/0004-637X/736/1/7.

- [61] M. De Pasquale and et al. Swift and Fermi Observations of the Early Afterglow of the Short Gamma-Ray Burst 090510. *ApJ*, 709:L146–L151, February 2010. doi: 10.1088/2041-8205/709/2/L146.
- [62] J. H. Dellinger. A New Cosmic Phenomenon. *Science*, 82:351, October 1935. doi: 10.1126/science.82.2128.351.
- [63] D. Denisenko, C. Jacques, E. Pimentel, E. Guido, N. Ruocco, N. Howes, G. Masi, P. Schmeer, and F. Nocentini. V339 Delphini = Nova Delphini 2013 = Pnv J20233073+2046041. *IAU Circ.*, 9258, September 2013.
- [64] C. D. Dermer. The blazar paradigm and its discontents. *Mem. Soc. Astron. Italiana*, 86:13, 2015.
- [65] C. D. Dermer and A. Atoyan. Ultra-high energy cosmic rays, cascade gamma rays, and high-energy neutrinos from gamma-ray bursts. *New Journal of Physics*, 8:122, July 2006. doi: 10.1088/1367-2630/8/7/122.
- [66] S. G. Djorgovski, M. R. Metzger, S. R. Kulkarni, S. C. Odewahn, R. R. Gal, M. A. Pahre, D. A. Frail, M. Feroci, E. Costa, and E. Palazzi. The optical counterpart to the γ -ray burst GRB970508. *Nature*, 387:876–878, June 1997. doi: 10.1038/43126.
- [67] D. Donato, G. Ghisellini, G. Tagliaferri, and G. Fossati. Hard X-ray properties of blazars. *A&A*, 375:739–751, September 2001. doi: 10.1051/0004-6361:20010675.
- [68] D. Eichler and A. Levinson. A Compact Fireball Model of Gamma-Ray Bursts. *ApJ*, 529:146–150, January 2000. doi: 10.1086/308245.
- [69] D. Eichler, M. Livio, T. Piran, and D. N. Schramm. Nucleosynthesis, neutrino bursts and gamma-rays from coalescing neutron stars. *Nature*, 340:126–128, July 1989. doi: 10.1038/340126a0.
- [70] G. J. Fishman and C. A. Meegan. Gamma-Ray Bursts. *ARA&A*, 33:415–458, 1995. doi: 10.1146/annurev.aa.33.090195.002215.
- [71] W. Fong, E. Berger, and D. B. Fox. Hubble Space Telescope Observations of Short Gamma-Ray Burst Host Galaxies: Morphologies, Offsets, and Local Environments. *ApJ*, 708:9–25, January 2010. doi: 10.1088/0004-637X/708/1/9.
- [72] W. Fong, E. Berger, R. Chornock, R. Margutti, A. J. Levan, N. R. Tanvir, R. L. Tunnicliffe, I. Czekala, D. B. Fox, D. A. Perley, S. B. Cenko, B. A.

- Zauderer, T. Laskar, S. E. Persson, A. J. Monson, D. D. Kelson, C. Birk, D. Murphy, M. Servillat, and G. Anglada. Demographics of the Galaxies Hosting Short-duration Gamma-Ray Bursts. *ApJ*, 769:56, May 2013. doi: 10.1088/0004-637X/769/1/56.
- [73] D. B. Fox, D. A. Frail, P. A. Price, S. R. Kulkarni, E. Berger, T. Piran, A. M. Soderberg, S. B. Cenko, P. B. Cameron, A. Gal-Yam, M. M. Kasliwal, D.-S. Moon, F. A. Harrison, E. Nakar, B. P. Schmidt, B. Penprase, R. A. Chevalier, P. Kumar, K. Roth, D. Watson, B. L. Lee, S. Sheckman, M. M. Phillips, M. Roth, P. J. McCarthy, M. Rauch, L. Cowie, B. A. Peterson, J. Rich, N. Kawai, K. Aoki, G. Kosugi, T. Totani, H.-S. Park, A. MacFadyen, and K. C. Hurley. The afterglow of GRB 050709 and the nature of the short-hard γ -ray bursts. *Nature*, 437:845–850, October 2005. doi: 10.1038/nature04189.
- [74] A. Franckowiak and et al. . *Abstrac for the Sixth Fermi Symposium*, 2015.
- [75] H. Friedman, S. W. Lichtman, and E. T. Byram. Photon Counter Measurements of Solar X-Rays and Extreme Ultraviolet Light. *Physical Review*, 83: 1025–1030, September 1951. doi: 10.1103/PhysRev.83.1025.
- [76] R. Fruhwirth, Regler M., R. K. Bock, H. Grote, and D. Notz. *Data Analysis Techniques for High-Energy Physics* (2nd ed.; Cambridge: Cambridge Univ. Pres) .
- [77] S. B. Gavler et al. Radiation tests of CsI(Tl) crystals for the GLAST satellite mission. *Nuclear Instruments and Methods in Physics Research*, 545:842–851, June 2005.
- [78] N. Gehrels and S. Razzaque. Gamma-ray bursts in the swift-Fermi era. *Frontiers of Physics*, 8:661–678, December 2013. doi: 10.1007/s11467-013-0282-3.
- [79] G. Ghisellini, editor. *Radiative Processes in High Energy Astrophysics*, volume 873 of *Lecture Notes in Physics*, Berlin Springer Verlag, 2013. doi: 10.1007/978-3-319-00612-3.
- [80] G. Ghisellini and A. Celotti. Quasi-thermal Comptonization and Gamma-Ray Bursts. *ApJ*, 511:L93–L96, February 1999. doi: 10.1086/311845.
- [81] G. Ghisellini, G. Ghirlanda, L. Nava, and A. Celotti. GeV emission from gamma-ray bursts: a radiative fireball? *MNRAS*, 403:926–937, April 2010. doi: 10.1111/j.1365-2966.2009.16171.x.
- [82] A. Goldstein et al. The Fermi GBM Gamma-Ray Burst Spectral Catalog: The First Two Years. *ApJS*, 199:19, March 2012. doi: 10.1088/0067-0049/199/1/19.

- [83] J. E. Grove and W. N. Johnson. The calorimeter of the Fermi Large Area Telescope. In *Space Telescopes and Instrumentation 2010: Ultraviolet to Gamma Ray*, volume 7732 of Proc. SPIE, page 77320J, July 2010. doi: 10.1117/12.857839.
- [84] D. Gruber and et al. The Fermi GBM Gamma-Ray Burst Spectral Catalog: Four Years of Data. *ApJS*, 211:12, March 2014. doi: 10.1088/0067-0049/211/1/12.
- [85] S. Guiriec and et al. Detection of a Thermal Spectral Component in the Prompt Emission of GRB 100724B. *ApJ*, 727:L33, February 2011. doi: 10.1088/2041-8205/727/2/L33.
- [86] S. Guiriec, C. Kouveliotou, F. Daigne, B. Zhang, R. Hascoët, R. S. Nemmen, D. J. Thompson, P. N. Bhat, N. Gehrels, M. M. Gonzalez, Y. Kaneko, J. McEnery, R. Mochkovitch, J. L. Racusin, F. Ryde, J. R. Sacahui, and A. M. Ünsal. Toward a Better Understanding of the GRB Phenomenon: a New Model for GRB Prompt Emission. *ApJ*, 807:148, July 2015. doi: 10.1088/0004-637X/807/2/148.
- [87] N. Gupta and B. Zhang. Prompt emission of high-energy photons from gamma ray bursts. *MNRAS*, 380:78–92, September 2007. doi: 10.1111/j.1365-2966.2007.12051.x.
- [88] R. C. Hartman and et al. Multiepoch Multiwavelength Spectra and Models for Blazar 3C 279. *ApJ*, 553:683–694, June 2001. doi: 10.1086/320970.
- [89] E. Hays, T. Cheung, and S. Ciprini. Detection of gamma rays from Nova Delphini 2013. *The Astronomer’s Telegram*, 5302, August 2013.
- [90] M. Hernanz. Explosion, turn-off and recovery of accretion in novae revealed by X-rays. *The X-ray Universe 2011*, 2011.
- [91] J. S. Hey, S. J. Parsons, and J. W. Phillips. Some Characteristics of Solar Radio Emissions. *MNRAS*, 108:354, 1948. doi: 10.1093/mnras/108.5.354.
- [92] A. M. Hillas. Cerenkov light images of EAS produced by primary gamma. *International Cosmic Ray Conference*, 3, August 1985.
- [93] A. M. Hillas. Evolution of ground-based gamma-ray astronomy from the early days to the Cherenkov Telescope Arrays. *Astroparticle Physics*, 43: 19–43, March 2013. doi: 10.1016/j.astropartphys.2012.06.002.

- [94] J. Hinton. Ground-based gamma-ray astronomy with Cherenkov telescopes. *New Journal of Physics*, 11(5):055005, May 2009. doi: 10.1088/1367-2630/11/5/055005.
- [95] J. Holder, V. A. Acciari, E. Aliu, and et al. Status of the VERITAS Observatory. In F. A. Aharonian, W. Hofmann, and F. Rieger, editors, *American Institute of Physics Conference Series*, volume 1085 of *American Institute of Physics Conference Series*, pages 657–660, December 2008. doi: 10.1063/1.3076760.
- [96] H. S. Hudson. Global Properties of Solar Flares. *Space Sci. Rev.*, 158:5–41, January 2011. doi: 10.1007/s11214-010-9721-4.
- [97] J. D. Hunter. Matplotlib: A 2D graphics environment. *Computing In Science & Engineering*, 9(3):90–95, 2007.
- [98] K. Hurley. Detection of a γ -ray burst of very long duration and very high energy. *Nature*, 372:652–654, December 1994. doi: 10.1038/372652a0.
- [99] W. N. Johnson, J. E. Grove, B. F. Philips, H. Arrighi, J. Krizmanic, J. Norris, S. Ritz, S. Singh, and D. Suson. CsI Hodoscopic Calorimeter for the GLAST Mission. In *AAS/High Energy Astrophysics Division #4*, volume 31 of *Bulletin of the American Astronomical Society*, page 735, April 1999.
- [100] G. Kanbach, D. L. Bertsch, C. E. Fichtel, R. C. Hartman, S. D. Hunter, D. A. Kniffen, P. W. Kwok, Y. C. Lin, J. R. Mattox, and H. A. Mayer-Hasselwander. Detection of a long-duration solar gamma-ray flare on June 11, 1991 with EGRET on COMPTON-GRO. *A&AS*, 97:349–353, January 1993.
- [101] R. W. Klebesadel, I. B. Strong, and R. A. Olson. Observations of Gamma-Ray Bursts of Cosmic Origin. *ApJ*, 182:L85, June 1973. doi: 10.1086/181225.
- [102] C. Kouveliotou, C. A. Meegan, G. J. Fishman, N. P. Bhat, M. S. Briggs, T. M. Koshut, W. S. Paciesas, and G. N. Pendleton. Identification of two classes of gamma-ray bursts. *ApJ*, 413:L101–L104, August 1993. doi: 10.1086/186969.
- [103] R. P. Kraft. Binary Stars among Cataclysmic Variables. III. Ten Old Novae. *ApJ*, 139:457, February 1964. doi: 10.1086/147776.
- [104] P. Kumar and R. Barniol Duran. On the generation of high-energy photons detected by the Fermi Satellite from gamma-ray bursts. *MNRAS*, 400:L75–L79, November 2009. doi: 10.1111/j.1745-3933.2009.00766.x.

- [105] P. Kumar and R. Barniol Duran. External forward shock origin of high-energy emission for three gamma-ray bursts detected by Fermi. *MNRAS*, 409:226–236, November 2010. doi: 10.1111/j.1365-2966.2010.17274.x.
- [106] C. N. Leibler and E. Berger. The Stellar Ages and Masses of Short Gamma-ray Burst Host Galaxies: Investigating the Progenitor Delay Time Distribution and the Role of Mass and Star Formation in the Short Gamma-ray Burst Rate. *ApJ*, 725:1202–1214, December 2010. doi: 10.1088/0004-637X/725/1/1202.
- [107] Z. Li. Prompt GeV Emission from Residual Collisions in Gamma-Ray Burst Outflows: Evidence from Fermi Observations of Grb 080916c. *ApJ*, 709:525–534, January 2010. doi: 10.1088/0004-637X/709/1/525.
- [108] M. S. Longair. *High Energy Astrophysics*. February 2011.
- [109] F. Longo, R. Desiante, and et al. Toward the LAT solar flare catalog. *Poster presented at the Sixth Fermi Symposium*, 2015.
- [110] E. Lorenz and The MAGIC Collaboration. Status of the 17 m MAGIC telescope. *New A Rev.*, 48:339–344, April 2004. doi: 10.1016/j.newar.2003.12.059.
- [111] E. Lorenz and R. Wagner. Very-high energy gamma-ray astronomy. A 23-year success story in high-energy astroparticle physics. *European Physical Journal H*, 37:459–513, August 2012. doi: 10.1140/epjh/e2012-30016-x.
- [112] D. Lynden-Bell. Galactic Nuclei as Collapsed Old Quasars. *Nature*, 223:690–694, August 1969. doi: 10.1038/223690a0.
- [113] J. R. Mattox, D. L. Bertsch, J. Chiang, B. L. Dingus, and et al. The Likelihood Analysis of EGRET Data. *ApJ*, 461:396, April 1996. doi: 10.1086/177068.
- [114] C. Meegan et al. The Fermi Gamma-ray Burst Monitor. *ApJ*, 702:791–804, September 2009. doi: 10.1088/0004-637X/702/1/791.
- [115] C. A. Meegan, G. J. Fishman, R. B. Wilson, J. M. Horack, M. N. Brock, W. S. Paciasas, G. N. Pendleton, and C. Kouveliotou. Spatial distribution of gamma-ray bursts observed by BATSE. *Nature*, 355:143–145, January 1992. doi: 10.1038/355143a0.
- [116] P. Meszaros and M. J. Rees. Gamma-Ray Bursts: Multiwaveband Spectral Predictions for Blast Wave Models. *ApJ*, 418:L59, December 1993. doi: 10.1086/187116.

- [117] P. Meszaros and M. J. Rees. Relativistic fireballs and their impact on external matter - Models for cosmological gamma-ray bursts. *ApJ*, 405:278–284, March 1993. doi: 10.1086/172360.
- [118] P. Mészáros and M. J. Rees. Steep Slopes and Preferred Breaks in Gamma-Ray Burst Spectra: The Role of Photospheres and Comptonization. *ApJ*, 530:292–298, February 2000. doi: 10.1086/308371.
- [119] P. Meszaros, M. J. Rees, et al. Optical and Long-Wavelength Afterglow from Gamma-Ray Bursts. *ApJ*, 476:232, February 1997. doi: 10.1086/303625.
- [120] A. A. Moiseev, R. C. Hartman, J. F. Ormes, D. J. Thompson, M. J. Amato, T. E. Johnson, K. N. Segal, and D. A. Sheppard. The anti-coincidence detector for the GLAST large area telescope. *Astroparticle Physics*, 27:339–358, June 2007. doi: 10.1016/j.astropartphys.2006.12.003.
- [121] E. Moretti and M. Axelsson. Signs of magnetic acceleration and multizone emission in GRB 080825C. *MNRAS*, 458:1728–1732, May 2016. doi: 10.1093/mnras/stw432.
- [122] R. J. Murphy, C. D. Dermer, and R. Ramaty. High-energy processes in solar flares. *ApJS*, 63:721–748, March 1987. doi: 10.1086/191180.
- [123] R. J. Murphy, G. H. Share, J. E. Grove, W. N. Johnson, R. L. Kinzer, J. D. Kurfess, M. S. Strickman, and G. V. Jung. Accelerated Particle Composition and Energetics and Ambient Abundances from Gamma-Ray Spectroscopy of the 1991 June 4 Solar Flare. *ApJ*, 490:883–900, December 1997.
- [124] R. J. Murphy, G. H. Share, J. G. Skibo, and B. Kozlovsky. The Physics of Positron Annihilation in the Solar Atmosphere. *ApJS*, 161:495–519, December 2005. doi: 10.1086/452634.
- [125] R. J. Murphy, B. Kozlovsky, G. H. Share, X.-M. Hua, and R. E. Lingenfelter. Using Gamma-Ray and Neutron Emission to Determine Solar Flare Accelerated Particle Spectra and Composition and the Conditions within the Flare Magnetic Loop. *ApJS*, 168:167–194, January 2007. doi: 10.1086/509637.
- [126] R. J. Murphy, B. Kozlovsky, J. Kiener, and G. H. Share. Nuclear Gamma-Ray De-Excitation Lines and Continuum from Accelerated-Particle Interactions in Solar Flares. *ApJS*, 183:142–155, July 2009. doi: 10.1088/0067-0049/183/1/142.
- [127] E. Nakar. Short-hard gamma-ray bursts. *Phys. Rep.*, 442:166–236, April 2007. doi: 10.1016/j.physrep.2007.02.005.

- [128] R. Narayan, B. Paczynski, T. Piran, et al. Gamma-ray bursts as the death throes of massive binary stars. *Astrophysical Journal Letters*, 395:L83–L86, August 1992. doi: 10.1086/186493.
- [129] P. L. Nolan, W. F. Tompkins, I. A. Grenier, and P. F. Michelson. Variability of EGRET Gamma-Ray Sources. *ApJ*, 597:615–627, November 2003. doi: 10.1086/378353.
- [130] P. L. Nolan, A. A. Abdo, M. Ackermann, M. Ajello, and et al. Fermi Large Area Telescope Second Source Catalog. *ApJS*, 199:31, April 2012. doi: 10.1088/0067-0049/199/2/31.
- [131] N. Omodei, V. Petrosian, W. Liu, F. Rubio da Costa, Q. Chen, M. Pesce-Rollins, E. Grove, F. Longo, and for the Fermi-LAT Collaboration. Shedding new light on the Sun with the Fermi LAT. *ArXiv e-prints 1502.03895*, February 2015.
- [132] J. P. Osborne, K. Page, A. Beardmore, C. Woodward, G. Schwarz, M. Bode, J.-U. Ness, S. Shore, S. Starrfield, M. Wagner, and F. Walter. Nova Del 2013 (V339 Del) is now a bright super-soft X-ray source. *The Astronomer's Telegram*, 5505, October 2013.
- [133] L. Pacciani, F. Tavecchio, I. Donnarumma, A. Stamerra, L. Carrasco, E. Re-cillas, A. Porras, and M. Uemura. Exploring the Blazar Zone in High-energy Flares of FSRQs. *ApJ*, 790:45, August 2014. doi: 10.1088/0004-637X/790/1/45.
- [134] W. S. Paciesas et al. The Fourth BATSE Gamma-Ray Burst Catalog (Revised). *The Astrophysical Journal Supplement Series*, 122:465–495, June 1999. doi: 10.1086/313224.
- [135] B. Paczynski. Super-Eddington winds from neutron stars. *ApJ*, 363:218–226, November 1990. doi: 10.1086/169332.
- [136] P. Padovani and P. Giommi. The connection between x-ray- and radio-selected BL Lacertae objects. *ApJ*, 444:567–581, May 1995. doi: 10.1086/175631.
- [137] K. L. Page, J. P. Osborne, N. P. M. Kuin, C. E. Woodward, G. J. Schwarz, S. Starrfield, S. N. Shore, and F. M. Walter. Detection of super-soft emission in nova V339 Del. *The Astronomer's Telegram*, 5470, October 2013.
- [138] A. Pe'Er, B.-B. Zhang, F. Ryde, S. McGlynn, B. Zhang, R. D. Preece, and C. Kouveliotou. The connection between thermal and non-thermal emission

- in gamma-ray bursts: general considerations and GRB 090902B as a case study. *MNRAS*, 420:468–482, February 2012. doi: 10.1111/j.1365-2966.2011.20052.x.
- [139] M. Pesce-Rollins and et al. *Astroparticle Physics 2014, A Joint TeVPA/IDM Conference*. URL <http://indico.cern.ch/event/278032/session/9/contribution/201/material/slides/0.pdf>.
- [140] M. Pesce-Rollins, N. Omodei, V. Petrosian, W. Liu, F. Rubio da Costa, A. Allafort, and Q. Chen. First Detection of > 100 MeV Gamma-Rays Associated with a Behind-the-limb Solar Flare. *ApJ*, 805:L15, June 2015. doi: 10.1088/2041-8205/805/2/L15.
- [141] M. Pesce-Rollins, N. Omodei, V. Petrosian, W. Liu, F. Rubio da Costa, A. Allafort, and for the Fermi-LAT Collaboration. Fermi Large Area Telescope observations of high-energy gamma-ray emission from behind-the-limb solar flares. *ArXiv e-prints*, July 2015.
- [142] B. M. Peterson. *An Introduction to Active Galactic Nuclei*. February 1997.
- [143] L. E. Peterson and J. R. Winckler. Gamma-Ray Burst from a Solar Flare. *J. Geophys. Res.*, 64:697–707, July 1959. doi: 10.1029/JZ064i007p00697.
- [144] T. Piran. Astronomy: Glowing embers. *Nature*, 422:268–269, March 2003.
- [145] R. Preece and et al. The First Pulse of the Extremely Bright GRB 130427A: A Test Lab for Synchrotron Shocks. *Science*, 343:51–54, January 2014. doi: 10.1126/science.1242302.
- [146] R. D. Preece, M. S. Briggs, R. S. Mallozzi, G. N. Pendleton, W. S. Paciasas, and D. L. Band. The Synchrotron Shock Model Confronts a “Line of Death” in the BATSE Gamma-Ray Burst Data. *ApJ*, 506:L23–L26, October 1998. doi: 10.1086/311644.
- [147] R. D. Preece, M. S. Briggs, R. S. Mallozzi, G. N. Pendleton, W. S. Paciasas, D. L. Band, et al. The BATSE Gamma-Ray Burst Spectral Catalog. I. High Time Resolution Spectroscopy of Bright Bursts Using High Energy Resolution Data. *ApJS*, 126:19–36, January 2000. doi: 10.1086/313289.
- [148] E. R. Priest. Book-Review - Solar Flare Magnetohydrodynamics. *Science*, 214:356, October 1981.
- [149] R. Ramaty and N. Mandzhavidze. Theoretical models for high-energy solar flare emissions. In J. Ryan and W. T. Vestrand, editors, *High-Energy Solar*

- Phenomena - a New Era of Spacecraft Measurements*, volume 294 of *American Institute of Physics Conference Series*, pages 24–44, December 1994.
- [150] R. Rando and for the Fermi LAT Collaboration. Post-launch performance of the Fermi Large Area Telescope. *ArXiv e-prints 0907.0626*, July 2009.
- [151] G. Rank, J. Ryan, H. Debrunner, M. McConnell, and V. Schönfelder. Extended gamma-ray emission of the solar flares in june 1991. *A&A*, 378:1046–1066, November 2001. doi: 10.1051/0004-6361:20011060.
- [152] S. Razzaque, C. D. Dermer, and J. D. Finke. The Stellar Contribution to the Extragalactic Background Light and Absorption of High-Energy Gamma Rays. *ApJ*, 697:483–492, May 2009. doi: 10.1088/0004-637X/697/1/483.
- [153] D. V. Reames. Coronal abundances determined from energetic particles. *Advances in Space Research*, 15, July 1995.
- [154] M. J. Rees. Appearance of Relativistically Expanding Radio Sources. *Nature*, 211:468–470, July 1966. doi: 10.1038/211468a0.
- [155] M. J. Rees and P. Meszaros. Unsteady outflow models for cosmological gamma-ray bursts. *ApJ*, 430:L93–L96, August 1994. doi: 10.1086/187446.
- [156] M. J. Rees, P. Meszaros, et al. Relativistic fireballs - Energy conversion and time-scales. *MNRAS*, 258:41P–43P, September 1992.
- [157] J. M. Ryan. Long-Duration Solar Gamma-Ray Flares. *Space Sci. Rev.*, 93: 581–610, August 2000.
- [158] F. Ryde, M. Axelsson, B. B. Zhang, S. McGlynn, A. Pe’er, C. Lundman, S. Larsson, M. Battelino, B. Zhang, E. Bissaldi, J. Bregeon, M. S. Briggs, J. Chiang, F. de Palma, S. Guiriec, J. Larsson, F. Longo, S. McBreen, N. Omodei, V. Petrosian, R. Preece, and A. J. van der Horst. Identification and Properties of the Photospheric Emission in GRB090902B. *ApJ*, 709: L172–L177, February 2010. doi: 10.1088/2041-8205/709/2/L172.
- [159] E. E. Salpeter. Accretion of Interstellar Matter by Massive Objects. *ApJ*, 140:796–800, August 1964. doi: 10.1086/147973.
- [160] J. D. Scargle, J. P. Norris, B. Jackson, and J. Chiang. Studies in Astronomical Time Series Analysis. VI. Bayesian Block Representations. *ApJ*, 764:167, February 2013. doi: 10.1088/0004-637X/764/2/167.

- [161] B. E. Schaefer. Comprehensive Photometric Histories of All Known Galactic Recurrent Novae. *ApJS*, 187:275–373, April 2010. doi: 10.1088/0067-0049/187/2/275.
- [162] R. Schlickeiser. Particle Acceleration Processes in Cosmic Plasmas. In L. Klein, editor, *Energy Conversion and Particle Acceleration in the Solar Corona*, volume 612 of *Lecture Notes in Physics*, Berlin Springer Verlag, pages 230–260, 2003.
- [163] M. Schmidt. 3C 273 : A Star-Like Object with Large Red-Shift. *Nature*, 197:1040, March 1963. doi: 10.1038/1971040a0.
- [164] A. W. Shafter. On the Nova Rate in the Galaxy. *ApJ*, 487:226–236, September 1997.
- [165] N. I. Shakura and R. A. Sunyaev. Black holes in binary systems. Observational appearance. *A&A*, 24:337–355, 1973.
- [166] A. Shemi and T. Piran. The appearance of cosmic fireballs. *ApJ*, 365:L55–L58, December 1990. doi: 10.1086/185887.
- [167] J. Sitarek, W. Bednarek, R. Lopez-Coto, E. de Ona Wilhelmi, for the MAGIC Collaboration, R. Desiante, F. Longo, E. Hays, and for the Fermi-LAT Collaboration. Very high energy gamma-ray follow-up observations of novae and dwarf novae with the MAGIC telescopes. *ArXiv e-prints*, February 2015.
- [168] H. Sol. Very High Energy gamma-rays from blazars. In A. M. Mickaelian and D. B. Sanders, editors, *Multiwavelength AGN Surveys and Studies*, volume 304 of *IAU Symposium*, pages 119–124, July 2014. doi: 10.1017/S1743921314003524.
- [169] Stamerra, A. Private communications.
- [170] Y. T. Tanaka, J. Becerra Gonzalez, R. Itoh, J. D. Finke, Y. Inoue, R. Ojha, B. Carpenter, E. Lindfors, F. Krauß, R. Desiante, K. Shiki, Y. Fukazawa, F. Longo, J. E. McEnery, S. Buson, K. Nilsson, V. Fallah Ramazani, R. Reinthal, L. Takalo, T. Pursimo, and W. Boschini. A significant hardening and rising shape detected in the MeV/GeV ν F spectrum from the recently discovered very-high-energy blazar S4 0954+65 during the bright optical flare in 2015 February. *PASJ*, 68:51, August 2016. doi: 10.1093/pasj/psw049.
- [171] Q.-W. Tang, F.-K. Peng, X.-Y. Wang, and P.-H. T. Tam. Measuring the Bulk Lorentz Factors of Gamma-ray Bursts with Fermi. *ApJ*, 806:194, June 2015. doi: 10.1088/0004-637X/806/2/194.

- [172] N. R. Tanvir, D. B. Fox, A. J. Levan, E. Berger, K. Wiersema, J. P. U. Fynbo, A. Cucchiara, T. Krühler, N. Gehrels, J. S. Bloom, J. Greiner, P. A. Evans, E. Rol, F. Olivares, J. Hjorth, P. Jakobsson, J. Farihi, R. Willingale, R. L. C. Starling, S. B. Cenko, D. Perley, J. R. Maund, J. Duke, R. A. M. J. Wijers, A. J. Adamson, A. Allan, M. N. Bremer, D. N. Burrows, A. J. Castro-Tirado, B. Cavanagh, A. de Ugarte Postigo, M. A. Dopita, T. A. Fatkhullin, A. S. Fruchter, R. J. Foley, J. Gorosabel, J. Kennea, T. Kerr, S. Klose, H. A. Krimm, V. N. Komarova, S. R. Kulkarni, A. S. Moskvitin, C. G. Mundell, T. Naylor, K. Page, B. E. Penprase, M. Perri, P. Podsiadlowski, K. Roth, R. E. Rutledge, T. Sakamoto, P. Schady, B. P. Schmidt, A. M. Soderberg, J. Sollerman, A. W. Stephens, G. Stratta, T. N. Ukwatta, D. Watson, E. Westra, T. Wold, and C. Wolf. A γ -ray burst at a redshift of $z \sim 8.2$. *Nature*, 461: 1254–1257, October 2009. doi: 10.1038/nature08459.
- [173] M. Tavani and et al. Discovery of Powerful Gamma-Ray Flares from the Crab Nebula. *Science*, 331:736, February 2011. doi: 10.1126/science.1200083.
- [174] D. J. Thompson. Blazar Variability: A Gamma-Ray Perspective. In H. R. Miller, K. Marshall, J. R. Webb, and M. F. Aller, editors, *Blazar Variability Workshop II: Entering the GLAST Era*, volume 350 of *Astronomical Society of the Pacific Conference Series*, page 113, July 2006.
- [175] V. Trimble. The Distance to the Crab Nebula and NP 0532. *PASP*, 85:579, October 1973. doi: 10.1086/129507.
- [176] W. T. Vestrand, G. H. Share, R. J. Murphy, D. J. Forrest, E. Rieger, E. L. Chupp, and G. Kanbach. The Solar Maximum Mission Atlas of Gamma-Ray Flares. *ApJS*, 120:409–467, February 1999. doi: 10.1086/313180.
- [177] G. Vianello, N. Omodei, and Fermi/LAT collaboration. The First 100 LAT Gamma-Ray Bursts: A New Detection Algorithm and Pass 8. *ArXiv e-prints 1502.03122*, February 2015.
- [178] M. Vogel. Relativistic Celestial Mechanics of the Solar System, by Sergei Kopeikin, Michael Efroimsky and George Kaplan. *IEEE Signal Processing Magazine*, 29:375–376, September 2012. doi: 10.1109/MSP.2012.2187038.
- [179] S. P. Wakely and D. Horan. TeVCat: An online catalog for Very High Energy Gamma-Ray Astronomy. *International Cosmic Ray Conference*, 3:1341–1344, 2008.
- [180] T. C. Weekes and et al. Observation of TeV gamma rays from the Crab nebula using the atmospheric Cerenkov imaging technique. *ApJ*, 342:379–395, July 1989. doi: 10.1086/167599.

-
- [181] Y. B. Zel'dovich. The Fate of a Star and the Evolution of Gravitational Energy Upon Accretion. *Soviet Physics Doklady*, 9:195, September 1964.
- [182] B. Zhang, Y. Z. Fan, J. Dyks, S. Kobayashi, P. Mészáros, D. N. Burrows, J. A. Nousek, N. Gehrels, et al. Physical Processes Shaping Gamma-Ray Burst X-Ray Afterglow Light Curves: Theoretical Implications from the Swift X-Ray Telescope Observations. *ApJ*, 642:354–370, May 2006. doi: 10.1086/500723.
- [183] B.-B. Zhang, B. Zhang, E.-W. Liang, Y.-Z. Fan, X.-F. Wu, A. Pe'er, A. Maxham, H. Gao, and Y.-M. Dong. A Comprehensive Analysis of Fermi Gamma-ray Burst Data. I. Spectral Components and the Possible Physical Origins of LAT/GBM GRBs. *ApJ*, 730:141, April 2011. doi: 10.1088/0004-637X/730/2/141.